5-2011

Microscopy Techniques for Investigating Interactions in Microbial Systems

Amanda Nicole Edwards
aedwar11@utk.edu

Recommended Citation

Edwards, Amanda Nicole, "Microscopy Techniques for Investigating Interactions in Microbial Systems. " PhD diss., University of Tennessee, 2011.
https://trace.tennessee.edu/utk_graddiss/964

To the Graduate Council:

I am submitting herewith a dissertation written by Amanda Nicole Edwards entitled "Microscopy Techniques for Investigating Interactions in Microbial Systems." I have examined the final electronic copy of this dissertation for form and content and recommend that it be accepted in partial fulfillment of the requirements for the degree of Doctor of Philosophy, with a major in Life Sciences.

Jennifer Morrell-Falvey, Major Professor

We have read this dissertation and recommend its acceptance:

Alison Buchan, Gladys Alexandre, Dale A. Pelletier, Mitchel J. Doktycz

Accepted for the Council:

Carolyn R. Hodges

Vice Provost and Dean of the Graduate School

(Original signatures are on file with official student records.)

To the Graduate Council:

I am submitting herewith a dissertation written by Amanda Nicole Edwards entitled "Microscopy techniques for investigating interactions in microbial systems." I have examined the final electronic copy of this dissertation for form and content and recommend that it be accepted in partial fulfillment of the requirements for the degree of Doctor of Philosophy, with a major in Life Sciences.

Jennifer Morrell-Falvey, Major Professor

We have read this dissertation
and recommend its acceptance:

Alison Buchan

Gladys Alexandre

Dale A. Pelletier

Mitchel J. Doktycz

Accepted for the Council:

Carolyn R. Hodges
Vice Provost and Dean of the Graduate School

(Original signatures are on file with official student records.)

Microscopy Techniques for Investigating Interactions in Microbial Systems

A Dissertation Presented for
the Doctor of Philosophy Degree
The University of Tennessee, Knoxville

Amanda Nicole Edwards
May 2011

Dedication

This work is dedicated to my sister, Natalie Billings McCarroll.

"... a dream that became a reality and spread throughout the stars"

ACKNOWLEDGEMENTS

I would like to first thank my advisor, Dr. Jennifer Morrell-Falvey and my ORNL group leader Dr. Mitchel Doktycz for the opportunity to work in their labs as an intern and a graduate student. I am truly grateful for their guidance and for introducing me to many microscopy tools.

I want to acknowledge my thesis committee for their service. In addition to Drs. Morrell-Falvey and Doktycz, Dr. Alison Buchan, Dr. Gladys Alexandre and Dr. Dale Pelletier were immensely helpful throughout this process. I greatly appreciate the critical reviews and helpful discussions throughout my graduate career.

I would also like to extend my gratitude to Dr. Jason Fowlkes for taking valuable time away of his own work to be the computational force behind the FRAP project. Without his efforts, this collaborative project would not be possible. I would also like to thank Dr. Robert F. Standaert for his experience the Impα/NLS system, for introducing me to fluorescence anisotropy, and for always having an insightful answer my questions. Many thanks to Elizabeth T. Owens and Dr. Gregory B. Hurst for their contribution to the *R. palustris* protein interaction screen.

Special thanks go to Piro Siuti for his work on the *A. brasilense* AFM project. All of the extended work hours in front of the AFM and discussions yielded an interesting story.
Also, I would like to thank Dr. Scott Retterer for introducing me to AFM and microfluidics. I am grateful for his teaching and leadership as I took on new challenging projects. I would like to thank Dr. Gladys Alexandre and Amber N. Bible for their collaboration and providing us with the *A. brasilense* strains.

I would like to acknowledge the support of the Genome Science and Technology program at the University of Tennessee, Knoxville and the Biological and Nanoscale Systems Group at ORNL. This work was funded by the Genomic Science Program of the Office of Biological and Environmental Research, US DOE.

I would like to thank all of the lab members that I worked with, my fellow classmates, and my officemates for their support and friendship. Finally, I would like to extend my sincerest graditude to my family for all of their encouragement and support through this process. It was a long road, but I made it.

ABSTRACT

Biological interactions occur on multiple length scales, ranging from molecular to population wide interactions. This work describes the study of two specific areas of biological interactions in microbial systems: intracellular protein-protein interactions and cell-to-cell interactions. The implementation of optical and atomic force microscopy and the methodologies developed during this study proved to be invaluable tools for investigating these systems.

Identifying and characterizing protein interactions are fundamental steps toward understanding complex cellular networks. We have developed a unique methodology which combines an imaging-based protein interaction assay with a fluorescence recovery after photobleaching technique (FRAP). Protein interactions are readily detected by co-localization of two proteins of interest fused to green fluorescent protein (GFP) and DivIVA, a cell division protein from *Bacillus subtilis*. We demonstrate that the modified co-localization assay is sensitive enough to detect protein interactions over four orders of magnitude. FRAP data was analyzed using a combination of various image processing techniques and analytical models. This combined approach made it possible to estimate cell morphology parameters such as length, diameter, the effective laser probe volume, as well as to the mobile protein concentration *in vivo*, the number of bound molecules at the cellular poles, and the biophysical parameter k_{off}.

Cells not only utilize molecular interactions in the intracellular environment, but also express proteins, polysaccharides and other complex molecules to mediate interactions with the surrounding extracellular environment. In *Azospirillum brasilense,* cell surface properties, including exopolysaccharide production, are thought to play a direct role in promoting cell-to-cell interactions. Recently, the Che1 chemotaxis-like pathway from *A. brasilense* was shown to modulate flocculation, suggesting an associated modulation of cell surface properties. Using atomic force microscopy, distinct changes in the surface morphology of flocculating *A. brasilense* Che1 mutant strains were detected. Further analyses suggest that the extracellular matrix differs between the *cheA1* and the *cheY1* deletion mutants, despite similarity in the macroscopic floc structures. Collectively, these data indicate that disruption of the Che1 pathway is correlated with distinctive changes in the extracellular matrix, which likely result from changes in surface polysaccharides structure and/or composition.

TABLE OF CONTENTS

LIST OF TABLES

LIST OF FIGURES

Chapter 1. Introduction and Background

1.1. Biological Interactions

Modern biology has tried to answer why cells operate far from thermodynamic equilibrium in order to function as a self-sustaining chemical reactor all in an eloquent attempt to reproduce itself. In simplistic terms, what is life and how does it function? The unambiguous definition of life remains elusive, although technological advances continue to redefine our understanding of life. On a basic level, life is governed by biological interactions and all biological interactions follow fundamental principles of the physical and chemical sciences. In turn, these interactions lead to the assembly and organization of a cell. Yet, unraveling the complexity of interactions both within the intracellular and extracellular environment is a difficult challenge for biologists. Recent advances in genomic sequencing/annotation have led to an increased rate of high-throughput proteomic analysis and imaging technologies for a more thorough understanding of biological systems.

Ultimately, all biological systems function as a result of interacting entities forming networks, be it small molecules, DNA/RNA-protein interactions, or protein-protein interactions. Networks are dynamic yet robust, responding to environmental perturbations such that the overall function can adapt without deleterious effects. Within a cell, networks can interact with other networks which lead to a complex intra/extracellular web of interactions that contribute to survival. The field of systems biology is working toward a complete understanding of how molecular interactions lead to networks, and how these networks function together. Although systems biology is a relatively new concept in life science, it employs many disciplines such as molecular biology, biochemistry, biological engineering, and physics to derive answers.

Biological interactions occur on multiple length scales, ranging from molecular to population wide interactions. Macromolecules interact on an atomic level to form organized structures, essentially through self-assembly. This process is possible since the linear arrangement of monomers specifies the spatial configuration of the polymer, resulting in a supramolecular structure (i.e. DNA double helix, protein secondary and tertiary structures). Consequently, these structures interact in concert contributing to the overall function of the cell. Despite the immense diversity of cells between taxonomic kingdoms, it is becoming increasingly clear that all cells share similar principles.

This dissertation describes the study of two specific areas of biological interactions in microbial systems: intracellular protein-protein interactions and cell-to-cell interactions. The implementation of optical and atomic force microscopy and the methodologies developed during this study proved to be invaluable tools for investigating these systems. The following introduction will provide background and significance of these interaction systems and current techniques used to investigate them. The remaining chapters describe the practical work of this dissertation where molecular tools and fluorescence imaging methods were developed to identify and characterized protein-protein interactions *in vivo*. In addition, cell-to-cell interactions were characterized with fluorescence and atomic force microscopy.

1.2. Protein-Protein Interactions (PPIs): A historical perspective

Scientists have been aware of the cellular importance of proteins since Swedish organic chemist Jons Jakob Berzelius coined the term in 1838 [1] . Proteins are complex macromolecules comprised of amino acids. There are twenty naturally occurring amino acids that are involved in the assembly of protein polypeptide chains. Since amino acids differ in structure and composition, polypeptide chains can fold into different complex tertiary structures depending on the amino acid composition. Their complexity allows for interactions with almost any other physical component. Inorganic salts, metals, sugars, fatty acids, nucleotides, and other proteins can all interact and participate in the functionality of proteins. Moreover, proteins can have more than one specific binding partner, further adding to the complexity of biological networks. Proteins have been described as the working machines that make up the assembly line of cellular functions [2]. Simply put, highly organized interactions coordinate the functions that cellular systems depend on for survival. Numerous studies going back decades have characterized the functions of proteins and how these macromolecules react with other physical entities in their surrounding environment (for in-depth reviews please refer to [3-7]). However, for the scope of this dissertation the following section will focus on the diversity of protein-protein interactions (PPIs) and how they are characterized.

A single organism can contain thousands of PPIs, which form functional networks within a cell [8, 9]. PPIs can be characterized in a variety of ways including the type of complex they form (hetero- versus homo-oligomeric), type of association (transient versus permanent), and stability with and without its binding partner [4].   Although it is helpful for organizational purposes to classify PPIs into categories, it is important to remember interactions depend highly on the physiological state of the cell. Nevertheless, to facilitate a greater understanding of biological processes, it becomes necessary to describe PPIs categorically.

On a molecular level, proteins interact with other proteins with the same forces that act upon most macromolecules. These include van der Waals forces, hydrogen bonding, ionic interactions, hydrophobic interactions, dipole interactions, and water mediated polar interactions. The interaction of two proteins depends upon the surface structure and chemistry of the binding site [10]. Several groups [11-13] have worked, with some success, to computationally predict PPI binding sites. Of course a wide range of parameters must be considered for accurate modeling of any potential binding site, particularly when examining the pre-binding surface of a protein monomer. These parameters, which include but are not limited to electrostatics, amino acid composition, hydrophobicity, and solvent potential, give higher predictive power when combined. Thus far, the success rate for prediction is close to 70% [10]. Indeed, the data provided by computational predictions of PPIs do not circumvent the need for experimental evidence. In fact, there is not a single universal method that can accurately identify the extensive network of PPIs in a single cell. Ultimately, the ability to predict, model, and manipulate biological responses to genetic and environmental signals is dependent upon a thorough understanding of the interactions within and between cellular networks.

1.2.1. Detection of protein interactions and protein complexes in vitro and in vivo

A plethora of *in vitro* and *in vivo* methods have been used extensively to detect and characterize PPIs and each method offers different advantages and disadvantages with respect to throughput, ease of use, sensitivity, and accuracy (reviewed in [14-16]; Table 1.1). *In vitro* approaches for identifying or characterizing PPIs depend upon the purification of the proteins of interest or the *in vitro* expression of such proteins in a synthetic system. In the era of whole system proteomics, *in vitro* approaches have been adapted and updated to address questions specific to systems biology. Furthermore, improvements in the methods and analytical tools for detection have made several *in vitro* assays applicable for high-throughput analysis [17-20].

Classical biochemical methods such as affinity blotting, 2D-gel electrophoresis, affinity chromatography, and co-immunoprecipitation have proved to be valuable in characterizing numerous protein interactions over the past several decades [15]. For example, affinity chromatography was used in the 1970s to determine the interaction between host and phage proteins with the *E. coli* RNA polymerase [21]. This methodology depends on the covalent attachment of a protein of interest to a matrix, such as Sepharose, which is applied to a column. A solution of potential ligands, typically a cellular extract, is allowed to flow through the column. The resulting flow-through contains only the proteins that do not interact with the functionalized protein of interest. Other proteins that bind to the matrix can be eluted with high salt concentrations, a detergent such as sodium dodecyl sulfate (SDS), or known co-factors. Binding and elution conditions must be carefully optimized to reduce any non-specific binding, false negative results due to lack of binding, and any indirect non-specific interactions that may not be biologically relevant. Although the basic principle of affinity chromatography remains the same, genetic and technological advancements have improved the methodology to optimize isolation of protein complexes and specific identification of the proteins involved. For example, tandem affinity purification, in combination with mass spectrometry, is a protein complex purification strategy that is based on a target protein tagged with a specialized affinity tag. The TAP tag is comprised of two sequential affinity tags separated by a cleavage site (Glu-X-X-Tyr-X-Gln/Ser) from the tobacco etch virus (TEV). The “classical” affinity tag (ProtA-TEV-CBP) contains two IgG-binding units of protein A (*S. aureus*) and a calmodulin binding domain;

Table 1.1: Methods for identifying and/or characterizing protein-protein interactions (Table adapted from [16, 22]).

Approach	**Application**	**Sensitivity**	**Quantify affinity**	**Quantify kinetics**	**Throughput**
Tandem affinity chromatography	*In vitro*	< 50 nM	No	No	High
Protein arrays and microfluidic platforms	*In vitro*	<1 µM	Yes	Yes	Low/High
Yeast two-hybrid	*In vivo*	< 50 µM	No	No	Low/High
NMR	*In vitro/ In vivo*	pM- µM	Yes	Yes	Low
Surface plasmon resonance	*In vitro*	pM- µM	Yes	Yes	Low
Fluorescence polarization/anisotropy	*In vitro*	nM- µM	Yes	Yes	Low/High
FRET/BRET	*In vitro/ In vivo*	< 10 µM	Yes	Yes	Low/High
Bimolecular fluorescence complementation and derivative assays	*In vivo*	< 10 µM	Yes/No	Yes/No	Low/High
Co-localization coupled with FRAP*	*In vivo*	nM-µM	Yes	Yes	Low/High

*Assay described in Chapters 2 and 3 of this dissertation.

however, variation affinity domains (i.e. S-tag, FLAG tag, Biotinylation tag) have shown success for other species. The method offers many advantages for high-throughput proteome analysis including purification under native conditions and high specificity with low background [23]. TAP purification was first used to identify protein complexes in several model organisms, including *Saccharomyces cerevisiae* [8] and *Escherichia coli* [24-27]. These studies identified numerous molecular complexes and provided insights into the physiological role of many proteins of unknown function based on their association with proteins of known function. This method, however, tends to be biased toward identification of high affinity interactions and interactions with slow dissociation kinetics [17]. Nevertheless, thousands of protein interactions have been identified in yeast, bacteria, plant and mammalian systems [23]. More recently, this methodology has also been applied to characterize protein interaction networks in less tractable microbes, including *Rhodopseudomonas palustris* and *Shewanella oneidensis* [28].

The modern proteomics age is also taking advantage of chip based technologies, both array and microfluidic methods, for high-throughput analysis. For protein arrays, the overall methodology is similar to the DNA microarray approach. An array platform is generated with different proteins immobilized with antibodies, metal chelators, or streptavidin [16, 29]. Detection techniques usually involve fluorescence or chemoluminescent probes [29-31] but in some cases direct analysis by mass spectrometry has been successful [32, 33]. Although protein arrays allow for the detection of thousands of different binding events, the protein immobilization techniques may lead to the obstruction or deformation of the binding site. Further, stringent washing conditions and blocking proteins may compromise binding of weak PPIs [16, 32]. Still, economy of micro-scale analysis makes protein arrays well suited to high throughput investigation of PPIs. Recently, microfluidic platforms and biosensers have been implemented for high-throughput PPI *in situ* analysis. These synthetic systems are attempting to closely mimic physiological conditions, while eliminating long incubation times and reducing reagent cost [34]. For example, Javanmard et al demonstrated the use of a microfluidic based biosensor to measure electrical impedance across a microfluidic channel when a binding event is detected [34]. Gerber et al demonstrated an approach where an array of “bait” and “prey” proteins were transcribed *in vitro* and interactions were detected by an *in situ* microfluidic affinity assay [33]. Droplet based microfluidic systems have also been used to study PPIs where the manipulation of multiphase flows can generate a micro-reactor, where conditions in the droplet can be optimized to simulate the physiological state of a cell. Importantly, high rates of droplet generation coupled with fluorescence detection have significant applicability for high-throughput proteomics [35].

All of the *in vitro* approaches described above have been used effectively to identify protein interactions. However, each methodology involves cell lysis and dilution of cellular components which can have significant effects on protein interactions. Within the cell, proteins do not interact in dilute buffered solutions, but rather in a highly crowded macromolecular environment. There is growing recognition of the importance that crowding events in the cytosol play in the diffusion and reactivity of individual protein molecules [36-38]. Thus, assays that detect and characterize protein interactions in intact cells may be more relevant to natural systems.

Several classical *in vivo* assays take advantage of sophisticated genetic strategies to uncover interactions between the protein products of encoded genes under investigation. For example, extragenic suppressor mutations, which can reverse a phenotype resulting from a primary mutation, have been used to identify interactions between two proteins. An extragenic suppressor occurs in a gene other than the gene carrying the primary mutation, and restores activity of the protein products. In other words, a mutation that occurs in a protein heterodimer leads to lack of binding ultimately resulting in an observable phenotype. If a second mutation occurs in the other protein that allows the proteins to interact, this second mutation “suppresses” the effect of the first. This approach was difficult to employ since the suppressor did not have an identifiable phenotype without the original mutation [15]. However, Jarvik and Botstein identified suppressor mutations in phage P22 that carried a cold-sensitive phenotype that did not depend on the original mutation [39]. As a result of their pioneering work, this strategy has been used in bacteria and eukaryotic systems to identify protein-protein interactions involved in cell division [40], cytoskeletal structure [41], and DNA replication [42]. A synthetic lethal mutation is another genetic technique that has been used extensively for identification of interacting proteins. If a protein-protein interaction is required for an essential cellular function, then the disruption of binding will lead to a lethal or observable phenotype. The disruption of binding results from a double mutation in both interacting proteins. Dobzhansky was the first to successfully demonstrate this phenomenon in *Drosophila* [43]. Screens for synthetic lethality have also been applied to *S. cerevisiae* protein interactions [15].

The yeast two-hybrid assay is by far the most popular genetic screen used to detect interactions in living cell [44, 45]. Yeast two-hybrid was developed in the late 1980s by Fields and Song [44]. Since that time, numerous large scale interactome studies have been carried out fo eukaryotes and prokaryotes using the yeast two-hybrid assay (reviewed in [3, 45, 46]). The screening process involves a “bait” protein expressed as a chimeric fusion to the DNA-binding domain (BD) of a *S. cerevisiae* transcription factor. The other “prey” proteins that are screened against the “bait” are expressed as another chimeric fusion to an activation domain (AD) of the same transcription factor. If the two proteins interact, this action brings AD and BD together to form a functional transcriptional complex. This complex then activates the expression of a reporter gene. Most two-hybrid screens are based on at least two selection criteria with different reporter genes, typically a nutrient-based selection coupled with a colorimetric assay. Advantages of this assay include the ability to identify stable and transient interactions and map interaction domains. The yeast two-hybrid method has been employed for genome wide high throughput screens of *S. cerevisiae* [45, 47, 48], *C. elegans* [49], and *Drosophila* [50]. However, large scale yeast two hybrid screens are often challenged by high false positive and false negative rates [51]. Furthermore, classical yeast two-hybrid systems require soluble proteins or soluble domains of membrane proteins for transport into the nucleus, thus excluding any membrane bound or associated proteins. Nevertheless, yeast two-hybrid continues to be a benchmark assay for detecting PPIs *in vivo*. More recently, variations of the two-hybrid assay that involve detection of interactions in mammalian systems are diversifying the capabilities of a two-hybrid approach [52]. Another modification of yeast two-hybrid utilizes the split-ubiquitin system [53]. The interaction between two membrane proteins can be detected by the proteolytic cleavage of a fusion protein which releases a transcription factor only when the proteins of interest interact. This transcription factor thus activates a reporter gene where expression is detected by a colorimetric assay [54, 55].

1.2.2. Quantitative analysis of protein interactions

Characterization of PPIs is not limited strictly to their identification. In order to understand the consequences of PPIs for cellular function, a detailed quantitative analysis of their binding interfaces, including architecture and affinity of binding sites, must follow detection of PPIs. The overall strength of an interaction is defined by the equilibrium dissociation constant (K_d). The equilibrium state of a binary PPI is defined as:

$$P_1P_2 \rightleftharpoons P_1 + P_2 \qquad \text{(Eq. 1.1)}$$

and the corresponding equilibrium dissociation constant is defined as:

$$[K_d] = \frac{[P_1][P_2]}{[P_1P_2]} \qquad \text{(Eq. 1.2)}$$

K_d has units of molarity (M) and represents the concentration where 50% of P_2 is bound to P_1. In terms of binding kinetics, K_d is calculated from the rates k_{off}/k_{on}, where k_{off} is the rate of dissociation and k_{on} is the rate of association. Within the physiological context of the cell, the range of K_d can span over twelve orders of magnitude [4, 56]. After many years of intense research devoted to elucidating the architecture of binding sites and the role of affinity/specificity of the interactions, we are only beginning to understand their complexity. Several methods (Table 1.1), many *in vitro*, have been developed to identify PPIs and quantify their dissociation kinetics. However, just as in identifying PPIs, there is not a single method capable of completely characterizing all of the physiochemical requirements of binding. This section is a description of three of the most common techniques for quantifying PPIs.

NMR spectroscopy is a powerful technique for biophysical characterization of PPIs, particularly due to the fact that NMR offers high resolution structural information on the interaction partners. Unlike X-ray crystallography, which is also used to determine the structure of protein complexes, NMR has the added advantage of providing a measurement of binding affinity [57]. Furthermore, it does not rely on the crystallization process whereby the proteins may not crystallize in a biologically relevant conformation or the proteins may not crystallize at all. NMR spectroscopists can determine the affinity and stoichiometry of an interaction pair or complex by titrating increasing concentrations of a binding partner to a fixed concentration of protein(s). This approach is particularly well suited for weak PPIs ($K_d \geq 100\ \mu M$) where it is the only method that can determine their structure [56-58]. With the incorporation of newly designed cryogenically cooled probes, the range of sensitivity has recently increased. The current range of detection and quantification is 10^{-6} to 10^{-2} M. The advantages of using NMR to characterize weak PPIs are being realized since weak interactions are critical in cellular events such as signal transduction or transient assembly of protein complexes. For example, Vaynberg et. al. used NMR to solve the structure and quantify the interaction of the ultraweak Nck-2/PINCH-1 interaction domains (K_d 3×10^{-3}M), which is involved in regulation of assembly/disassembly of cell matrix adhesions for cell migration [59].

Since the early 1990s, the detection of PPIs by surface plasmon resonance (SPR) has become widely used due to advancements in protein immobilization on a solid surface. Several key advantages to SPR include only small amounts of sample (on the order of µg) are needed and no labeling is required. Furthermore, SPR provides quantitative data on PPI binding affinities as well as association/dissociation kinetics. The technique is completely generic for all PPIs of interest since the signal recorded relies on the properties of a thin metal film surface and the refractive index of the electromagnetic waves that propagate close to the surface. Therefore, changes detected in the local index of refraction, are due to changes in the resonance conditions of the surface plasmon waves when molecules are absorbed to the surface. By injecting the surface with a known concentration of protein, the association/and dissociation can be fitted from the phase data as a function of time. Several covalent coupling techniques have been used to functionalize proteins to a surface, similar to the protein array technology described above. In many cases, coupling with a single cysteine or a single biotin molecule may help reduce any perturbations that could abolish binding of the interacting proteins. Recently, SPR and its derivative methodologies have shown significant promise in characterizing PPIs for G-protein coupled receptors (GPCRs) [60-62] since several groups have demonstrated methods for lipid bilayer deposition and liposome absorption on SPR substrates [63, 64]. Membrane associated proteins could then be immobilized to a surface while maintaining binding capability. Alternatively, Harding et. al. were the first to demonstrate that the opposite approach could be taken by immobilizing the ligand instead of the membrane bound receptor. In their study, a GPCR ligand, neurotensin (NT), was immobilized to the surface via N-terminal-biotinylation and the detergent solubilized neurotensin receptor-1 (NTS-1) was injected over the surface as a constant flow rate resulting in SPR response data [65]. SPR techniques have been extended for high-throughput detection and quantification of PPIs [66-68]. Despite the versatility of SPR for characterizing PPIs, the method does have several limitations. For example, since proteins are immobilized to a surface, the binding detected by SPR may not reflect the binding characteristics in solution. Further, the immobilization process may inhibit/induce conformational changes or lead to inactivation of the protein, thus inhibiting binding [17].

Fluorescence (polarization) anisotropy is a widely used, facile method for quantifying PPIs in solution due to its high sensitivity, ease of data collection, and system flexibility. This technique exploits the fluorescence polarization properties of bound molecules [69]. Fluorophores that are excited with plane-polarized light emit plane-polarized light [69-71]. The degree of polarization (P) is calculated by measuring the parallel ($I_{\parallel}$) and perpendicular ($I_{\perp}$) fluorescence intensities relative to the plane of linearly polarized excitation light.

$$P = \frac{(I_{\parallel} - I_{\perp})}{(I_{\parallel} + I_{\perp})} \qquad \text{(Eq. 1.3)}$$

Emission anisotropy (A) is another term used to describe polarized emission and is derived from the ratio of the polarized component to the total fluorescence intensity.

$$A = \frac{(I_{\parallel} - I_{\perp})}{(I_{\parallel} + 2I_{\perp})} \qquad \text{(Eq. 1.4)}$$

The total fluorescence intensity along the perpendicular plane is defined as the sum of intensities for both the x and the y plane. Hence, the term $2I_{\perp}$ is defined as $I_y + I_y$ [72]. Both measurements are clearly interrelated and use of either term is appropriately considered for the system in question.

$$A = \frac{2P}{3 - P} \qquad \text{(Eq. 1.5)}$$

Generally, anisotropy (Eq. 1.5) is more commonly used to describe binding equilibrium and association/dissociation kinetics. Binding/kinetic assays rely on the principle that molecular rotations, which occur during the lifetime of fluorescence emission, result in depolarization of the emitted light (i.e. reduced anisotropy). Since molecular rotation decreases when molecular weight increases, any fluorescent ligand bound to a protein will emit a greater amount of plane-polarized light relative to the unbound state (i.e. increased anisotropy) [73]. In a direct binding assay one of the reactants, typically a small protein or peptide, is fluorescently labeled. A fluorometer measures the change in anisotropy from the bound to unbound states [71, 73]. Titration of an unlabled protein with a set concentration of fluorescently labeled ligand provides a direct measurement of the complex K_d. The resulting anisotropy can be converted to the fraction of bound ligand by the following expression:

$$x = \frac{A - A_f}{A_b - A_f + (g - 1)(A_b - A)} \qquad \text{(Eq. 1.6)}$$

where A is the observed anisotropy, A_f is the free anisotropy, A_b is the bound anisotropy, and g is the quantum yield enhancement factor. The dissociation constant, K_d, can then be calculated from:

$$K_d = \frac{(1 - x)(nP_T - xL_T)}{x} \qquad \text{(Eq. 1.7)}$$

where x is the fraction of bound ligand calculated from Eq. 4, n is the number of binding sites, P_T is the total protein concentration, and L_T is the total ligand concentration. A wide range of fluorophores are available for labeling including enhanced fluorescent proteins, fluorescent dyes such as rhodamine or Texas red, and quantum dots [74]. Since the assay does not require removal of the fluorescence probe and polarization is a ratiometric measurement (i.e. fluctuations in fluorescence intensity are self-corrected), the method has been utilized for high throughput screening for drug discovery. For example, Pfizer has developed a global cyanine-labeled based anisotropy assay for high throughput screening of pharmacologically relevant compounds [73]. Fluorescence anisotropy has also been used to thoroughly study the mechanisms of recognition by the nuclear import protein, Importin α (Impα), to nuclear localization signal variants (NLSs) [75-78]. In eukaryotic cells, Impα mediates the formation of a trimeric nuclear import complex between the cargo to be transported into the nucleus and the import receptor, Importin β (Impβ). The entire complex is then translocated via Impβ into the nucleus where the cargo is delivered. Although the biochemical and structural data confirmed that Impα binds directly to NLS peptides, the exact mechanism for recognition remained elusive [75]. Through quantitative fluorescence anisotropy, the NLS was fused to GFP and titrated with decreasing concentrations of the Impα to characterize over 26 NLS variants. In Chapters 2 and 3 of this work, we utilize the quantitative information reported in the Impα/NLS binding studies to characterize the sensitivity of a fluorescence-based protein-protein interaction assay and as a model system to develop a method to measure binding affinities *in vivo*.

1.2.3. Fluorescence microscopy: Visualizing PPIs

The previous sections highlight the importance of biochemical and cell biology based methods to identify and characterize PPIs both *in vitro* and *in vivo*. Although these techniques continue to make significant strides in elucidating protein interaction networks, a fundamental need to probe into the spatio-temporal changes in a native cellular environment has led to the development of microscopic approaches. Generally speaking, biologists have a fundamental curiosity to visually observe real-time interactions in living cells. Microscopy has revolutionized many areas of biology and the physical sciences. Light microscopy has been an important tool for biology since the late 1500s. Both prokaryotic and eukaryotic cells have been phenotypically characterized with light microscopic techniques such as bright field or phase contrast. However, molecular interactions were virtually impossible to visualize until the invention of fluorescence microscopy almost a century ago. More specifically, the development of fluorescence probes made it possible to study cellular interactions with high temporal resolution on the order of picoseconds and high spatial resolution on the order of nanometers [79-81].

In 1955, a green fluorescent substance from the jellyfish *Aequorea victoria* was first described in the literature by Davenport and Nicol [82]. Seven years later Osamu Shimomura and colleagues describe their extraction of two proteins, which lead to the characterization of a novel bioluminescent system from *A. victoria.* In this system, a photoprotein aequorin excites green fluorescent protein (GFP), resulting in the emission of green fluorescent light [83-86]. The importance of this discovery became apparent upon the successful cloning and heterologous expression of GFP by Chalfie et al [87]. GFP showed huge potential as a biomarker *in vivo*. Since then, over 30 homologous fluorescent proteins have been identified in distantly related marine organisms. Scientists continue to successfully mutate the wild-type proteins, leading to numerous variants with improved photostability, fluorescence intensity, faster maturation, and different excitation/emission wavelengths [88]. Notably, Roger Tsien’s group has generated a dynamic palette of nonoligomerizing fluorescent proteins [89]. Patterson and Lippincott-Schwartz [90] described a variant of GFP harboring a histidine substitution (T203H), which when irradiated with a 413 nm laser, lead to a stable protein with a marked increase in fluorescence intensity when excited at 488 nm. Thus, the first photoactivatible GFP (PA-GFP) was introduced. PA-GFP and its other variants enabled researchers to selectively activate and track molecules *in vivo*. Photoconvertable and photoswitchable fluorescent proteins have also been developed and used to monitor biological interactions [91]. In nearly 20 years, thousands of studies have utilized GFP to track and visualize cellular events with minimal perturbations to the cell. The significant impact of GFP was recognized in 2008 when Shimomura, Chalfie, and Tsien were awarded the Nobel Prize in Chemistry.

Along with the upsurge of novel fluorescent probes in the 1970s and 1980s, the demand for fluorescence microscopes dramatically increased. At this time a significant proportion of published work in the field of cell biology incorporated some form of fluorescence microscopy. However, by the mid 1980s, the principle limitation of fluorescence microscopy became quite apparent. The fluorescence signal in thick samples resulted in an out of focus glow, reducing the detailed resolution needed to image biological processes. This was only moderately remedied by preparing thin samples or imaging a cell line which was characteristically thin, such as epithelial cells. Unfortunately, this technique was not applicable for all questions in cell biology. Brad Amos and John White at Cambridge University, whose research focused on cell division in eukaryotes, sought to improve resolution of fluorescence microscopy so that fine details within cells could be observed [92]. They decided to investigate and apply the concept of confocal microscopy. The first confocal microscope was invented and patented by Marvin Minsky in 1957 when he postulated that the ideal microscope would measure the light absorbed or scattered at each point on a specimen. He found that this could be accomplished by placing an objective on one side of the specimen and a pinhole on the other. The pinhole acts as a spatial filter, eliminating any out of focus signal from the final image [93]. Biologists remained uninterested in this novel concept primarily due to the fact that Minsky's and other confocal microscopes relied on moving the sample stage to acquire images. This mechanism was simply too slow for biological imaging. Amos, White, and engineer Michael Fordham developed a system in 1986 where the light path is scanned rather than physically moving the sample. Thus, the first laser scanning confocal microscope was introduced specifically for biological applications. By the next decade, commercial microscope manufacturers and distributors such as Zeiss, Bio-Rad, and Leica were improving the technology and marketing confocal microscopes to biologists. These initial microscopes pioneered a new era of diverse applications in fluorescence microscopy [92].

The basic setup of a modern laser scanning confocal microscope continues to incorporate the point-by-point illumination of the sample and elimination of out of focus light (Figure 1.1) [94]. A laser serves as the excitation light source for sample illumination. The laser is reflected off of a dichroic mirror, which then sends the light to a set of horizontal and vertical rotating mirrors. The mirrors then scan the light over the sample. The fluorescent molecules in the sample are excited at the point of illumination. The resulting fluorescence emission passes back through the rotating mirrors, the dichroic mirror, and a pinhole aperture. Thereafter, the light that manages to pass through the pinhole is measured by a photomultiplier tube (PMT). An image is digitally constructed as the computer records one pixel at a time. Scan rates and image resolution depend on the desired imaging application [94]. For example, typical image acquisition of bacteria using a Leica TCS SP2 laser scanning confocal microscope as described throughout the practical work of this dissertation has a scan rate set to the default value of 300

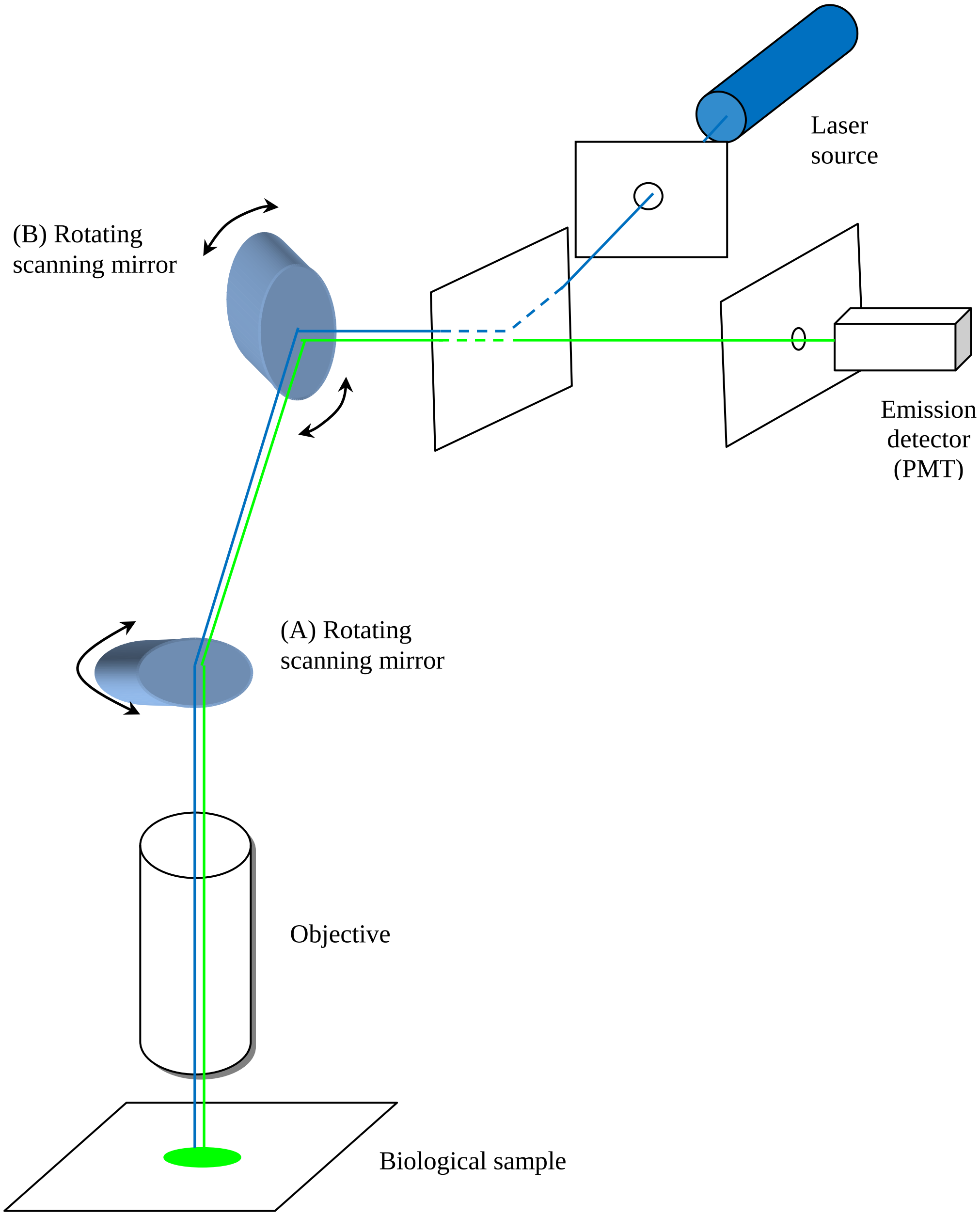

Figure 1.1 General design of a laser scanning confocal microscope. The laser source illuminates the specimen at a specified excitation wavelength. The scanning mirrors (A) and (B) adjust the laser beam position to scan the specimen. Figure is modified from [93].

Hz and results in a 512 x 512 pixel image. However, the scan rates, resolution, and other parameters are optimized for fluorescence recovery after photobleaching (FRAP), as described in Chapter 3.

As a result of advances in confocal microscopy and novel fluorescence probes, new methods have been developed for detecting protein interactions *in vivo.* For example, interactions between two proteins that are less than 100Å apart can be imaged and assessed by detecting fluorescence resonance energy transfer (FRET) between donor and acceptor fluorophores fused to proteins of interest [95, 96]. FRET determines the propinquity between labeled proteins in the nanometer range. The work of Tsien [89], Piston [88] and others [97-99] have produced stable variants of fluorescence proteins optimized for FRET experiments. Such mutations are necessary to reduce problems generally associated with FRET such as spectral cross-talk, elimination of dimerization, and optimized brightness, all while maximizing FRET efficiency. The most widely used FRET pairs continue to be variants of CFP and YFP. The significant amount of cross-talk between the pair has been recently mitigated by the development of CFPs such as mCerulean [100] and YFPs such as mVenus [101]. In addition to the standard CFP/YFP pairs, EGFP paired with monomeric variants of RFP such as DsRed [102], mRFP1 [103] and mCherry [89] have proved to be useful for FRET experiments investigating PPIs. For example, FRET has been recently used to investigate eukaryotic signaling cascades in response to contact with the Gram-negative pathogen *Neisseria gonorrhoeae* [104]. Resonance energy transfer is not strictly limited to fluorescence. Bioluminescence resonance energy transfer (BRET) is similar to FRET, but the donor fluorophore is replaced by a luciferase, thereby reducing extraneous fluorescence and photobleaching [105-107]. Other fluorescence based assays have been successfully employed to identify PPIs. For example, bimolecular fluorescent complementation (BiFC) assays can identify protein-protein interactions based on the reconstitution of a fluorescent protein, such as GFP or YFP, by non-fluorescent fragments fused to interacting proteins [108-111]. BiFC has been coupled with FRET to identify interactions in tertiary protein complexes [112].

Fluorescence recovery after photobleaching (FRAP) has also been implemented in investigating the binding kinetics of interacting proteins. This is based on the principle that when interactions are present, there is a lag in FRAP recovery in relation to only diffusion based recovery [113]. In other words, binding of a mobile protein to an anchored cellular component will impede the protein's mobility through the cellular milieu or a cellular membrane. James G. McNally, the principle investigator of the Fluorescence Imaging Group at the National Cancer Institute, has been instrumental in developing FRAP methodologies and mathematical models to estimate *in vivo* binding dynamics. Typically, FRAP experiments are performed with a laser scanning confocal microscope, which provides laser power for a directed photobleach pulse to a region of interest (ROI). McNally [114] outlines nine FRAP acquisition parameters that must be determined and/or set correctly in the system in order to quantitatively analyze the FRAP recovery curves (Table 1.2).

Other experimental parameters that should be explored include photoreversibility of GFP after bleaching and an estimate of the diffusion constant of the GFP fusion protein. First, photoreversibility can be determined experimentally by fixing cells expressing the GFP variant used in subsequent FRAP experiments, photobleaching the complete fluorescence content of the cells, and monitoring recovery. It is expected that the photobleach in this case remain

Table 1.2 General FRAP acquisition parameters [114].

Parameter	Guidelines
Number of pre-bleach images	At least 10-20 images are recommended.
Shape of the bleached region	The shape of the region of interest (ROI) affects FRAP recovery.
Size of the bleached region	It is recommended that the bleach spot size should be no more than 10% of the cellular area/compartment under analysis.
Laser power for photobleaching	The laser power should be optimized to photobleach the ROI at least by 50% for accurate recovery curve fitting.
Duration of the bleach pulse	This parameter should be small compared to the time of recovery. If not, recovery can occur along with bleaching.
Lag time between photobleach and first post-bleach image	This parameter should be small to measure rapid kinetics of binding.
Laser power for imaging	Laser power should be optimized such that unintential photobleaching is minimized while acquiring enough contrast to measure fluorescence recovery.
Duration of post-bleach imaging	FRAP recovery should reach a plateau to ensure that binding kinetics can be determined from the data.
Time interval between post-bleach images	This time interval depending on the kinetics of the binding molecules. At least 20 time points are recommended for analysis.

irreversible, but in some instances spontaneous re-fluorescence may occur. If this is the case, then the reversible photobleaching must be quantified and subtracted from FRAP recoveries. Second, an estimated diffusion constant of GFP without the fusion protein can be determined by FRAP experiments when GFP is expressed as a mobile protein in live cells. A bleach pulse is applied to an ROI similar in size and shape to the experimental ROI. The resulting curve can be fit with the following equation for simple diffusion:

$$\mathrm{frap}(t) = 1 - \varphi + (\varphi e^{-\alpha})[I_0(\alpha) + I_1(\alpha)] \qquad \text{Eq. 1.8}$$

where φ is the bleached fraction of protein, I_0 and I_1 are modified Bessel functions, and the α term is defined by:

$$\alpha = w^2/2Dt \qquad \text{Eq. 1.9}$$

where w is the bleach spot radius and D is the diffusion constant. This equation is applicable to FRAP experiments with circular bleach ROIs. Other ROIs with rectangular or more complex geometries follow different mathematical models [114-117]. The diffusion constant of the GFP-fusion protein can be estimated by means of:

$$D_{\text{GFP-fusion}} = D_{\text{GFP}} \left(\frac{M_{\text{GFP}}}{M_{\text{GFP-fusion}}} \right)^{1/3} \qquad \text{Eq. 1.10}$$

To determine if binding occurs between the GFP-fusion protein and some other cellular component, a direct comparison is made between the FRAP recovery curves of the unconjugated GFP and the GFP-fusion protein. If the FRAP recovery of the GFP-fusion is slower than the non-binding GFP molecule, then interactions are assumed to be present. From this point, the contributions of diffusion and binding to the recovery curve must be determined. In short, FRAP recovery can be "diffusion-uncoupled" or "diffusion-coupled" (Figure 1.2). In diffusion-uncoupled FRAP, the diffusion of a molecule occurs more rapidly relative to the time binding occurs. As a result, the majority of the FRAP curve represents the binding interaction, where only a short diffusive recovery occurs at the beginning of the curve. Quantitative data can be extracted from the recovery curve by applying mathematical models. Indeed, several models are available for analysis of diffusion-uncoupled recovery [118]. McNally notes that the simplest evaluation of a single binding state is predicted by the inverse of exponential decay:

$$\mathrm{frap}(t) = 1 - \varphi_{\mathrm{app}} e^{-k_{off} t} \qquad \text{Eq. 1.11}$$

In diffusion-coupled FRAP recovery, the time of diffusion is analogous to or much slower than the time required for the molecule of interest to associate with a binding site. Interpretation of diffusion-coupled FRAP recovery is more convoluted since diffusion cannot simply be ignored. In this scenario, the binding data and the contribution of diffusion contribute to the overall FRAP recovery curve. Because the data is intermixed, more complicated mathematical models are required to fit a diffusion-coupled recovery curve, particularly when the diffusion time is similar to the association time. For such complex cases, computer software has been developed for these calculations [119, 120].

FRAP has been applied to determine the binding kinetics of endogenous intracellular proteins in several studies [115, 121, 122]. For example, Carrero and colleagues have made

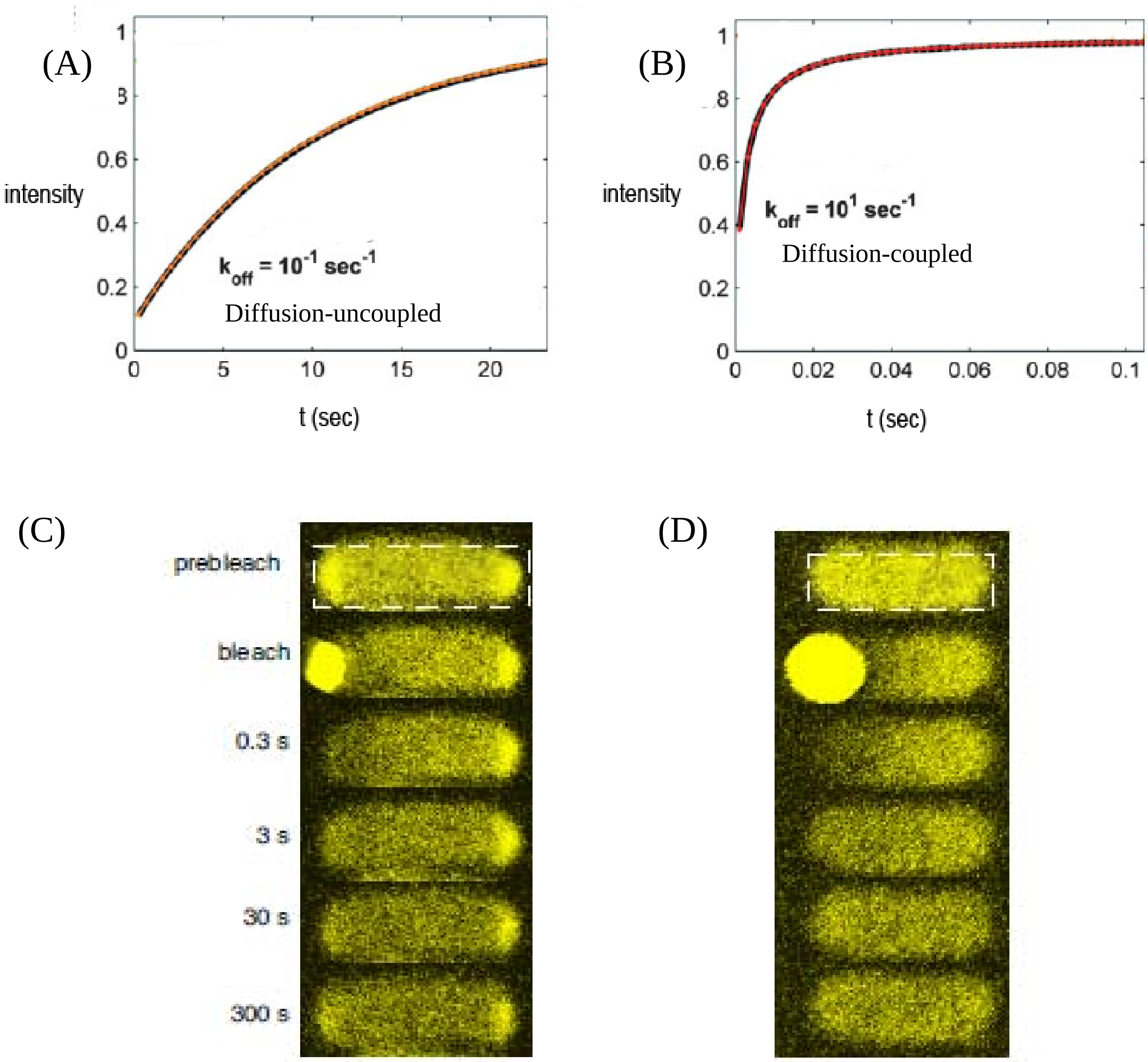

Figure 1.2 (A) Diffusion-uncoupled FRAP recovery curve. (B) Diffusion-coupled FRAP recovery curve. (C) FRAP images of *E. coli* CheZ-YFP fusion expressed in *flgM* and (D) *flhC* deletion mutants. *flgM* mutants have a fully functional chemotaxis system with increased protein expression levels to enlarge the chemotaxis cluster for FRAP experiments. *flhC* mutants do not have a fully functional chemotaxis system. Schulmeister et. al. applied FRAP to investigate the mobility and exchange kinetics of all *E. coli* cytoplasmic chemotaxis proteins and the chemotaxis receptor Tar [123] .

significant advances in the study of histone/chromatin interactions [121]. McNally et al used FRAP experiments to study the dynamic exchange of glucocorticoid receptors between chromatin regulatory elements and the nuclear compartment [123]. FRAP was recently applied to investigate the exchange kinetics of chemotaxis proteins at the cell poles in *E. coli* (Figure 1.2) [124]. In chapter 3 of this work, we describe a methodology that generically anchors a protein of interest to a discrete location (cell pole of *E. coli*) and FRAP is employed to examine the strength of binding.

1.3. Bacterial Extracellular Interactions

Biological interactions are not limited to intracellular networks. Sensing and adapting to environmental changes are essential survival strategies for bacteria. The cell wall or outer cell membrane is in a continuous state of interaction with the external environment. On a molecular scale, bacteria are externally bombarded with molecules. As a result of these interactions, cells elicit a physiological response to these external stimuli based on chemosensory and molecular relay systems. In addition, frequent external interactions require physical contact at the interface of the bacteria and the substrate. In many cases, mechanisms whereby bacteria detect the presence of a physical or biological surface and interact with it remain to be determined. This section will provide a brief overview of bacterial aggregation and the use of atomic force microscopy to investigate the forces that mediate this behavior.

1.3.1. Cell aggregation: An overview

In natural systems, single cell organisms such as bacteria, do not live as pure planktonic cultures as seen in the laboratory. Countless species tend to interact and adhere to specific interfaces within the environment. Interfaces between a bacterium and the environment include bacterial cells (single or multi-species), ‘host’ eukaryotic cells, or solid abiotic substrates. Depending on the environmental conditions, the interactions can lead to a wide spread phenomenon known as microbial aggregation. Many synonymous terms are found throughout the literature describing the gathering of bacteria including association, agglutination, multicellular adhesion, cohesion, flocculation, and biofilm formation. Extracellular interactions are mediated by the same macromolecular interactions (i.e. van der Waals forces, ionic interactions, and hydrostatic forces) that take place in the cytoplasm [125-128]. Generally speaking, cellular aggregation of microbial cells involves association of biopolymers, which form a hydrated extracellular matrix (Figure 1.3). Bacterial cells can accumulate at a solid-liquid interface in freshwater or marine systems, or associate with eukaryotic tissues in symbiotic or parasitic relationships. In many natural systems, bacteria can form multispecies aggregates, generating a highly organized microconsortia. Here, bacteria are afforded the opportunity to undergo horizontal gene transfer, communicate via quorum sensing systems, and sequester nutrients from water flow through the matrix. Furthermore, bacteria aggregate at these interfaces as a form of defense or stress response, to colonize preferable habitats, and to elicit the benefits found in a communal relationship [125, 127].

Indeed, a plethora of bacterial species are capable of aggregative behavior in numerous environmental settings. For example, Entroaggregative *E. coli* (EAEC) is a clinically important category of pathogenic *E. coli*, which is associated with life-threatening watery diarrhea. The prototypical highly aggregative phenotype is characterized by layers of aggregating bacteria embedded in a mucosal matrix overlaying the epithelial cells of the small intestine [129]. Autoaggregation of EAEC strains in broth cultures has also been observed [130]. The

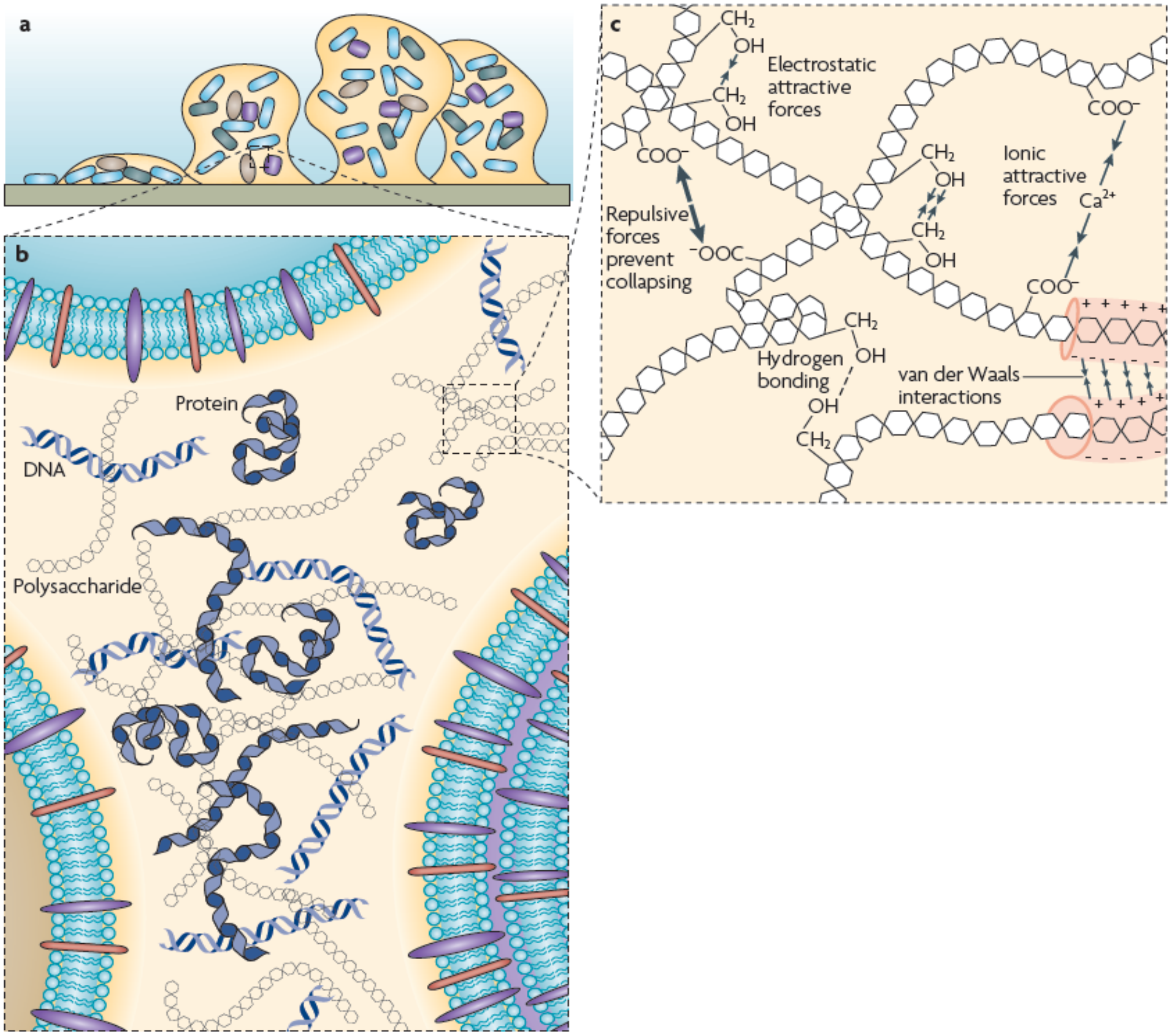

Figure 1.3 Extracellular matrix represented at different scales. (A) Bacterial biofilm formed on a solid substrate. (B) Components of the extracellular matrix. (C) Biophysical interactions that stabilize the matrix. Reprinted by permission from Macmillan Publishers Ltd: Nature Reviews Microbiology [127], copyright (2010).

aggregative phenotype has been linked to the expression of bundle forming fimbriae and extracellular hydrophobic proteins [131, 132]. As with many pathogenic bacteria, EAEC adhesins are classified as virulence factors, which contribute to the symptoms of EAEC infection/colonization. Microscopy and genetic studies have revealed heterogeneity in adhesins among EAEC strains, a factor that may impede vaccine development. Such findings underscore the importance of characterizing mechanisms of clinically-important bacterial aggregation [129]. Other well-studied aggregation systems include the Myxococcus soil bacteria family, which have developed a unique survival strategy in response to starvation. During conditions of nutritional stress, Myxococcus spp cease cellular division and differentiate into spore-filled fruiting bodies (reviewed in [133-135]). Collectively, a fruiting body contains approximately 10^5 myxospores. Upon suitable environmental conditions, all spores germinate simultaneously resulting in a metabolically active colony. High-resolution microscopy has revealed that cell-to-cell adhesion is directly related to fibrils, an extracellular adhesin comprised of proteins and polysaccharides [136, 137]. Fibrils are distinguished from pili due to their polysaccharide components and their size (fibrils are longer and greater in diameter).Bacteria that contain mutations that result in fibrillar deficiency do not aggregate in liquid culture or differentiate into fruiting bodies [136, 138, 139].

1.3.2. Mechanisms of interaction

How do bacteria stick together? In other words, what are the forces that govern the interactions between bacteria and other interfaces that result in aggregation? A highly simplistic explanation for bacterial “stickiness” is the ability to secrete extracellular adhesins for modification of the cell surface and their immediate surroundings. These modifications are typically tailored to the environmental conditions and the changes that occur therein. The synthesis and secretion of extracellular substances result in a complex matrix that can account for more than 90% of the dry mass in an aggregation of cells [127]. Initially, the extracellular material was thought to be comprised of mostly polysaccharides. However, further data indicate that the matrix is not limited to carbohydrates per se, but includes proteins, DNA, lipids, and can even contain more complex organic material accumulated in soil/water environments [127, 140]. Although aggregation systems are ubiquitous for many bacterial species, the extracellular matrix differs in specific composition and structure, resulting in different architectures. The structure can range from smooth and flat, to rough or filamentous. The porosity and elasticity of the extracellular matrix can vary as well. Essentially the architecture of the aggregating body is governed by the composition of the extracellular matrix and the interactions which occur on and around the cell surface. Architecture is also influenced by environmental factors (i.e. hydrodynamic forces, viscosity), motility, and quorum sensing [127].

For many species of bacteria, the major constituents in mediating cell-to-cell interactions are polysaccharides and proteins. The polysaccharide components of the extracellular matrix are well characterized for several species, owing to their ubiquity in cellular adhesion [126, 127]. Most exopolysaccharides are a mixture of neutral and charged residues with varying chain lengths and side chain branches [126, 127]. Mucoid *P. aeruginosa* strains produce alginate, the most thoroughly studied exopolysaccharide due to the clinical importance of chronic infections in cystic fibrosis patients [140-142]. Alginate overexpression has been classically implicated in the protection of *P. aeruginosa* from the host immune system as well as mediating adherence to the host lung tissue [142]. Wozniak and colleagues noted in a recent study that alginate, although important, is not the primary structural component *P. aeruginosa* strains PAO1 and PA14 during the establishment of biofilms. They suggest that other yet-to-be identified exopolysaccharide is involved in establishing initial cell-to-cell interactions [143]. In addition, non-mucoid strains of *P. aeruginosa* do not express alginate, but export polysaccharides that are primarily glucose-rich or consist of repeating chains of D-mannose, D-glucose, and L-rhamnose residues [127, 142]. These polysaccharides are also important in the formation of biofilms on host tissue or pellicles at air-liquid interfaces [142]. Cellulose is another example of an extracellular polysaccharide involved in cellular aggregation. Cellulose is a critical matrix component for several species, including the human pathogens *E. coli* and *S. typhimurium,* where it provides scaffolding and strengthens the interactions between cells. The diversity of exopolysaccharides is obviously not limited to the examples presented here. Variation of sugar residues, charge states, chain length, and functional roles are all different even among strains of the same species [126, 127, 140].

Although many of the proteins secreted by cells are enzymatic, others provide structural support and promote adhesion during aggregation. Carbohydrate binding proteins, known as lectins, help stabilize the polysaccharide components of the matrix via linking the cell surface with secreted exopolysaccharides [127]. *P. aeruginosa* expresses a galactose specific lectin, LecA, which contributes to biofilm formation. Mutants deficient in LecA showed a significant decrease in adhesion to a solid surface [144]. Another *P. aeruginosa* lectin, LecB, exhibits a high specificity for fructose. This lectin was also implicated cell-to-cell aggregation, where a mutant lacking LecB was impaired in biofilm formation [145]. Other bacteria such as *Streptococcus* spp and *B. subtiils* all express outer membrane lectins which bind extracellular polysaccharides for aggregation stability [127]. Other structures such as pili, fimbriae, amyloid fibers, and flagella are appendages that mediate and support cell-to-cell interactions [127, 140].

Other extracellular components associated with aggregation include extracellular DNA (eDNA), surfactants, and lipids [127]. eDNA is a surprising component, particularly when thought of as functional intercellular connectors instead of serving as genetic code. Initial assumptions marked eDNA as a lingering material from lysed cells, where its structure and adhesive properties in the extracellular matrix were not appreciated. However, recent evaluations show that eDNA is an important factor in bacterial aggregation [146, 147]. For example, flocculation of *Rhodovulum* spp is attributed to an extracellular matrix comprised of polysaccharides, proteins, and eDNA. Treatment with nucleolytic enzymes resulted in dispersal of the floc, indicating the importance of eDNA for floc structural stability or cell-to-cell adhesion [148]. Surfactants and lipids are also found in the extracellular matrix and play a role in adhesion, particularly to waxy or oily surfaces (i.e. external plant tissue such as roots or leaves) [127]. Further, lipopolysaccharides (LPS) have been implicated in the adhesion of pathogens, such as *E. coli*, to host epithelial tissue [149].

1.3.3. Cell-to-cell interactions of Azospirillum spp.

The rhizosphere is a nutrient habitat comprised of the soil environment directly surrounding plant roots. This region is influenced by the accumulation of complex organic molecules released by plants. It is estimated that 40% of the carbon fixed by terrestrial plants are secreted as root exudates [150]. In turn, this environment gives rise to multiple niches to support bacterial and eukaryotic colonization. Carbon and energy sources diffuse through the surrounding soil, establishing a concentration gradient adjacent to and under the root zone.

Motile bacteria preferentially move toward and colonize regions optimal for growth [150]. Although the rhizosphere is one of the most diverse prokaryotic ecosystems, competition between species demands strict adaption strategies for survival.

Rhizobacteria, particularily the species of the genus *Azospirillum* have been closely studied as a model system. Colonization was found to have a considerable beneficial effect on plant growth [151]. The plant growth-promoting capabilities of *Azospirillum* have been attributed to several mechanisms (reviewed in [151, 152]). For example, inoculation of *A. brasilense* on maize or wheat roots results in altered root morphology which promotes increased mineral and nutrient uptake and ultimately higher crop yields [153]. *A. brasilense* plant root interactions can also promote secretion of plant phytohormones such as auxins, cytokinins, and gibberellins that stimulate an increase in root hair length and root density [154-157]. *A. brasilense* has an oxidative metabolism that is optimum under microaerophilic conditions, which also corresponds to the preferred conditions for free-living nitrogen fixation [158]. These beneficial effects of *Azospirillum* have led to increased biomass production and crop yield for agriculturally important plants. Several mechanisms for root attachment have been proposed. The heavily glycosylated polar flagellum is considered to serve as an adhesin for root attachment.

The rhizosphere is dynamic and influenced by a assortment of factors. Environmental perturbations such as prolonged drought, excessive moisture, and acidification can influence the rhizosphere ecology. *Azospirillum* spp. have mechanisms in place to cope with ecological stresses. Under conditions of high aeration and limiting availability of combined nitrogen, *A. brasilense* cells differentiate into aggregating cells and form dense flocs that are visible to the naked eye [159, 160]. Flocs are formed by non-motile cells embedded in a dense polysaccharide matrix and by cell-to-cell aggregation [161]. It has been postulated that flocculation in *Azospirillum* functions as a survival mechanism under severe stress [161-163]. Flocculation has been shown to correlate with, and likely requires, the production of arabinose-rich extracellular polysaccharides [164]. Scanning electron and fluorescence microscopy studies of *A. brasilense* aggregating cells indicate the presence of fibrillar material connecting cells to each other or to both biotic and abiotic substrates [165, 166]. These fibrils seem to be absent in non-aggregating cells or mutants strains that are defective in aggregation, suggesting they may play a role in promoting this behavior [160, 167]. Fibrillar material has also been observed in *Azospirillum*-root interactions where small groups of aggregating cells preferentially colonize root surfaces [153, 165, 168, 169]. The detailed biochemical composition of this fibrillar material remains unknown, but it is possible that it is related to EPS production [164]. In support of this idea, the degree of bacterial aggregation appears to correlate with the amount and composition of EPS produced by *A. brasilense* strains [160]. Recently, *A. brasilense* Sp7 was found to produce a 67 kDa outer-membrane lectin that specifically recognizes the bacterial EPS. Other outer membrane proteins (OMPs) isolated from *A. brasilense* have also been implicated in non-specific association with EPS [170].

1.3.4. Atomic force microscopy

Imaging of biological interactions is not limited to optical microscopy. In fact, the resolution of a light microscope does not allow for the visualization of extracellular ultrastructures which are essential for many cell-to-cell interactions. The development of the transmission electron microscope in 1931 by Max Knoll and Ernst Ruska [171] revolutionized magnification capabilities in the field of microscopy. Optical microscopy, limited by the diffraction properties of light through an objective lens, can magnify specimens approximately 2000x, roughly visualizing structures as small as 200-300 nm. However, advanced electron microscopes can magnify up to 2,000,000x reaching the atomic level. In 1945 the first image of an intact cell was taken with an electron microscope by Keith R. Porter, Albert Claude, and Ernest F Fullam [172]. For the first time, biologists could observe cells and viral particles in striking detail. While the accomplishments of Porter et al pioneered a new age in biological imaging, the limitations of electron microscopy quickly became apparent. Harsh sample preparation (i.e. formaldehyde fixation, ethanol dehydration, sample coating with a conductive material) and imaging in a vacuum prevented visualization of extracellular functions of living cells in real time. In 1986 Binnig et al introduced a novel invention termed the Atomic Force Microscope (AFM). AFM belongs to the broad family of Scanning Probe Microscopes (SPM), which use a physical probe to scan the surface of a sample. Unlike other forms of SPM, such as the Scanning Tunneling Microscopy (STM; also developed by Binnig in 1981), imaging beyond the diffraction limit of light did not require a conductive surface or complex fixative procedures of biological samples [173]. Thus, AFM has become a remarkable tool for imaging biological samples, particularly in physiological conditions.

One of the key principles of operation includes a silicon or silicon nitride cantilever usually between 100 to 500 µm long and 0.5 to 5 µm in thickness. On the underside of the cantilever, a nano-tapered tip senses the force between the sample and cantilever. A laser point of light is focused on the back of the metallic-coated cantilever. The reflected laser point is relayed to an optical system with a position sensitive photodiode (PSPD), which measures

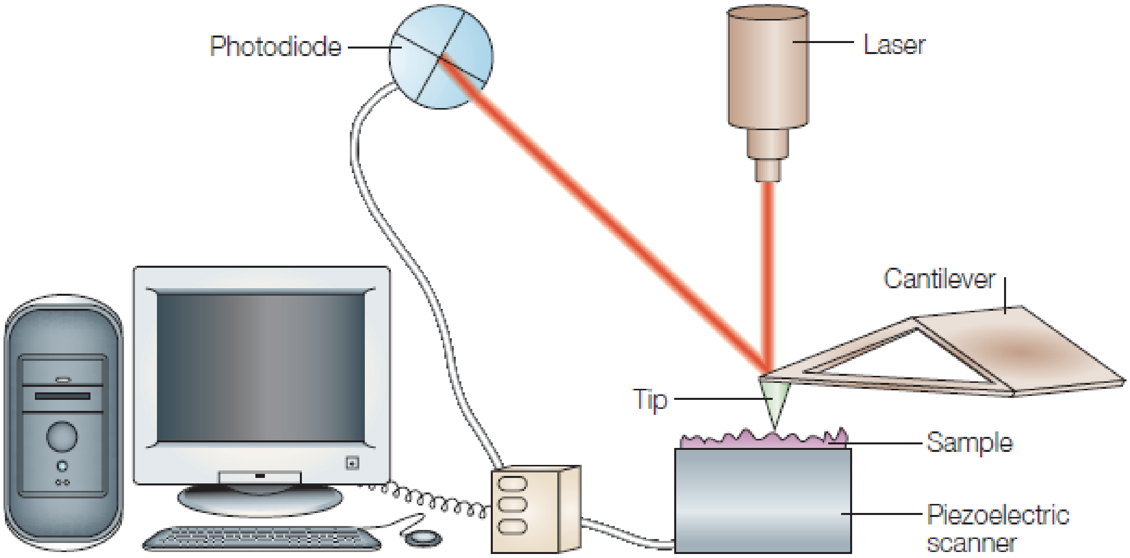

Figure 1.4 Atomic force microscope. Reprinted by permission from Macmillan Publishers Ltd: Nature Reviews Microbiology [174], copyright (2004).

changes in the laser point corresponding to the cantilever movement over the sample. The instrument is sensitive enough to detect changes in the laser movement as small as 1 nm [175]. When operation is set to force mode, the instrument's force sensitivity is within the piconewton range[174]. AFM can be operated in several modes of function including contact, tapping, force, and lateral force. In Chapter 5, contact mode was employed for all experiments examining the extracellular ultrastructure of *A. brasilense* during flocculation and will be described in detail here. Contact mode can be employed in both air and liquid imaging, where the cantilever tip is closely associated with the sample surface. The cantilever deflection is maintained at a constant value by a piezoelectric scanner. As the cantilever raster scans over the sample surface, changes in the deflection are monitored with an electric feedback system. This system then applies a voltage to the piezo, which moves the cantilever in the *z* (height) direction to keep the deflection constant. A topographic image of the sample surface is generated as the computer software measures the scanner distance moved in the z direction relative to spatial variation in the x-y plane. During tapping mode, the cantilever is oscillated near its resonance frequency. The tip is then scanned over the surface where the amplitude and phase are monitored. The interactions that occur when the tip is near the surface reduce the amplitude of oscillation, while the piezo adjusts the height to maintain constant amplitude of oscillation. Tapping mode is beneficial for biological imaging since damage to the sample surface and lateral forces are significantly reduced [174]. To physically measure biological interactions, force mode records the cantilever deflection as the tip approaches the surface and is retracted from it. From this data, appropriate corrections are applied to generate a force versus distance curve [174].

Within the past 25 years, AFM investigations have probed DNA molecules, proteins, lipid membranes and mammalian cells. Only in recent years, AFM has gained the attention of microbiologists, where it is an established technique to observe microbial cell surfaces and extracellular interactions. This was illustrated in a recent example where Salmonella biofilm morphology and the roles of several extracellular adhesion mechanisms were investigated with AFM [176]. Researchers have applied AFM to study the extracellular material of *A. brasilense* Sp7. van der Aa and Dufrêne investigated the absorption of *A. brasilense* Sp7 expolymers onto polystyrene substrate under different growth conditions. They hypothesized that adhesion of the bacteria to the substrate is mediated by secreted polysaccharides and proteins. Indeed, AFM topographic imaging and force distance analysis indicated that a continuous proteinaceous layer was absorbed onto the substrate, changing the properties of the surface. Changing the growth conditions from favorable (nutrient medium, optimal temperature, 24 h for adhesion) to unfavorable (reduction in incubation time and temperature) reduced the adhesion density and the extracellular material present on the polystyrene. This work supports the hypothesis that extracellular material produced by *A. brasilense* Sp7 mediates the interactions between the cells and the abiotic substrate. In Chapter 4 of this work, AFM was used to detect distinct changes in the surface morphology of flocculating *A. brasilense* Che1 mutant strains.

Chapter 2. Intracellular Interactions: Co-localization assay for detecting protein-protein interactions

This chapter is based on a manuscript reprinted from *Analytical Biochemistry*, 395/2, A. Nicole Edwards, Jason D. Fowlkes, Elizabeth T. Owens, Robert F. Standaert, Dale A. Pelletier, Gregory B. Hurst, Mitchel J. Doktycz, Jennifer L. Morrell-Falvey, "An in vivo imaging-based assay for detecting protein interactions over a wide range of binding affinities". 166-177, Copyright (2009), with permission from Elsevier.

Data, images, and text relevant to this study are included in this chapter. Images are presented in color where they were published in black and white. Under the direction of the co-authors, I conducted the experiments, analyzed the resulting data, and drafted the manuscript. The co-authors responded with editorial comments and additional text where needed.

2.1. Introduction and significance

Ding and colleagues have described an imaging-based bacterial protein interaction screen that allows for rapid identification of protein interactions *in vivo* [177]. This technique relies on the localization properties of DivIVA, a cell division protein from *Bacillus subtilis* [178]. DivIVA localizes to the cell poles and provides a general mechanism to target a protein to a discrete spatial location within a live cell. Although *E. coli* and other Gram-negative bacteria lack a DivIVA homolog, its localization pattern is maintained when expressed in these cells [178]. In this assay, a protein of interest is fused to DivIVA and its potential binding partner is fused to green fluorescent protein (GFP). Following co-expression of both fusion proteins in *E. coli*, a positive protein interaction is detected if the GFP-fusion protein is recruited to the cell pole due to its interaction with its binding partner anchored to the cell pole via DivIVA. This assay has several advantages, including the ability to test interactions in the context of a living cell, ease of use, rapid results, and amenability to high throughput screening. In addition, because the criteria for interpreting a positive interaction is based on simple GFP localization patterns in cells, this assay is amenable to automated image analysis. To this end, we have developed an algorithm that can be used to automatically identify positive interactions based on changes in the GFP-fusion protein localization patterns in cells before and after induction of DivIVA-fusion protein expression [179].

Here, we report modification of the co-localization assay to facilitate rapid cloning and high-throughput applications and determine the range of binding affinities that can be detected using this assay. Further, we compare the ability to detect protein interactions using the co-localization assay with the benchmark yeast two hybrid assay. To allow rapid cloning, we constructed new vectors encoding N- and C-terminal DivIVA or GFP molecular tag fusions based on site-specific recombination technology [180]. Importantly, recombination-based reactions for cloning and plasmid preparation of this vector set can be fully automated. Once the expression vectors are successfully transformed into *E. coli* and the cells are grown in liquid culture, assay results can be obtained in 60 minutes. The sensitivity of the assay was defined using a well-characterized protein interaction system involving the eukaryotic nuclear import receptor subunit, Importin α (Impα) [181] and variant nuclear localization signals (NLS) representing a range of binding affinities [76, 78, 182]. Using these interaction pairs, we demonstrate that the modified co-localization assay is sensitive enough to detect protein interactions with K_d values that span over four orders of magnitude (1nM to 15μM). Finally, we utilized this assay to confirm numerous protein interactions identified in a large scale protein interaction screen in *R. palustris*. *R. palustris* is a metabolically diverse, purple nonsulphur phototrophic bacterium that has the ability to grow on a wide range of carbon substrates, including aromatic acids derived from lignin. In addition, it has the ability to fix nitrogen gas into ammonia with hydrogen produced as a byproduct of this reaction. This pilot study demonstrated the suitability and utility of the co-localization assay for both high throughput and directed protein interaction studies.

2.2. Materials and methods

2.2.1. Bacterial growth and media

E. coli strains DH5α and BL21(DE3) (Invitrogen) were grown in Luria-Bertani (LB) medium [183], which was supplemented with 50 µg/ml kanamycin, 15 µg/ml chloramphenicol, or 50 µg/ml ampicillin as needed. *E. coli* cultures were grown at 37ºC unless otherwise noted. Plasmids pNGFP, pCGFP, pNDIV, and pCDIV were transformed and propagated in chemically competent *E. coli* DB3.1 (Invitrogen) due to the presence of the *ccdB* gene in each destination vector. The *ccdB* positive-selection marker acts by targeting the DNA gyrase and killing the background of cells. Only cells containing the desitination vector will give rise to viable clones. All other plasmids lacking the *ccdB* gene were transformed and propagated in chemically competent *E. coli* DH5α. For protein expression, plasmids were transformed into *E. coli* BL21(DE3) cells. L-arabinose was added to a final concentration of 0.2% to LB medium to induce expression of DivIVA-fusion proteins.

2.2.2. DNA recombination procedures

BP and LR clonase recombination reactions were performed according to manufacturer's instructions (Invitrogen). Purification of PCR products or plasmid DNA was performed using Qiagen DNA purification kits (Hilden, Germany). PCR reactions were performed using a GeneAmp thermocycler (PerkinElmer, Walthum, MA) with Vent polymerase (New England

Biolabs, Ipswich, MA). All oligonucleotides used as primers for this study were purchased from Integrated DNA Technologies (Coralville, Iowa) and reaction protocols were optimized according to the oligonucleotide specification.

2.2.3. Construction of GFP destination vectors.

The N-terminal GFP destination vector pNGFP was derived from pACYC184. The DEST17 cassette (nt 1-1979) was PCR amplified from pDEST17 (Invitrogen) as a HindIII-HindIII fragment using the primers 5'-cccaagcttagatctcgatcccgcg-3' and 5'-ccgaagcttggatatccggatatagttcc-3'. The resulting fragment included the T7 promoter, 6xHis tag, V5 epitope, Cm^{R} gene, and ccdB gene flanked by attR1/attR2 recombination sites. This DEST17 fragment was then cloned into the HindIII site in pACYC184. The Tet^{R} gene was rendered nonfunctional in the pACYC184 vector. Enhanced GFP (S65T) [184] was PCR amplified from pFA6a vector [185] in two steps. First, the internal NdeI site was destroyed by amplifying the 5' end of the gene using the primers 5'-ggaattccatatggtcagtaaaggagaagaacttttcactgg-3' and 5'-gccgtttcatgtgatctgggtatcttg-3'. The resulting 200 bp PCR product was used as a primer along with 5'ggaattccatatgtttgtatagttcatccatgccatgtg-3'to amplify the full length GFP gene flanked by NdeI sites and lacking a stop codon. This fragment was then cloned in frame into the pACYC184-DEST17 plasmid using the unique NdeI site in DEST17 to produce pNGFP. The C-terminal GFP destination vector pCGFP was also derived from pACYC184. The DEST42 cassette (nt 311-2107) was PCR amplified from pET-DEST42 (Invitrogen) as a HindIII-NdeI/HindIII fragment using the primers 5'-cccaagcttgcgaaattaatacgactcac-3' and 5'-cccaagcttcatatgcaccactttgtacaagaaagc-3'. The resulting fragment included the T7 promoter, lac operator (*lacO*), Cm^{R} gene, and ccdB gene flanked by attR1/attR2 recombination sites. The PCR product was cloned into the HindIII site of pACYC184, which unintentionally destroyed the Tet^{R} gene. GFP was then PCR amplified as described above with the exception that the reverse primer 5’-ggaattccatatgctatttgtatagttcatcc-3’ was used to add a stop codon to the GFP PCR fragment. The resulting product was digested with NdeI and cloned into pACYC184-DEST42 plasmid using the engineered NdeI site on the 3’end of the of DEST42 cassette.

2.2.4. Construction of DivIVA destination vectors

The N-terminal DivIVA destination vector pNDIV was constructed utilizing the pBAD24 vector backbone with the arabinose inducible promoter P_{BAD}. DivIVA (~500 nt) was PCR amplified from *B. subtilis* genomic DNA using the primers 5’-catgccatggctatgcaattaacgccaaatg-3’ and 5’-gctctagattccttttcctcaaatacagc-3’ and cloned into pBAD24 as a NcoI-XbaI fragment. The DEST14 cassette (nt 67-1912) including both Cm^{R} and ccdB genes flanked by attR1/attR2 recombination sites was PCR amplified from pDEST14 (Invitrogen) as a XbaI-SphI fragment using the primers 5’-gctctagaacaagtttgtacaaaaaagctgaacg-3’ and 5’acatgcatgcaccactttgtacaagaaagctgaacg-3’. The resulting PCR product was cloned in frame with DivIVA using the engineered XbaI site to produce pNDIV. A control plasmid pNDIV-GFP was constructed by cloning GFP in frame immediately upstream of DivIVA. Briefly, DivIVA was PCR amplified from B. subtilis genomic DNA as a NcoI/NdeI-XbaI fragment using the primers 5’-catgccatggctcatatgccattaacgccaaatg-3’ and 5’-gctctagattccttttcctcaaatacagc-3’. The DivIVA fragment was digested with NcoI and XbaI and cloned into pBAD24. The DEST14 cassette was then cloned into pBAD24-DivIVA as a XbaI-SphI fragment as described above. GFP was amplified as a NdeI-NdeI fragment using pNGFP as a template which resulted in a GFP PCR product flanked by NdeI sites lacking a stop codon. The GFP fragment was then digested and cloned into the engineered NdeI site of pBAD24-DivIVA-DEST14 to produce pNDIV-GFP. The C-terminal DivIVA destination vector pCDIV was constructed using pBAD24 as the vector backbone. The DEST14 cassette was PCR amplified from pDEST14 (Invitrogen) as a Acc651-XbaI fragment using the primers 5'-ccggtacccacaagtttgtacaaaaaagctgaacg- 3' and 5'-gctctagaaccactttgtaacaagaaagctg -3' and cloned into pBAD24 to produce pBAD24-DEST14. DivIVA was PCR amplified from B. subtilis genomic DNA with flanking XbaI and HindIII restriction sites using the primers 5'-gctctagagatgccattaacgccaaatg-3' and 5'-gggaagcttttattccttttcctcaaatacagc-3' and subsequently cloned into pBAD24-DEST14 to produce pCDIV. The GFP control plasmid, pCDIV-GFP, was constructed by PCR amplifying DivIVA as a XbaI-NdeI/HindIII fragment without a stop codon using the primers 5'-gctctagagatgccattaacgccaaatg-3' and 5'-gggaagcttcatatgttccttttcctcaaatacagc-3' and cloned into pBAD24-DEST14. GFP was then PCR amplified as an NdeI-NdeI fragment as described above and cloned into the engineered NdeI site to produce pCDIV-GFP. All vectors were sequence verified.

2.2.5. Construction of expression vectors

Oligonucleotide primers including *attB1* and *attB2* recombination sequences were used to PCR amplify a gene of interest. *R. palustris* genes were amplified from genomic DNA as described [28]. Yeast Importin α (karyopherin α) was amplified from pProEX-HTb expression vector [181, 186] and the variant NLS sequences were synthesized from oligos. Both BP and LR recombination reactions were performed as described by Invitrogen [180]. Correct inserts were verified by PCR and gel electrophoresis. The vectors used in this study are listed in Table 2.1.

Table 2.1 Plasmids used in the co-localization assay

Plasmid	Relevant Characteristics	Source or reference
pDONR221	Gateway® pDONR™ Vector, Km^r	Invitrogen
pDEST14	Gateway® pDEST™ Vector, Amp^r Cm^r	Invitrogen
pDEST17	Gateway® pDEST™ Vector, Amp^r Cm^r	Invitrogen
pET-DEST42	Gateway® pDEST™ Vector, Amp^r Cm^r	Invitrogen
pBAD24	P_{BAD} promoter from *araBAD* operon, Amp^r	[187]
pACYC184	Tet^r Cm^r	[188]
DivIVA Destination Vectors		
pNDIV	pBAD24 backbone with P_{BAD}-divIVA-dest14, Amp^r	This study
pCDIV	pBAD24 backbone with P_{BAD}- dest14-divIVA, Amp^r	This study
pNDIV-GFP	pBAD24 backbone with P_{BAD}-GFP-divIVA-dest14, Amp^r	This study
pCDIV-GFP	pBAD24 backbone with P_{BAD}- dest14-divIVA-GFP, Amp^r	This study
DivIVA Expression Clones		
pNDIV479	P_{BAD}-divIVA-Impα(mut), Amp^r	This study
pNDIV558	P_{BAD}-divIVA-Full length Impα, Amp^r	This study
pNDIV505	P_{BAD}-divIVA-BPSV40A4, Amp^r	This study
pNDIV501	P_{BAD}-divIVA-Myc, Amp^r	This study
pNDIV463	P_{BAD}-divIVA-SV40, Amp^r	This study
pNDIV488	P_{BAD}-divIVA-BPSV40T3, Amp^r	This study
pNDIV502	P_{BAD}-divIVA-MycA6, Amp^r	This study
pNDIV528	P_{BAD}-divIVA-SV40A5, Amp^r	This study
pNDIV499	P_{BAD}-divIVA-SV40E, Amp^r	This study
pNDIV503	P_{BAD}-divIVA-MycA8, Amp^r	This study
pNDIV469	P_{BAD}-divIVA-SV40A7E, Amp^r	This study
pNDIV504	P_{BAD}-divIVA-SV40A4, Amp^r	This study
pNDIV529	P_{BAD}-divIVA-SV40R3, Amp^r	This study
pNDIV530	P_{BAD}-divIVA-SV40T3, Amp^r	This study
pNDIV648	P_{BAD}-divIVA-MycA4, Amp^r	This study
pNDIV33	P_{BAD}-divIVA-GroES2, Amp^r	This study
pNDIV47	P_{BAD}-divIVA-GroEL2, Amp^r	This study
pNDIV110	P_{BAD}-divIVA-GroES1, Amp^r	This study
pNDIV113	P_{BAD}-divIVA-GroEL1, Amp^r	This study
pNDIV223	P_{BAD}-divIVA-HPr, Amp^r	This study
pNDIV218	P_{BAD}-divIVA-HPr kinase, Amp^r	This study
pNDIV65	P_{BAD}-divIVA-NifH, Amp^r	This study
pNDIV99	P_{BAD}-divIVA-NifD, Amp^r	This study
pNDIV101	P_{BAD}-divIVA-NifK, Amp^r	This study
pNDIV334	P_{BAD}-divIVA-RPA2336, Amp^r	This study
pNDIV333	P_{BAD}-divIVA-RPA2334, Amp^r	This study
pCDIV480	P_{BAD}- Impα(mut)-divIVA, Amp^r	This study
pCDIV560	P_{BAD}- Full length Impα-divIVA, Amp^r	This study
pCDIV511	P_{BAD}- BPSV40A4-divIVA, Amp^r	This study
pCDIV507	P_{BAD}- Myc-divIVA, Amp^r	This study
pCDIV465	P_{BAD}- SV40-divIVA, Amp^r	This study
pCDIV489	P_{BAD}- BPSV40T3-divIVA, Amp^r	This study
pCDIV408	P_{BAD}- MycA6-divIVA, Amp^r	This study
pCDIV531	P_{BAD}- SV40A5-divIVA, Amp^r	This study
pCDIV470	P_{BAD}- SV40E-divIVA, Amp^r	This study
pCDIV509	P_{BAD}- MycA8-divIVA, Amp^r	This study
pCDIV471	P_{BAD}- SV40A7E-divIVA, Amp^r	This study
pCDIV510	P_{BAD}- SV40A4-divIVA, Amp^r	This study
pCDIV532	P_{BAD}- SV40R3-divIVA, Amp^r	This study
pCDIV533	P_{BAD}- SV40T3-divIVA, Amp^r	This study
GFP Destination Vectors		
pNGFP	pACYC184 backbone with T7-GFP-dest17, Cm^r	This study
pCGFP	pACYC184 backbone with T7-dest42-GFP, Cm^r	This study

Table 2.1 Continued

Plasmid	Relevant Characteristics	Source or reference
GFP Expression Clones		
pNGFP48	T7-GFP- Impα(mut), Cm^r	This study
pNGFP562	T7-GFP- Full length Impα, Cm^r	This study
pNGFP517	T7-GFP-BPSV40A4, Cm^r	This study
pNGFP513	T7-GFP-Myc, Cm^r	This study
pNGFP467	T7-GFP-SV40, Cm^r	This study
pNGFP484	T7-GFP-BPSV40T3, Cm^r	This study
pNGFP514	T7-GFP-MycA6, Cm^r	This study
pNGFP534	T7-GFP-SV40A5, Cm^r	This study
pNGFP486	T7-GFP-SV40E, Cm^r	This study
pNGFP515	T7-GFP-MycA8, Cm^r	This study
pNGFP472	T7-GFP-SV40A7E, Cm^r	This study
pNGFP516	T7-GFP-SV40A4, Cm^r	This study
pNGFP535	T7-GFP-SV40R3, Cm^r	This study
pNGFP536	T7-GFP-SV40T3, Cm^r	This study
pNGFP650	T7-GFP-MycA4, Cm^r	This study
pNGFP138	T7-GFP-GroEL1, Cm^r	This study
pNGFP49	T7-GFP-GroEL2, Cm^r	This study
pNGFP112	T7-GFP-GroES1, Cm^r	This study
pNGFP45	T7-GFP-GroES2, Cm^r	This study
pNGFP67	T7-GFP-NifD, Cm^r	This study
pNGFP106	T7-GFP-NifH, Cm^r	This study
pNGFP68	T7-GFP-NifK, Cm^r	This study
pNGFP347	T7-GFP-RPA2334, Cm^r	This study
pNGFP348	T7-GFP-RPA2336, Cm^r	This study
pNGFP349	T7-GFP-RPA2338, Cm^r	This study
pCGFP482	T7- Impα(mut)-GFP, Cm^r	This study
pCGFP482	T7- Full length Impα-GFP, Cm^r	This study
pCGFP523	T7-BPSV40A4-GFP, Cm^r	This study
pCGFP519	T7-Myc-GFP, Cm^r	This study
pCGFP468	T7-SV40-GFP, Cm^r	This study
pCGFP485	T7-BPSV40T3-GFP, Cm^r	This study
pCGFP520	T7-MycA6-GFP, Cm^r	This study
pCGFP537	T7-SV40A5-GFP, Cm^r	This study
pCGFP487	T7-SV40E-GFP, Cm^r	This study
pCGFP521	T7-MycA8-GFP, Cm^r	This study
pCGFP473	T7-SV40A7E-GFP, Cm^r	This study
pCGFP522	T7-SV40A4-GFP, Cm^r	This study
pCGFP538	T7-SV40R3-GFP, Cm^r	This study
pCGFP539	T7-SV40T3-GFP, Cm^r	This study
pCGFP651	T7-MycA4-GFP, Cm^r	This study
pCGFP135	T7-GroES2-GFP, Cm^r	This study
pCGFP136	T7-GroES1-GFP, Cm^r	This study
pCGFP137	T7-GroEL1-GFP, Cm^r	This study
pCGFP211	T7-HPr-GFP, Cm^r	This study
pCGFP212	T7-HPr kinase-GFP, Cm^r	This study
pCGFP142	T7-NifD-GFP, Cm^r	This study
pCGFP200	T7-NifH-GFP, Cm^r	This study
pCGFP201	T7-NifK-GFP, Cm^r	This study

2.2.6. Co-localization assay

Expression vectors were co-transformed in BL21(DE3) for protein expression. Images of live cells expressing GFP-fusion proteins were captured using a Leica TCS SP2 scanning confocal microscope equipped with a Leica HCX PL APO 63x/1.40-0.60 oil objective lens. Leica LCS software (version 1537) was used to acquire images. Following induction of DivIVA-fusion protein expression with 0.2% L-arabinose for 1 hr at 37°C, images were collected again to determine the localization pattern of the GFP-fusion protein. The criterion for a positive interaction was met if at least 50% of the cells exhibited GFP-fusion protein localization at both poles of the cells (and/or an extra medial localization pattern).

2.2.7. Yeast Two-Hybrid

Truncated Impα and various NLS sequences were cloned into ProQuest Two-Hybrid vectors pDEST22 and pDEST32 according to the manufacturer’s instructions (Invitrogen). The resulting bait and prey plasmids were then co-transformed into *S. cerevisiae* MaV203 (*MATα*) cells grown in YPAD at 30°C. Synthetic Complete (SC) dropout medium lacking leucine and tryptophan was used to select for co-transformants. Positive two-hybrid interactions were detected by growth on SC medium lacking leucine, tryptophan, histidine, and uracil. β-galactosidase reporter enzyme activity was measured using the Galacto-Star chemiluminescent reporter assay system according to the manufacturer's instructions (Tropix Inc., Bedford, MA), with the exception that cells were lysed via glass bead disruption. Each sample was measured in triplicate. All **two-hybrid vectors are listed in Table 2.2.**

Table 2.2 Plasmids used for yeast two-hybrid experiments.

Plasmid	Relevant Characteristics	Source or reference
pDEST22	GAL4 activation domain (AD) destination vector; Amp^r, Cm^r	Invitrogen
pDEST32	GAL4 DNA binding domain (DB) destination vector; Gm^r, Cm^r	Invitrogen
pDBLeu	DNA Binding Domain .(DB) cloning vectors lacking *attR* sites; Km^r	Invitrogen
pEXP-AD502	Activation domain (AD) expression vector; Amp^r	Invitrogen
Y2H expression vectors		
pDEST544	AD-Impα(mut)	This study
pDEST643	AD-BPSV40A4	This study
pDEST641	AD-Myc	This study
pDEST545	AD-SV40	This study
pDEST640	AD-BPSV40T3	This study
pDEST637	AD-MycA6	This study
pDEST546	AD-SV40A5	This study
pDEST639	AD-SV40E	This study
pDEST638	AD-MycA8	This study
pDEST644	AD-SV40A7E	This study
pDEST642	AD-SV40A4	This study
pDEST547	AD-SV40R3	This study
pDEST548	AD-SV40T3	This study
pDEST707	AD-MycA4	This study
pDEST549	DB-Impα(mut)	This study
pDEST657	DB-BPSV40A4	This study
pDEST653	DB-Myc	This study
pDEST550	DB-SV40	This study
pDEST652	DB-BPSV40T3	This study
pDEST654	DB-MycA6	This study
pDEST551	DB-SV40A5	This study
pDEST655	DB-MycA8	This study
pDEST656	DB-SV40A4	This study
pDEST552	DB-SV40R3	This study
pDEST553	DB-SV40T3	This study
pDEST708	DB-MycA4	This study

2.3. Results

2.3.1. Vector construction

To facilitate rapid cloning and analysis of predicted interacting proteins, we constructed new, compatible DivIVA and GFP expression vectors based on site-specific recombination technology rather than traditional restriction enzyme cloning. Since the position of the molecular tag can have a large impact on fusion protein folding, stability, and function, we constructed a full complement of expression vectors encoding both N- and C-terminal DivIVA and GFP fusions. The DivIVA vectors are based on a pBAD24 backbone and DivIVA-fusion protein expression is tightly regulated by the P_{BAD} arabinose inducible promoter [187]. Plasmids pNDIV and pCDIV encode an N- and C-terminal DivIVA-fusion respectively (Figure 2.1A, C). These vectors were constructed using a Gateway recombination cassette from pDEST14 (Invitrogen) to produce an in frame DivIVA-fusion with any gene of interest following a site-specific recombination reaction. To validate that DivIVA-fusion proteins localize to the cell pole as expected, control plasmids pNDIV-GFP and pCDIV-GFP were constructed to express DivIVA-GFP fusion proteins that can be easily tracked in the cell using fluorescence microscopy (Figure 2.1B, D). GFP expression vectors pNGFP and pCGFP are derived from the pACYC184 backbone and GFP-fusion protein expression is controlled by an inducible T7 promoter [188]. The pACYC184-based GFP expression vectors include a Gateway recombination cassette derived from pDEST17 (Invitrogen) for N-terminal GFP fusions or from pET-DEST42 (Invitrogen) for C-terminal GFP fusions (Figure 2.1E, F). As expected, cloning proved to be highly robust as at least 95% of transformants contained the expected gene of interest fused to

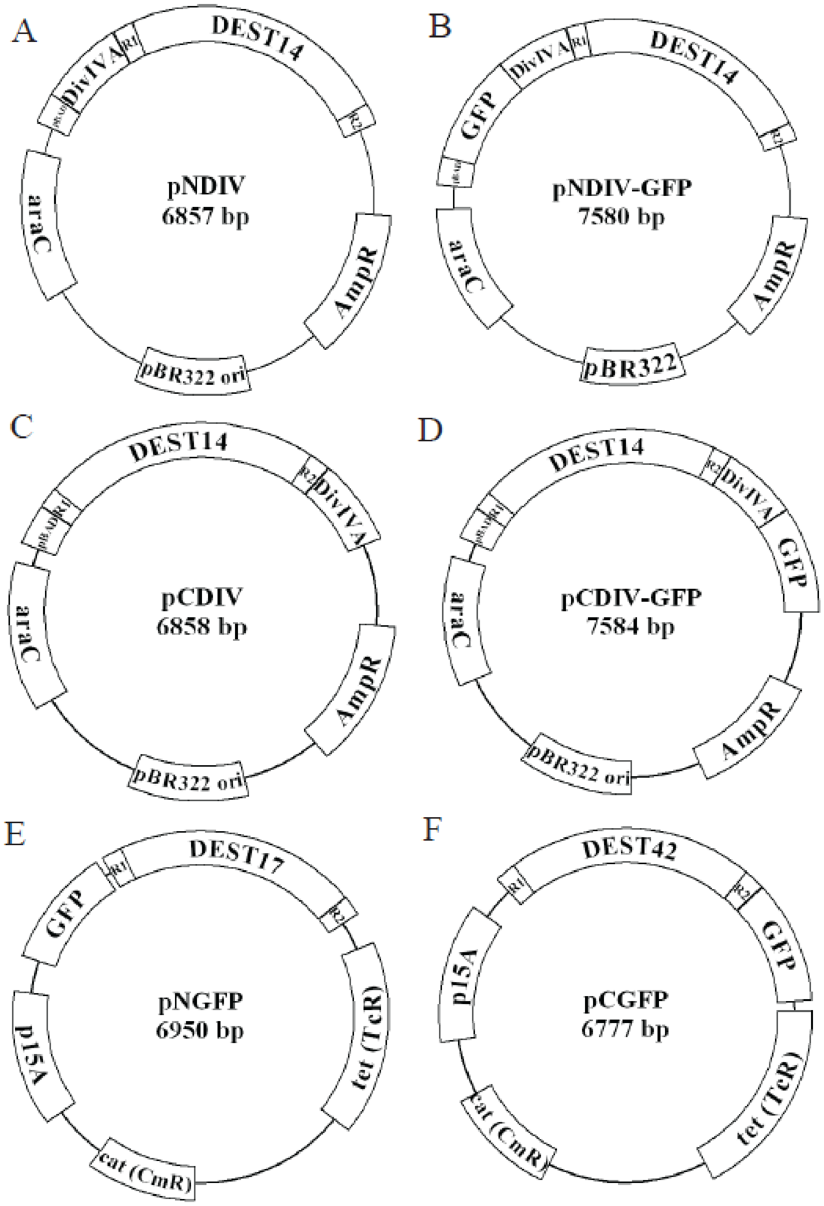

Figure 2.1 Gateway destination vector maps. (A, B) N-terminal DivIVA and DivIVA-GFP fusion vectors. (C, D) C-terminal DivIVA and DivIVA-GFP fusion vectors. All vectors encoding DivIVA-fusion proteins are based on the pBAD24 vector backbone with a pBAD arabinose-inducible promoter. (E) N-terminal GFP fusion vector. (F) C-terminal GFP fusion vector. All vectors encoding GFP-fusion proteins are based on the pACYC184 vector backbone with a T 7 inducible promoter. Vector maps were created in pDRAW32 (http://www.acaclone.com). P = promoter.

DivIVA or GFP following a site-specific recombination reaction. Clones with a correct insert were easily identified using PCR methods or restriction enzyme analysis.

2.3.2. Validation of Gateway destination vectors

To establish the functionality of the new vector set, we focused on testing the well-characterized interaction between yeast Impα and the NLS wtSV40 [182]. Previous biophysical characterization studies of this interaction pair indicate a strong affinity, with a K_d of 9 nM for Impα/wtSV40 [76, 78]. Yeast Impα is a 60 kDa protein which forms a complex with Impβ and mediates the transport of proteins through the nuclear pore complex via recognition of short nuclear localization signals. For this study, the N-terminal autoinhibitory Impβ binding (IBB) domain of Impα was deleted such that Impα will bind NLS-containing substrates when expressed in the absence of Impβ. In addition to the N-terminal truncation, a mutation (Tyr397Asp) is present in Impα to prevent homodimerization [181]. Truncated Impα expresses well in *E. coli*, is highly stable, and the C-terminal binding domain recognizes NLSs without the presence of their host proteins [75, 76].

The full complement of expression vectors (pNGFP, pCGFP, pNDIV, and pCDIV) was constructed for *S. cerevisiae* truncated Impα and wtSV40 NLS. Pairwise combinations of GFP and DivIVA expression vectors were then co-transformed into *E. coli* BL21 (DE3) cells for fusion protein expression and transformants were selected by growth on LB plates containing ampicillin and chloramphenicol. Following inoculation and overnight growth at 37°C in liquid LB medium containing antibiotics, cells were screened for GFP-fusion protein expression using fluorescence microscopy. GFP-fusion protein expression was detected even without induction of the T7 promoter with IPTG (Figure 2.2A and data not shown). Occasionally inclusion bodies

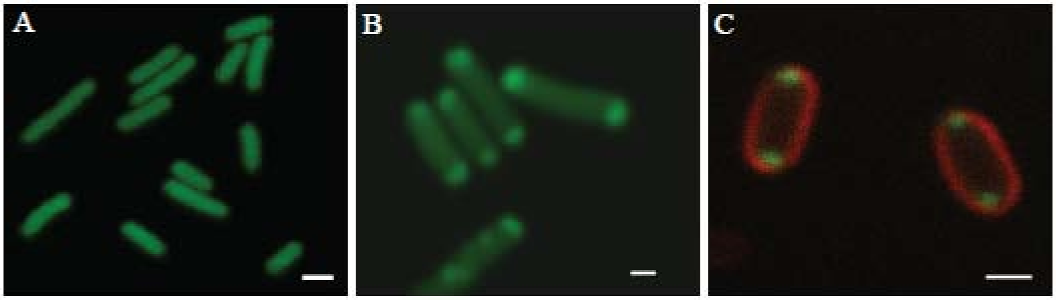

Figure 2.2 Validation of new co-localization assay vector set. (A, B) Images of cells showing GFP-wtSV40 NLS localization before (A) and after (B) induction of Impα-DivIVA expression. The localization pattern of GFP-wtSV40 NLS is consistent with a positive interaction between Impα and wtSV40 NLS. (C) Images of control cells showing Impα DivIVA-GFP localization to the cell poles. To define individual cells, the cell membrane was stained with FM 5-95 (Invitrogen). All scale bars represent 1 μm.

were observed, which may have resulted from overexpression or improper folding of the GFP-fusion protein (data not shown). In these situations, prevention of inclusion body formation could often be achieved in overnight cultures by lowering growth temperatures or adjusting media composition. This initial visualization of the GFP-fusion protein expression pattern also provided information on whether the expressed protein displayed an intrinsic localization pattern, which could affect interpretation of the assay. After confirmation of GFP-fusion protein expression, arabinose was added to the growth medium to induce expression of the DivIVA-fusion protein and the cells were incubated for an additional 60 minutes at 37°C. The cells were then observed again by fluorescence microscopy to determine whether there was a change in GFP-fusion protein localization. A positive interaction was indicated between the proteins of interest if the GFP-fusion protein was recruited to the cell poles after induction of DivIVA-fusion protein expression. The presence of three localization sites, one at each pole and one at the mid-cell (DivIVA localizes to the mid-cell during cellular division) was also considered a positive interaction. Conversely, the proteins of interest were determined not to interact if the GFP-fusion protein remained diffusely distributed in the cell or localized to only one pole. A positive protein interaction was indicated only if 50% or more of the cells in the population met these decision rule criteria.

As expected, interactions were detected between Impα and wtSV40 NLS using the co-localization assay. The position of the fluorescent tag did have an impact on the results. For example, when GFP was fused to the C-terminus of wtSV40 NLS, it did not interact with Impα-DivIVA. When the GFP tag was switched to N-terminus of wtSV40 NLS, however, we were able to detect a positive interaction (Figure 2.2B). These data illustrate the impact that molecular tag position has on detecting positive interactions and underscore the rationale for constructing both N- and C-terminal GFP and DivIVA expression vectors. To confirm localization of Impα-DivIVA fusion to the cell poles, we expressed control cells with Impα-DivIVA-GFP (Figure 2.2C).

2.3.3. Sensitivity analysis

We next wanted to test the sensitivity of the co-localization assay to determine the range of binding affinities that can be detected using this method. The truncated Impα and variant NLS interaction pairs are ideal candidates for investigating the assay sensitivity due to the broad spectrum of known dissociation constants (K_d) derived from fluorescence polarization studies [76, 78]. By mutating different amino acids in the NLS, Hodel and colleagues constructed a set of NLS variants and measured their affinity for truncated yeast Impα, revealing dissociation constants ranging from <1 nm to >15 μM [78]. For this study, we selected 13 NLS sequences representing a wide range of binding affinities and constructed the full set of N- and C-terminal DivIVA and GFP expression vectors (Table 2.3). Using the co-localization assay, we detected interactions between Impα and all of the variant NLS peptides (Figure 2.3 and data not shown). To determine whether these interactions were specific, we tested whether the variant NLS peptides could interact with full length Impα. Full length Impα has a relatively low affinity for NLSs due to the presence of an N-terminal autoinhibitory region on the Importin β-binding (IBB) domain [182]. When expressed alone in *E. coli*, full length Impα-GFP was diffusely distributed in the cells (Figure 2.4A). When full length Impα-GFP was co-expressed with various NLS-DivIVA constructs, we did not observe interactions between full length Impα and NLSs, indicating that the interactions detected by the co-localization assay between truncated Impα and

Table 2.3. Binding affinities and assay results for truncated Impα and NLS variants. Binding affinities between truncated yeast Impα and NLS sequences were determined by fluorescence polarization experiments reported in previous work by Hodel et. al. [76, 78]. The prototype unipartite NLS is from the large T antigen (TAg) of the simian vacuolating virus 40 (SV40). Its sequence is PKKKRKV, where the six underscored resides (P1–P6) bind in six pockets of Impα. Bipartite NLSs feature two basic clusters where the C-terminal basic cluster corresponds to P1–P6 of the SV40 NLS, and the N-terminal basic residues (KR, P10–P20) bind in a second pocket on Impα. The mutated residues for each NLS are underlined. (+) indicates a positive interaction detected between truncated Impα and the NLS variant indicated using either the co-localization assay or the yeast two-hybrid assay. (–) indicates no interaction was detected between Impα and NLS. A positive interaction by the yeast two-hybrid assay was determined by colony growth on selective media and/or b-galactosidase activity above background levels. A positive interaction by the co-localization assay was determined by recruitment of the GFP-fusion protein to the cell poles after expression of the DivIVA-fusion protein.

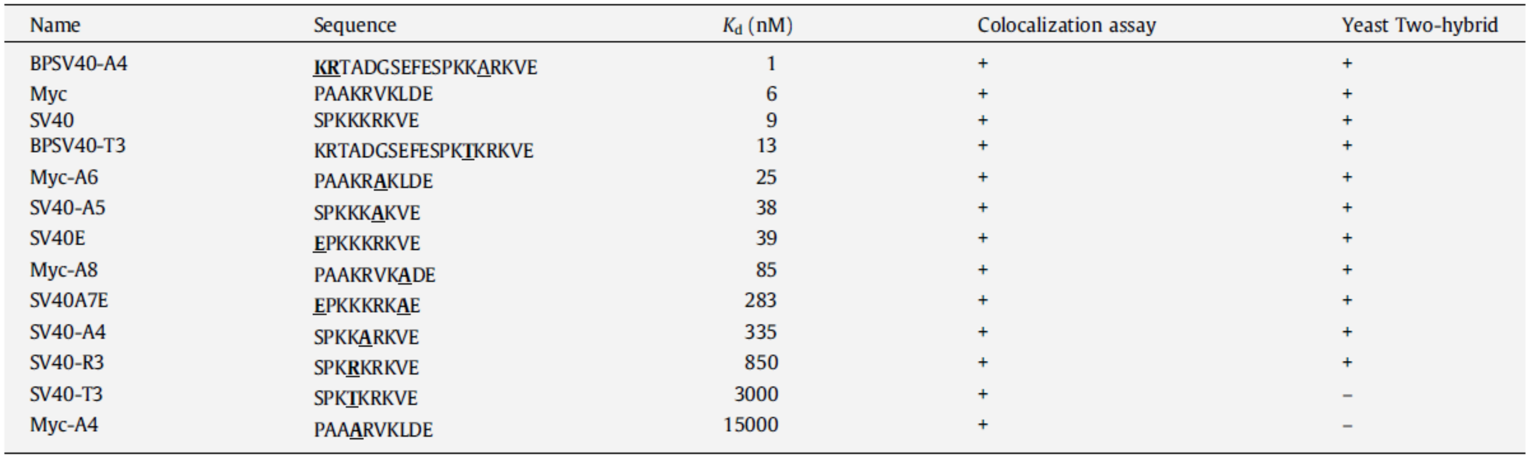

Name	Sequence	K_d (nM)	Colocalization assay	Yeast Two-hybrid
BPSV40-A4	**KR**TADGSEFESPKK**A**RKVE	1	+	+
Myc	PAAKRVKLDE	6	+	+
SV40	SPKKKRKVE	9	+	+
BPSV40-T3	KRTADGSEFESPK**T**KRKVE	13	+	+
Myc-A6	PAAKR**A**KLDE	25	+	+
SV40-A5	SPKKK**A**KVE	38	+	+
SV40E	**E**PKKKRKVE	39	+	+
Myc-A8	PAAKRVK**A**DE	85	+	+
SV40A7E	**E**PKKKRK**A**E	283	+	+
SV40-A4	SPKK**A**RKVE	335	+	+
SV40-R3	SPK**R**KRKVE	850	+	+
SV40-T3	SPK**T**KRKVE	3000	+	–
Myc-A4	PAA**A**RVKLDE	15000	+	–

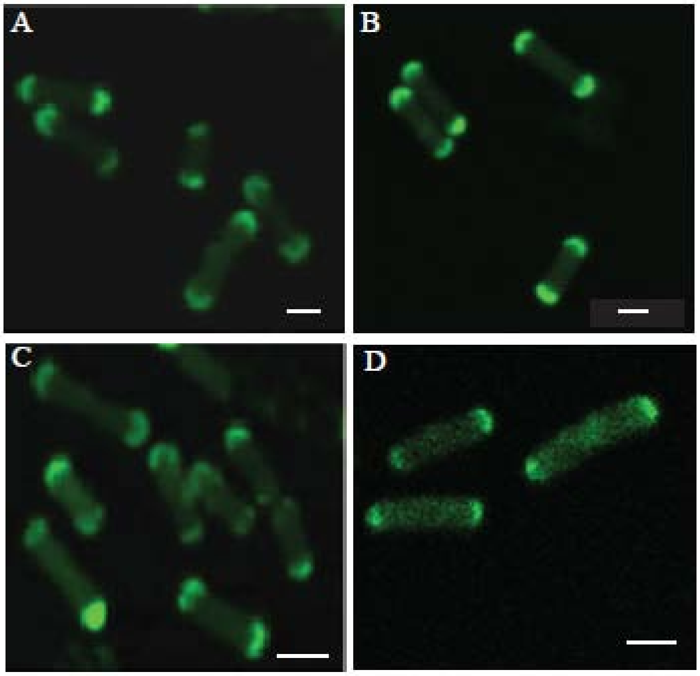

Figure 2.3 Detection of positive interactions between Impα and various NLS peptides. Images of live cells expressing GFP- and DivIVA-fusion proteins. Recruitment of the GFP-fusion protein to the poles indicates a positive interaction between the Impα and the indicated NLS peptide. (A) Cells expressing GFP-Impα and DivIVABPSV40A4, K_d: 1 nM. (B) Cells expressing GFP-Impα and DivIVA-SV40A5, K_d: 38 nM. (C) Cells expressing GFP-Impα and DivIVA-SV40A4, K_d: 335 nM. (D) Cells expressing Impα-GFP and DivIVA-MycA4, K_d: 15000 nM. All scale bars represent 1 µm.

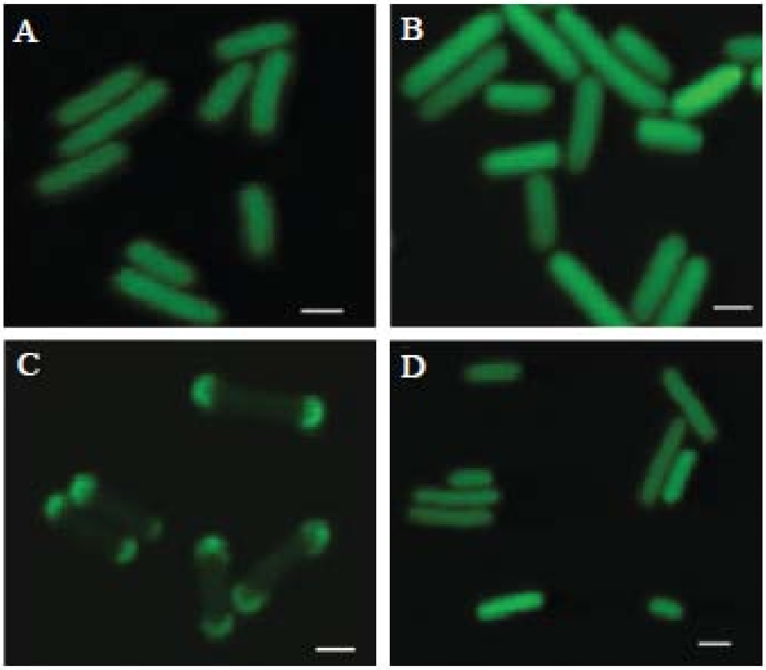

Figure 2.4 The interaction between SV40wt NLS is specific for truncated Impα. (A) Cells expressing full-length GFP-Impα only. (B) Cells expressing GFP-Impα (full length) and DivIVA-SV40wt. (C) Cells expressing GFP-Impα (truncated) and DivIVA-SV40wt, Kd: 9 nM. (D) Cells expressing GFP-Impα and DivIVA-SBP. Scale bars represents 1 µm.

NLSs were indeed specific (Figure 2.4 and data not shown). Additionally, truncated Impα was tested with streptavidin binding peptide (SBP) to evaluate the possibility that truncated Impα binds non-specifically to short peptides. An interaction was not observed between Impα and SBP, consistent with the hypothesis that the interaction between the variant NLS peptides and truncated Impα is specific (Figure 2.4D).

2.3.4. Comparison between the co-localization and yeast two-hybrid assays

These data establish that the co-localization assay is sensitive enough to detect protein interactions with dissociation constants as weak as 15μM. We next wanted to compare results obtained from this assay with results obtained using the well-characterized yeast two hybrid assay. To this end, we constructed vectors expressing DNA-binding domain (bait) or activation domain (prey) fusion proteins for Impα and all 13 NLS peptides listed in Table 2.3 and tested each pair wise combination for interaction using the ProQuest two hybrid assay (Invitrogen). The results of this comparison are shown in Table 2.3. Using the two hybrid assay, we detected interactions between Impα and all of the NLS peptides, except SV40T3 and MycA4. These NLS peptides were measured to have the weakest interactions with truncated Impα, with a K_d value of 3μM for SV40T3 and 15μM for MycA4 [78]. The orientation of fusion tags also influenced the results of this experiment. When Impα was fused to the DNA-binding domain (bait protein) and the NLS peptides were fused to the activation domain, we measured β-galactosidase activity above background levels for 11 out of the 13 interaction pairs. When the fusion proteins were switched such that Impα was fused to the activation domain (prey protein), β-galactosidase activity was only above background for one interaction pair (Impα and MycA6 NLS).

2.3.5. Detection of interactions in R. palustris using the co-localization assay

Having established the sensitivity of the co-localization assay, we next wanted to demonstrate its utility for high-throughput and directed protein interaction screens. To this end, we conducted a pilot study validating protein interactions identified in *R. palustris* by affinity isolation and mass spectrometry [28] or predicted by computational methods. In the *R. palustris* interactome mapping study, candidate bait proteins were PCR amplified from genomic DNA, recombined to produce an entry vector, and ultimately recombined into an expression plasmid to produce a V5-6xHis affinity-tagged protein. These expression plasmids were then individually transformed into *R. palustris* cells and the resulting fusion protein was affinity isolated along with its *in vivo* interaction partners. The co-purified proteins were then identified using mass spectrometry. Several putative protein interactions were then chosen for experimental validation by the co-localization assay, including interactions among two known protein complexes, a transient kinase-substrate interaction, and a predicted interaction between proteins of unknown function (Table 2.4). Using the existing recombination-based entry clones for *R. palustris* [28], we quickly produced a set of DivIVA and GFP expression vectors to test interactions using the co-localization assay (Table 2.1). Similar to our previous experience, cloning was very efficient and nearly all (approximately 95%) the clones contained the expected gene of interest fused to DivIVA or GFP following a site-specific recombination reaction.

One of the first complexes characterized in *R. palustris* was the GroEL-GroES chaperonin complex. The role of the GroEL-GroES chaperonin is to facilitate folding of proteins within the cellular environment. Two homologs of GroEL (GroEL1 and GroEL2) and GroES (GroES1 and GroES2) exist in *R. palustris* cells [189] and numerous interactions were detected

Table 2.4 *R. palustris* pairwise interactions tested by the assay. The columns marked “before” and “after” refer to the GFP-fusion protein localization pattern observed before and after addition of arabinose to the media to induce expression of the DivIVA fusion protein. “Cyto” indicates that the GFP-fusion protein was distributed throughout the cytoplasm, “poles” indicates that the GFP-fusion protein relocalized to the poles of the cells, and “IB” indicates the presence of inclusion bodies. The interpretation of the experiment is indicated in the column labeled “result.”“positive” refers to detection of an interaction between the proteins of interest, “negative” indicates that no interaction was detected; and “IB” indicates the presence of inclusion bodies which interfered with interpretation of the assay.

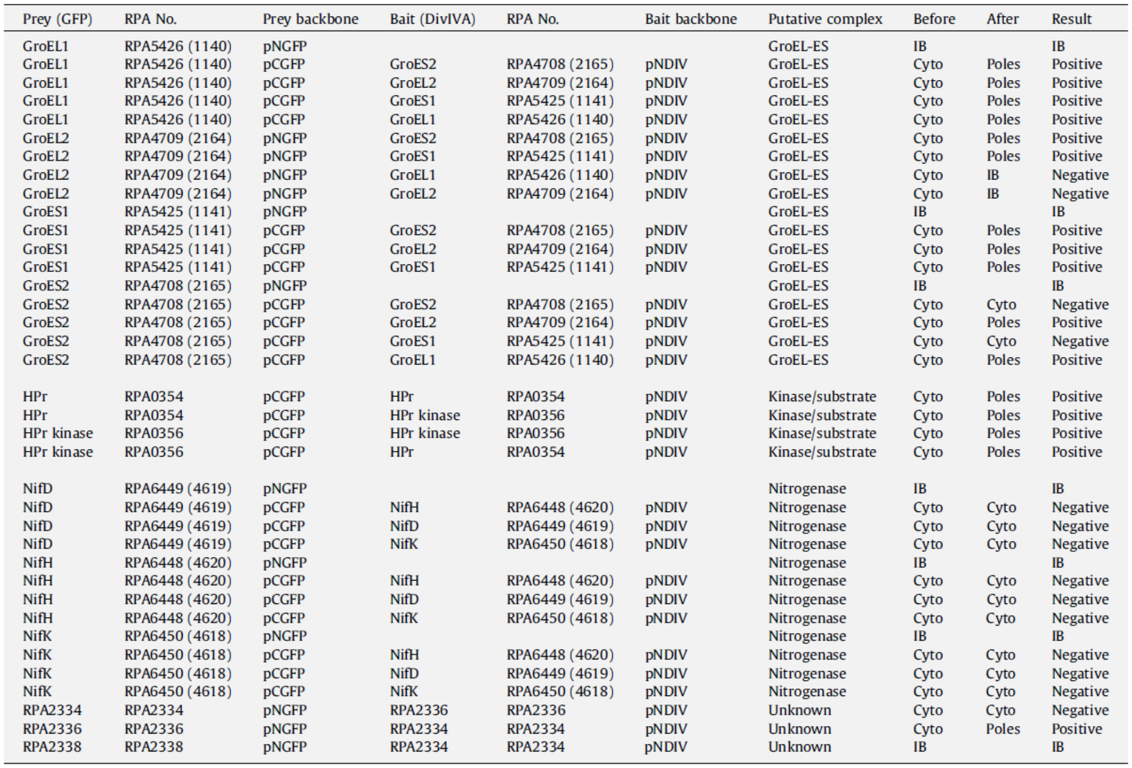

Prey (GFP)	RPA No.	Prey backbone	Bait (DivIVA)	RPA No.	Bait backbone	Putative complex	Before	After	Result
GroEL1	RPA5426 (1140)	pNGFP				GroEL-ES	IB		IB
GroEL1	RPA5426 (1140)	pCGFP	GroES2	RPA4708 (2165)	pNDIV	GroEL-ES	Cyto	Poles	Positive
GroEL1	RPA5426 (1140)	pCGFP	GroEL2	RPA4709 (2164)	pNDIV	GroEL-ES	Cyto	Poles	Positive
GroEL1	RPA5426 (1140)	pCGFP	GroES1	RPA5425 (1141)	pNDIV	GroEL-ES	Cyto	Poles	Positive
GroEL1	RPA5426 (1140)	pCGFP	GroEL1	RPA5426 (1140)	pNDIV	GroEL-ES	Cyto	Poles	Positive
GroEL2	RPA4709 (2164)	pNGFP	GroES2	RPA4708 (2165)	pNDIV	GroEL-ES	Cyto	Poles	Positive
GroEL2	RPA4709 (2164)	pNGFP	GroES1	RPA5425 (1141)	pNDIV	GroEL-ES	Cyto	Poles	Positive
GroEL2	RPA4709 (2164)	pNGFP	GroEL1	RPA5426 (1140)	pNDIV	GroEL-ES	Cyto	IB	Negative
GroEL2	RPA4709 (2164)	pNGFP	GroEL2	RPA4709 (2164)	pNDIV	GroEL-ES	Cyto	IB	Negative
GroES1	RPA5425 (1141)	pNGFP				GroEL-ES	IB		IB
GroES1	RPA5425 (1141)	pCGFP	GroES2	RPA4708 (2165)	pNDIV	GroEL-ES	Cyto	Poles	Positive
GroES1	RPA5425 (1141)	pCGFP	GroEL2	RPA4709 (2164)	pNDIV	GroEL-ES	Cyto	Poles	Positive
GroES1	RPA5425 (1141)	pCGFP	GroES1	RPA5425 (1141)	pNDIV	GroEL-ES	Cyto	Poles	Positive
GroES2	RPA4708 (2165)	pNGFP				GroEL-ES	IB		IB
GroES2	RPA4708 (2165)	pCGFP	GroES2	RPA4708 (2165)	pNDIV	GroEL-ES	Cyto	Cyto	Negative
GroES2	RPA4708 (2165)	pCGFP	GroEL2	RPA4709 (2164)	pNDIV	GroEL-ES	Cyto	Poles	Positive
GroES2	RPA4708 (2165)	pCGFP	GroES1	RPA5425 (1141)	pNDIV	GroEL-ES	Cyto	Cyto	Negative
GroES2	RPA4708 (2165)	pCGFP	GroEL1	RPA5426 (1140)	pNDIV	GroEL-ES	Cyto	Poles	Positive
HPr	RPA0354	pCGFP	HPr	RPA0354	pNDIV	Kinase/substrate	Cyto	Poles	Positive
HPr	RPA0354	pCGFP	HPr kinase	RPA0356	pNDIV	Kinase/substrate	Cyto	Poles	Positive
HPr kinase	RPA0356	pCGFP	HPr kinase	RPA0356	pNDIV	Kinase/substrate	Cyto	Poles	Positive
HPr kinase	RPA0356	pCGFP	HPr	RPA0354	pNDIV	Kinase/substrate	Cyto	Poles	Positive
NifD	RPA6449 (4619)	pNGFP				Nitrogenase	IB		IB
NifD	RPA6449 (4619)	pCGFP	NifH	RPA6448 (4620)	pNDIV	Nitrogenase	Cyto	Cyto	Negative
NifD	RPA6449 (4619)	pCGFP	NifD	RPA6449 (4619)	pNDIV	Nitrogenase	Cyto	Cyto	Negative
NifD	RPA6449 (4619)	pCGFP	NifK	RPA6450 (4618)	pNDIV	Nitrogenase	Cyto	Cyto	Negative
NifH	RPA6448 (4620)	pNGFP				Nitrogenase	IB		IB
NifH	RPA6448 (4620)	pCGFP	NifH	RPA6448 (4620)	pNDIV	Nitrogenase	Cyto	Cyto	Negative
NifH	RPA6448 (4620)	pCGFP	NifD	RPA6449 (4619)	pNDIV	Nitrogenase	Cyto	Cyto	Negative
NifH	RPA6448 (4620)	pCGFP	NifK	RPA6450 (4618)	pNDIV	Nitrogenase	Cyto	Cyto	Negative
NifK	RPA6450 (4618)	pNGFP				Nitrogenase	IB		IB
NifK	RPA6450 (4618)	pCGFP	NifH	RPA6448 (4620)	pNDIV	Nitrogenase	Cyto	Cyto	Negative
NifK	RPA6450 (4618)	pCGFP	NifD	RPA6449 (4619)	pNDIV	Nitrogenase	Cyto	Cyto	Negative
NifK	RPA6450 (4618)	pCGFP	NifK	RPA6450 (4618)	pNDIV	Nitrogenase	Cyto	Cyto	Negative
RPA2334	RPA2334	pNGFP	RPA2336	RPA2336	pNDIV	Unknown	Cyto	Cyto	Negative
RPA2336	RPA2336	pNGFP	RPA2334	RPA2334	pNDIV	Unknown	Cyto	Poles	Positive
RPA2338	RPA2338	pNGFP	RPA2334	RPA2334	pNDIV	Unknown	IB		IB

between these homologs using affinity isolation and mass spectrometry [28]. Whether these homologs are differentially regulated or promote folding of different populations of proteins in *R. palustris* remains unknown. Initially, all four proteins were expressed as N-terminal GFP-fusions and tested for localization in *E.coli*. Unexpectedly, all but GFP-GroEL2 formed inclusion bodies under these conditions (data not shown). When GFP was fused to the C-terminus of the proteins, however, no inclusion bodies were formed and the fusion proteins were distributed throughout the cell as expected. Using this assay, positive interactions were detected between GroES1-GroES2, GroEL1-GroEL2, GroES1-GroEL1, GroES1-GroEL2, GroES2-GroEL1, GroEL1-GroEL1, GroES1-GroES1, and GroES2-GroEL2 (Figure 2.5A, B and Table 2.4).

One of the reasons *R. palustris* was chosen as a model organism to study nitrogen metabolism is because its genome sequence predicts that it encodes a combination of almost all the regulatory and posttranslational modification mechanisms that are known to control nitrogen metabolism in other bacteria [189]. For this reason, we chose to look at interactions in the molybdenum nitrogenase complex. The Mo nitrogenase is composed of two components, the Fe-protein and the Mo-Fe protein. The Fe-protein is present as a homodimer that binds a single 4Fe-4S cluster (RPA4620, NifH). The Mo-Fe protein, which is the actual catalytic component of nitrogenase, is composed of alpha (RPA4619, NifD) and beta (RPA4618, NifK) subunits as a $\alpha2\beta2$ heterotetramer [190]. For the *R. palustris* interactome study, NifH, NifD, or NifK was expressed as a V5-6xHis fusion protein in cells grown under nitrogen fixing conditions. Following affinity isolation, mass spectrometry confirmed the presence of all three members of the nitrogenase complex in reciprocal isolations (Pelletier and Hurst, unpublished results). When expressed as N-terminal GFP fusions in *E. coli* for the co-localization assay, however, NifD,

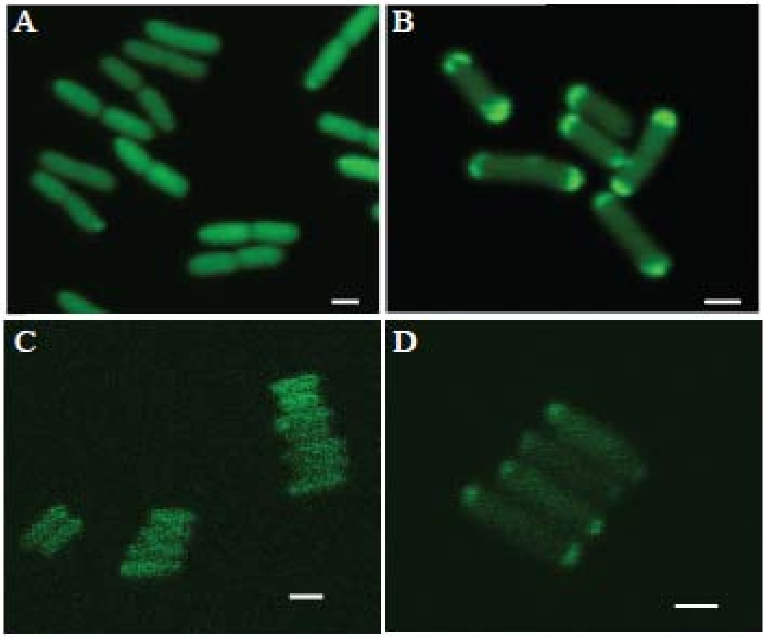

Figure 2.5. Detection of protein interactions from *R. palustris* (A, B) Images of cells showing GFP-GroEL2 localization before (A) and after (B) induction of DivIVA-GroES1 expression. Recruitment of GFP-GroEL2 to the cell poles is indicative of a positive interaction between GroES1 and GroEL2. (C, D) Images of cells showing Hpr kinase-GFP localization before (C) and after (D) induction of DivIVA-Hpr expression.
All scale bars represent 1 µm.

NifH, and NifK all formed inclusion bodies (Table 2.4). When the GFP tag was fused to the C-terminus of each Nif protein, however, the GFP fusion proteins were distributed in the cytoplasm. Nevertheless, we were unable to detect any interactions among the nitrogenase subunits using the co-localization assay (Table 2.4).

Another protein interaction that was tested by the co-localization assay is the predicted interaction between *R. palustris* Hpr (RPA0354) and Hpr kinase (RPA0356). This transient interaction is difficult to detect by affinity isolation and provided an opportunity to test the types of interactions that can be detected by the co-localization assay. The HPr- HPr kinase system is an important regulatory mechanism for sugar transport via the phosphoenolpyruvate:carbohydrate phosphotransferase system (PTS) and CcpA-mediated carbon catabolite repression in Gram-positive bacteria [191]. Biophysical characterization of this complex from *Staphylococcus xylosus* revealed that these proteins weakly associate, with a K_d of 100 µM [192]. Using the co-localization assay, we were able to detect an interaction between *R. palustris* Hpr and Hpr kinase, regardless of which protein was fused to GFP (Figure 2.5C, D and Table 2.4).

Finally, we used the co-localization assay to validate putative interactions among proteins of unknown function that are expressed during anaerobic growth in *R. palustris*. In the interactome mapping studies, a number of proteins predicted to be co-expressed as an anaerobic-induced operon were co-purified, including RPA2334, RPA2336, and RPA2338 (Pelletier and Hurst, unpublished results). Pairwise combinations of RPA2334, RPA2336, and RPA2338 were then tested for interactions using the co-localization assay. We were able to detect a positive interaction between RPA2334 and RPA2336, suggesting that at least these proteins form a complex in *R. palustris* (Table 2.4).

2.4. Discussion

Identifying and characterizing protein interactions are vital to understanding complex cellular systems. As genomic sequence data becomes available for an increasing number of organisms, focus is shifting toward elucidating how this genomic information is translated into dynamic, complex molecular networks capable of responding to environmental and genetic cues. Comparisons of interactomes among closely and distantly related organisms may reveal common regulatory and signaling networks and how these networks have evolved as organisms have adapted to different growth conditions and environments. Several high-throughput methods have been described to detect protein interactions, including affinity purification coupled with mass spectrometry, dihybrid screens, and fluorescence-based imaging assays. Although no one technique is capable of detecting all interactions, each method has advantages and disadvantages with respect to throughput, ease of use, cost, rapidity of results, sensitivity, and accuracy.

In this study, we report modification of an imaging-based protein interaction screen to facilitate either small scale protein network analyses or high-throughput screening applications. To this end, we have constructed and tested new recombination-compatible expression vectors to facilitate rapid and efficient cloning of potential interaction pairs. Cloning into these DivVIA- and GFP-fusion protein expression vectors can be fully automated using site-specific recombination reactions (Invitrogen), although we did not exploit this feature in this study. Both vectors have inducible promoters with GFP-fusion protein expression being driven by the T7 promoter and DivIVA-fusion protein expression being driven by the arabinose inducible promoter P_{BAD}. In our experience, GFP-fusion protein expression is detectible in *E. coli* BL21 (DE3) cells by fluorescence microscopy even without induction of the T7 promoter. In some cases, we observed the formation of inclusion bodies [193] rather than diffuse cellular localization of the GFP-fusion protein which is likely due to over expression or protein instability. Unfortunately, these inclusion bodies often localize to the cell poles thereby mimicking the GFP-fusion protein localization pattern for a positive interaction. For this reason, we routinely screen GFP-fusion protein localization patterns prior to induction of DivIVA-fusion protein expression and eliminate cultures containing inclusion bodies from further screening to reduce false positive identifications. In many cases, we can reduce inclusion body formation by lowering growth temperatures from 37°C to 30°C or 25°C or by adjusting media composition to slow cell growth. In addition, switching the position of the fusion tag from N- to C-terminus or vice versa often results in a more soluble protein that is distributed throughout the cell. Moreover, we have constructed both N- and C-terminal GFP and DivIVA expression vectors which allow testing of 4 different fusion tag orientations for each protein pair (N-terminal GFP + N-terminal DivIVA, N-terminal GFP + C-terminal DivIVA, C-terminal GFP + N-terminal DivIVA, and C-terminal GFP + C-terminal DivIVA) to maximize the protein interactions identified by this screen.

Once the localization pattern of the GFP-fusion protein is verified by fluorescence microscopy, L-arabinose is added to the media to a final concentration of 0.2% to induce DivIVA-fusion protein expression and the cells are incubated an additional 60 minutes. The cells are then imaged again to determine whether the GFP-fusion protein localization pattern changes in response to DivIVA-fusion protein expression. Namely, if the GFP-fusion protein is recruited to the cell poles, a positive interaction is indicated between the proteins of interest fused to GFP and DivIVA. Thus, the criteria for interpreting this assay are simple and amenable to automated image analysis [179]. Presently, we typically grow 1 ml cultures of *E. coli* cells transformed with both GFP and DivIVA expression plasmids and manually collect images before and after induction of the DivIVA-fusion protein. However, this assay could easily be scaled down to a micro-well plate format that would facilitate higher throughput studies.

The known binding affinities of Impα with 13 NLSs offered a broad dynamic range of K_d values for defining the co-localization assay sensitivity [78]. A positive interaction was detected for Impα and each NLS variant, revealing that the assay is sensitive enough to detect interactions with dissociation constants as weak as 15 µM. Since 15µM was the weakest dissociation constant represented in this data set, we have not determined the sensitivity limit for the co-localization assay. It is quite possible that weaker interactions can be detected; however these interactions are approaching the limit of what might be physiologically relevant. Using Impα and the same set of NLS variants, we determined that the yeast two hybrid assay was sensitive enough to detect an Impα-NLS interaction with a dissociation constant of 850 nM but not 3 µM or 15µM. Other published results have shown the yeast two hybrid assay to be more sensitive, with one report detecting a positive interaction with a dissociation constant of 70 µM [194]. Our inability to detect the weakest Impα-NLS interactions by two hybrid analysis may be due to several reasons. First, we cannot rule out the possibility of tag interference. Most of the positive interactions detected with the co-localization assay had both DivIVA and GFP fused to the N-terminus of the proteins of interest. One exception to this was the weakest interaction in which GFP was fused to the C-terminus of truncated Impα (Figure 2.3). In the commercial two hybrid assay used for this study, the DNA-binding and activation domains are fused to the N-terminus of the proteins of interest. Even after testing Impα as bait and prey, we were unable to detect a positive interaction with the NLS variants representing the weakest interactions (K_d 3µM or 15µM). The ability to test 4 fusion tag orientations rather than just two is an advantage of the co-localization assay and should reduce the occurrence of false negative results.

Another possible reason we did not detect the weakest Impα-NLS interactions by the yeast two hybrid assay may be due to competition for NLS binding between endogenous Impα and the Impα fusion protein. It seems likely that the truncated yeast Impα expressed for the two hybrid assay would have an affinity for endogenous NLS-containing proteins in the nucleus and this competition might interfere with the ability to detect a positive interaction. Further, one might expect this effect to be most pronounced with the weakest NLS variants as the endogenous substrates may have a higher affinity for the truncated Impα than the variant NLS peptides. In this particular case, testing Impα-NLS interactions in a heterologous host, such as *E. coli*, is advantageous since the effects of competition are significantly reduced.

Finally, we utilized the co-localization assay in a small scale protein interaction screen to test putative protein interactions in *R. palustris* identified by affinity isolation and mass spectrometry or predicted by computational methods. Because the expression plasmids used in the interactome mapping project were based on site-specific recombination, it was quick, easy, and cost-effective to obtain the relevant entry plasmids containing the genes of interest and recombine them into the DivIVA and GFP expression plasmids. The results of this small-scale screen illustrate some of the advantages and disadvantages of the assay. One advantage was the ability to test 4 different fusion tag orientations for each protein pair, which led to the detection of more positive interactions since we encountered a number of situations in which one pairwise orientation would produce a positive result while the other orientations led to a negative result or the formation of inclusion bodies. Since the cloning of genes of interest can be automated with this assay, it would be quite feasible to routinely test all 4 fusion tag orientations in a large scale screen. Using this assay, we confirmed the putative interaction between RPA2334 and RPA2336 identified from affinity isolation. These proteins are co-expressed during anaerobic growth in *R. palustris*, although their cellular function is unknown. It will be very interesting to conduct additional experiments to elucidate the role of this complex during anaerobic growth. Another advantage of this assay is the ability to detect weak and transient interactions, such as the interaction between *R. palustris* Hpr and Hpr kinase. Interestingly, the reported K_d for this interaction in *S. xylosus* is 100 µM, nearly an order of magnitude weaker than the weakest Impα-NLS interaction (15µM) included in our sensitivity analysis. It seems likely that the design of this assay in which proteins of interest are co-expressed in live cells rather than dilute buffers facilitates detection of weak and transient interactions based on crowding in the cellular environment. Although initial assumptions about Hpr-Hpr kinases suggested that these proteins were not present in Gram-negative bacteria based on their absence in enteric bacteria such as *E. coli*, recent genomic analysis has found that HPr-HPrK/P system is present in many proteobacteria. Since many of these organisms lack CcpA and a complete PTS, evidence indicates that HPr-HPrK/P may control transcription factors involved in virulence and cell adhesion [191]. Whether these proteins are involved in virulence and cell adhesion in *R. palustris* will require further experimentation.

The inability to detect interactions in the *R. palustris* nitrogenase complex illustrates a limitation of the co-localization assay; namely, that *E. coli* is not a suitable host for expression of some proteins. That no interactions were detected between NifK, NifH, and NifD is likely because the Mo nitrogenase operon encodes many of the accessory proteins responsible for proper folding and assembly of the nitrogenase complex. In addition, these accessory proteins are also involved in the synthesis of the Mo and Mo-Fe cofactors [190]. Since homologous pathways do not exist in *E. coli*, the assembly of these complexes may not be possible. Similarly, expression of eukaryotic proteins that are post-translationally modified is also compromised in a prokaryotic host. For this reason, the co-localization assay as it is described here may not be the best option for detecting some interactions. The issue of protein expression in heterologous hosts is not unique to the co-localization assay but is a general issue for all live cell assays. This limitation underscores the advantage to using multiple methods to map cellular networks since no single method can detect all protein interactions in a cell. It is important to note, however, that the general principle of the co-localization assay in which a fluorescently tagged protein re-localizes based on its interaction with a spatially confined protein could be adapted to other prokaryotic or even eukaryotic hosts.

The results presented here indicate that the co-localization assay is very sensitive for detecting a wide range of protein interactions and is well-suited for both selected network analysis and high-throughput screening applications. This assay should also be compatible with other fluorescence microscopy techniques, such as fluorescence recovery after photobleaching (FRAP), which could facilitate quantification of binding affinities. The ability to identify protein interactions and quantify binding affinities *in vivo* would represent a significant step towards understanding the mechanisms and regulation of protein interaction networks.

Chapter 3. Intracellular interactions: A FRAP-based method for quantification of binding affinities *in vivo*

This chapter is based on a manuscript in preparation. I conducted the experiments and acquired the FRAP data, where Jason D. Fowlkes developed the MatLab® routines to process and analyze the resulting FRAP data. All mathematical modeling and simulations were contributed by Dr. Fowlkes. Other co-authors include Robert F. Standaert, Mitchel J. Doktycz, Jennifer L. Morrell-Falvey who responded with editorial comments and additional text where needed.

3.1. Introduction and significance

Understanding and predicting cellular processes ultimately depend on identifying and quantifying the macromolecular interactions that drive them. As discussed in Chapter 1, PPIs have been traditionally measured by *in vitro* biochemical techniques, such as NMR, surface plasmon resonance, and fluorescence anisotropy. In recent years, the arrival of GFP fusion protein technology has led to advances in live cell fluorescence-based assays. Since the 1970s, fluorescence recovery after photobleaching (FRAP) has enabled researchers to quantify the mobility of protein in livings cells as a function of time [113, 118, 121]. FRAP assays not only assess diffusion of membrane associated or cytoplasmic proteins, but also address protein binding dynamics. More specifically, the rate of fluorescence recovery provides a measurement of diffusion through the cellular milieu and binding dynamics of the cellular components. Indeed, FRAP experiments have expanded beyond the examination of simple diffusion in cellular systems [114, 117, 121]. However, the majority of published FRAP experiments report qualitative interpretations of protein binding [113]. To this end, proteins are assumed to be weaker or tighter binders when faster or slower recoveries respectively, are observed [113]. Furthermore, the examples in Chapter 1 describe a number of experiments where FRAP is coupled with refined quantitative data analyses to extract rate constants.

Here, we present a unique methodology which combines the imaging-based co-localization assay (described in Chapter 2) with FRAP in order to quantify binding kinetics *in vivo*. This method was used to induce and maximize fluorescence contrast between bound and mobile protein. Exchange of this protein of interest with a binding partner located at the cell poles reveals information regarding the binding kinetics as bleached proteins exchange binding sites with their unbleached counterparts.   The time coordinate of the photobleaching takes place rapidly, relative to the dissociation rate of bound protein further ensuring that fluorescence photobleaching and binding are uncoupled. Ultimately, the rate of fluorescence recovery in the cell interior is determined by the binding interaction strength. Notably, this approach is, to our knowledge, the first general protein interaction screen which can be extended to acquisition of biophysical parameters. Two model protein interaction systems, Streptavidin/Streptavidin Binding Peptide (SBP) and Impα/NLSs, were used to develop the image processing techniques and analytical models for interpretation of FRAP recovery curves.

3.2. Materials and Methods

3.2.1. Bacterial strains and growth conditions

E. coli strains and growth conditions were performed as described in Chapter 2 with a few modifications. Briefly, for propagation of entry and expression clones, *E. coli* strains DH5α, BL21(DE3), and BL21(DE3)-AI (Invitrogen) were grown in Luria-Bertani (LB) medium, supplemented with 50 µg/ml kanamycin, 15 µg/ml chloramphenicol, or 50 µg/ml ampicillin as needed. For plasmid propagation, *E. coli* cultures were grown at 37ºC. For the co-localization assay and protein expression for His-tag purification, cultures were grown in 75% LB at 30ºC overnight.

3.2.2. Construction of entry clones and expression vectors

Impα and nuclear localization signal (NLS) clones used in this study were described previously in Chapter 2. All other expression clones were constructed in a similar manner. Streptavidin gene was PCR amplified from *Streptomyces avidinii* (ATCC 27419). Streptavidin binding peptide (SBP, [195]) was synthesized from oligos. Once cloned into Gateway entry vectors, BP and LR clonase recombination reactions were performed according to manufacturer's instructions (Invitrogen) to produce expression vectors. PCR reactions were performed using a GeneAmp thermocycler (PerkinElmer, Walthum, MA) with Vent or Phusion polymerase (New England Biolabs, Ipswich, MA). All oligonucleotides used as primers for this study were purchased from Integrated DNA Technologies (Coralville, Iowa) and reaction protocols were optimized according to the oligonucleotide specification.

3.2.3. Co-localization assay

The co-localization assay was conducted as described in Chapter 2. Slight modifications to the growth conditions, namely temperature and media concentrations, were made for each interaction pair to optimize protein expression and reduce the occurrence of inclusion body formation and cell elongation**.**

3.2.4. GFP concentration via ELISA

In vitro measurements of GFP concentration were determined by a commercially available GFP ELISA kit (Cell Biolabs, Inc) following the manufacturer's instructions. Briefly, cells expressing GFP fusions were grown overnight at 30°C. A 1.0 ml aliquot of the culture was harvested by centrifugation at 8000 rpm for 2 min and resuspended in 1 ml of BugBuster^{TM} (Novagen) supplemented with 1 µl of Benzonase Nuclease^{TM} (25 units/µl; Novagen) and 1 µl of

100 mg/ml lysozyme. To prevent protein degradation samples were also supplemented with Halt^{TM} protease inhibitor cocktail (Pierce Biotechnology, Rockford, IL) following the manufacturer's instructions. The resulting lysate was incubated on an orbital rotator for 20 minutes at 4˚C followed by sonication (3 pulses, 30 second duration, and 18% amplitude) with a Branson Digital Sonifier. The lysate was then centrifuged at 13,000 rpm for 30 min. A series of 10x dilutions were made with the assay diluent. The ELISA assay was preformed according to the provided protocol. The absorbance at 450 nm for each well was acquired with a BioTek Synergy 2 Multidection Microplate Reader**.** The remaining cell culture was prepared for fluorescence imaging and used to determine CFU.

3.2.5. FRAP protocol

FRAP experiments were performed on a Leica TCS SP2 scanning confocal microscope equipped with either a Leica HCX PL APO 63x/1.40-0.60 or a Leica HCX PL APO 100x/1.40-0.70 oil immersion objective lens. Leica LCS software (version 1537) FRAP application was used to collect pre-bleach, bleach, and post-bleach images. Additional post-bleach images were acquired manually to refocus the image for maximum fluorescence intensity. Bleaching was preformed with a rectangular region–of–interest (ROI). The photobleaching ROI was localized only to the cell interior thus avoiding the complications related to overlapping the photobleaching and binding events (i.e., binding events are localized at the cell poles). The bleach pulse was implemented by setting the 488-nm line of a 25 mW argon-krypton laser to (ATOF) of 100%. Fluorescence recovery was monitored at an acousto-optical tunable filter setting ATOF of 2-3% laser power, which was optimized for each experiment. Full description of FRAP parameters performed for Strep-SBP experiments and Impα-NLS are listed in Tables 3.1 and 3.2.

3.2.6. Fluorescence anisotropy binding assays

Fluorescence anisotropy was used to determine the dissociation constants and binding kinetics for GFP-NLS fusion proteins and Impα. A BioTek Synergy 2 Multidection Microplate Reader was used to monitor the anisotropy of GFP fluorescence at ambient temperature. The sample was excited with a xenon flash lamp passed though a 485/20 nm filter, and the fluorescence emitted from the sample was measured after passing through a 528/20 nm filter. The changes in anisotropy were recorded for 30 nM GFP-wtSV40 titrated with serial dilutions of purified Imp α (starting concentration of 2 μM) in 10 mM HEPES buffer, pH 7.4. To measure $k_{\mathrm{off},}$ an equilibrated solution of GFP-wtSV40 and purified Imp α with 1:1 stoichiometry was diluted 100x in 10 mM HEPES pH7.0. Anisotropy measurements were recorded every 15 to 20 sec for 30 min to acquire a disassociation curve. The curves for wtSV40, SV40A4, SV40A7E, and SV40T3 were fit with a first order exponential to derive k_{off}.

3.2.7. Protein purification and SDS-PAGE

His-tagged proteins expressed from pDEST17 or pNGFP were purified as follows. Expression vectors were transformed into E. coli BL21 (DE3) or BL21 (DE3) –A1 (Invitrogen) and resulting transformants were grown at 30˚C overnight. From the overnight culture, 0.5 ml was then used to inoculate 100 ml of LB medium. The culture was incubated at 37˚C until the OD_{600} reached 1.0. Cells were centrifuged at 5000 rpm for 20 min and resuspended in 15 ml of BugBuster$^{\mathrm{TM}}$ (Novagen) supplemented with 15 µl of Benzonase Nuclease$^{\mathrm{TM}}$ (25 units/µl; Novagen) and 15 µl of 100 mg/ml lysozyme. To prevent protein degradation samples were also

Table 3.1 Parameter settings for Strep-SBP FRAP.

Parameter	Setting	Notes
Pinhole	250	
Beam expander	3	
Format	256 x 256	
Mode	xyt	
Speed	1000 Hz	
Bleach laser intensity	30%	Laser power at source: 125 mW Laser power at focal plane: 25 mW
Pre-bleach images	2	
Bleach	1 laser pulse	
Post-bleach 1	6	
Post-bleach 2	50	Images acquired every 0.208 sec
Post-bleach 3	200	Images acquired every 0.208 sec
Laser intensity for image acquisition (ATOF setting)	3 % of bleach laser intensity	
Bleach laser type	ArKr 488 nm	

Table 3.2 Parameter settings for Impα-NLS FRAP.

Parameter	Setting	Notes
Pinhole	Default	
Beam expander	3	
Format	512 x 512	
Mode	xyt	
Speed	800 Hz	
Bleach laser intensity	100%	Laser power at source: 125 mW Laser power at focal plane: 25 mW
Pre-bleach images	5	
Bleach	10 laser pulses	
Post-bleach (program acquired)	5	
Post-bleach 2 (manual)	10-15 images	Captured at 5-10 min intervals
Laser intensity for image acquisition (ATOF) setting	2-2.5 % of bleach laser intensity	
Bleach laser type	ArKr 488 nm	

supplemented with Halt^{TM} protease inhibitor cocktail (Pierce Biotechnology, Rockford, IL) following the manufacturer's instructions. The cell lysate was incubated on an orbital rotator for at least 30 min at 4˚C and followed by sonication (3 pulses, 30 second duration, 18% amplitude) with a Branson Digital Sonifier. The lysate was then centrifuged at 11,000 rpm for 30 min and the soluble fraction was applied directly to His-Select Nickel Affinity Gel (column volume 2 ml; Sigma, Saint Louis, MO). The column was washed with 10 column volumes of wash buffer (50 mM NaH_2PO_4, 300 mM NaCl, 20 mM Imidazole) and eluted with 2 column volumes of the same buffer containing 500 mM imidazole. The purified GFP-fusion proteins were then added to an Amicon Ultra-15 filter column (Millipore) to exchange the elution buffer with 20 mM of HEPES buffer (pH 7.0). After the extraction procedure, both the soluble and insoluble fractions were boiled in SDS sample buffer (ref) and 5 µl was loaded onto a 7.5% or 12% Tris-HCl polyacrylamide gel (Bio-Rad) depending of the size of the GFP fusion protein. Gels were electrophoresed at 100V for 1 hr. The gels were then stained using SimplyBlue™ SafeStain (Invitrogen) following manufacturer's instructions to determine purity of protein.

3.2.8. GFP-Impα Western blots

Western blots were conducted to determine that GFP-Impα is maintained as a stable fusion *in vivo*. Cells expressing GFP-Impα were resuspended in a phosphate buffer (50 mM Na_2HPO_4; 300 mM NaCl, pH 8.0) supplemented with lysozyme (final concentration of 1 mg/ml) and Halt^{TM} protease inhibitor cocktail (Pierce Biotechnology, Rockford, IL) following the manufacturer's instructions. The cell lysate was sonicated (3 pulses, 30 second duration, 18% amplitude) with a Branson Digital Sonifier. The lysate was then centrifuged at 11,000 rpm for 30 min. SDS-PAGE was performed as described above and the protein was transferred to a

PVDF membrane using the iBlot® Dry Blotting System (Invitrogen). The membrane was blocked with 5% skim-milk in PBST for 1 hr followed by incubation with an anti-GFP rabbit-HRP conjugated primary antibody for 1hr. The membrane was thoroughly washed with PBST and visualized with a Metal-Enhanced DAB substrate kit (Thermo Scientific Pierce).

3.3. Image Processing and FRAP Fitting Methods

The following section is a description of the image processing and mathematical methodologies used to evaluate FRAP experimental data.

3.3.1. Image processing: Fluorescence calibration and cell reconstruction

In order to fit the recovery data with a mathematical binding model, specific cellular parameters such as fluorescent protein concentration (mobile and bound), rate of protein synthesis, extent of unintentional photobleaching, and cell morphology were evaluated from the FRAP data. A Matlab (The Math Works, Natick, MA) routine CellConstruct was used to extract these parameters. The input data includes *in vitro* GFP calibration images (Figure 3.1A), an image series of *E. coli* expressing GFP-fusion protein (Figure 3.1B), the experimental FRAP data series, and the confocal parameters listed in Table 3.3. Knowledge of the fluorescence excitation volume was required to convert the intensity acquired from bulk, *in vitro* wells of purified GFP into the equivalent intensity of GFP confined within a cell of bound volume of known dimensions (at constant Leica TCS SP2 settings). *In other words, one must answer the question, "What is the fluorescence intensity expected from a cell of known dimensions, relative to the intensity derived from a solution of infinite extent of the same concentration?"* In order to make this correction, a simulated, Gaussian laser probe was convoluted with a virtual cell

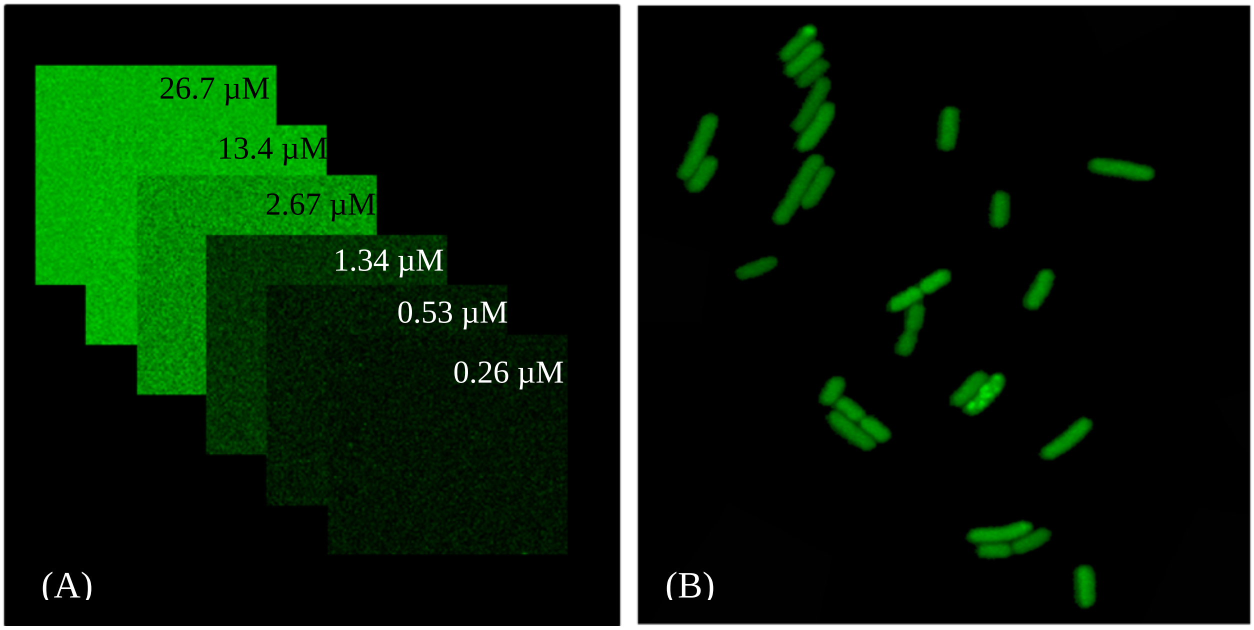

Figure 3.1 (A) *In vitro* GFP calibration images for correlating fluorescence intensity/concentration between known concentrations of “bulk” GFP and intracellular concentrations of GFP expressed in *E. coli*. (B) *E. coli* expressing GFP-Impα.

Table 3.3 Leica TCS SP2 settings that are required for CellConstruct input to scale *in vitro* fluorescence intensity to *in vivo* fluorescence intensity.

Laser wavelength	[nm]
Emission wavelength	[nm]
Objective numerical aperture	[0.1-1.6]
Objective magnification	[5-100]
Index of refraction	[>1]
Image resolution	[bits]
Image width	[pixels]
Photomultipiler tube voltage	[V]
AOTF laser intensity	[0-100]
Beam expander	[ ]
Voxel width	[nm]
Laser scan speed	[Hz]
Number of cells in fluorescence image	[ ]
Number of GFP calibration images	[ ]
Pinhole setting	[Airy]
Aperture diameter	[um]
***In vitro* GFP concentration**	[uM]

constructed from fluorescence images of real cells. The cell diameter, length, end cap shape and bound protein were determined from the experimental data by fitting procedures. The integrated fluorescence intensity of this model was compared with the *in vitro* GFP fluorescence intensity making sure to consider instrumentation and acquisition factors (where, due to the large bulk reservoir of GFP, the entire 3D beam distribution was assumed to excite fluorescence). A multiplication factor was derived to scale the intensity from the *in vitro* data to the *in vivo* data and depends directly on the integral of the probe excitation volume with each fluid spatial distribution. The *in vivo* protein concentration was then calculated from the fluorescence intensity data.

3.3.2 Image Processing: Fluorescence excitation assumptions

A Gaussian function was used to approximate the lateral laser probe profile where the beam waist (width) was reported as the e^{-1} intensity level and the calculated optical slice thickness was used to determine the depth of penetration of the beam. The optical slice thickness expression provided below represents the depth of information displayed at the pinhole and is valid for an Airy diameter of 1 AU and above.

$$z_{em} = \sqrt{\left(\frac{0.88\lambda_{ex}}{n^2-\sqrt{n^2-NA^2}}\right)^2 + \left(\frac{\sqrt{2}nd}{Mag3.6NA}\right)^2} \qquad \text{(Eq. 3.1)}$$

This equation represents the confocal behavior exhibited under the Geometrical–Optical Confocality regime and best describes the experiments described in this chapter. The efficiency of fluorescence excitation for molecules diffusing in a bounded volume (the cell) relative to those diffusing in an infinitely extending solution (baseline, *in vitro* wells) are considered equivalent.

3.3.3. Image Processing: Qualitative comparisons between the "virtual cell" and experimental data

A Gaussian probe image filter was generated based on the refined solution of the probe radius extracted from the experimental data. This filter was later used to convolute the final refined cell dimensions in order to generate an image of the computationally generated cell morphology as it would appear on the Leica confocal TCS SP2, to provide a qualitative, yet direct, comparison of the real cell with the simulated one (Figure 3.2).

3.3.4. Image processing: Calculation of bound protein at the cell poles

Integral to determining the number of fluorescent and bound molecules at the cell poles is an understanding of the irradiated surface area at the pole, per pixel, relative to the volume irradiated in the cell interior per pixel. A series of calculations was made to determine the number of molecules irradiated in each case utilizing the fluorescence intensity data collected at the cell interior center and at the midway point along the longitudinal axes of the cell poles. The number of molecules irradiated at the pole is proportional to the polar area that is irradiated and the number of molecules irradiated in the cell interior is proportional to the volume irradiated assuming a homogeneous coverage over the polar surface and a homogeneous spatial distribution of mobile protein within the cell interior. The surface area of the cell pole, irradiated by the laser probe, was calculated. The intensity per unit area of surface was then calculated, and when multiplied by the total polar area resulted in the total intensity from the polar region. This

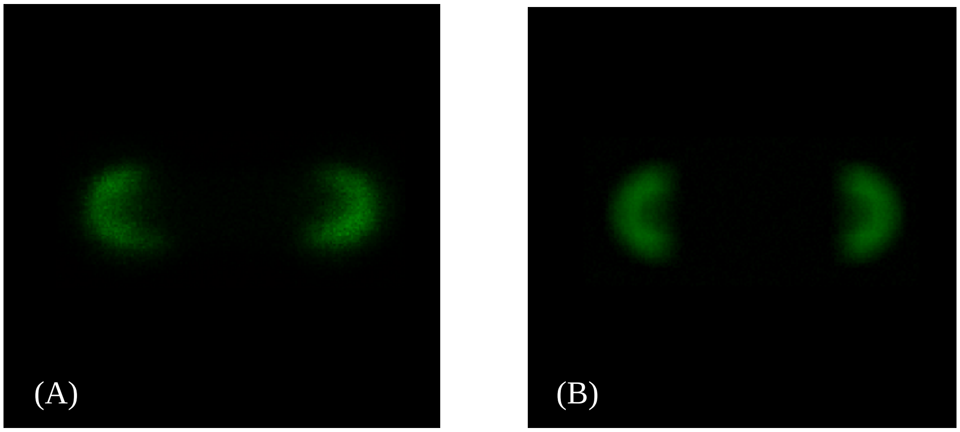

Figure 3.2 (A) *E. coli* cell, post-bleach, with bound protein at the cell poles. (B) 3D virtual cell derived from computational fits to the cell morphology as rendered on the Leica confocal TCS SP2 including noise, laser prove convolution, and image pixel size.

intensity was converted to the number of molecules bound as well as the concentration of bound protein if totally removed from the wall.

Subsequently, the number of molecules per unit area of pole surface was calculated as well as the total protein concentration in the cytosol volume. For example, if all the bound protein were dissolved into the cytosol along with the pre–existing mobile protein concentration; this last variable serves only as a additional means to comprehend the relative difference between the bound and mobile fractions; it has no other significance either for the simulation or as a meaningful variable but removes the surface area – to – volume conversion which can make comparing a bound surface density to volume concentration non–intuitive.

3.3.5. Image processing: Calculation of protein expression and low intensity photobleaching

The rate of photobleaching incurred during the course of the experiment as well as any detectable protein production must be identified and subtracted from the data to determine the true rate of fluorescence recovery in the cell interior (cytosol). Critical to this process was a reference cell that was located within the FRAP image series. The reference cell experienced the same fluorescence acquisition conditions as the photobleached cell minus the intentional photobleaching step. Thus, photobleaching during image acquisition and protein synthesis was assumed to be the same for both cells, which made it possible to directly correlate these processes accurately and precisely.

Photobleaching that occurred during fluorescence recovery acquisition (2% AOTF compared with 100% AOTF during photobleaching) induced a fluorescence decay in the reference cell with time on the order of 0.5–2% typically. This contribution to fluorescence recovery must be removed from the final recovery data. Photobleaching ensues as a function of the number of images acquired according to

$$I_{ref}^{ph}(p) = I_{ref}(1)(1-\gamma)^{p-1} \qquad \text{(Eq. 3.2)}$$

where p is the image number and γ is the photobleaching fraction per image acquisition and $I_{ref,p}$ is the photobleaching corrected, reference intensity. The reference cell intensity was fit to this function but only using images collected during a rapid time acquisition phase. Importantly, a succession of rapid image collection avoided convolution of protein production in these data points where the characteristic time representing protein production is much greater than the characteristic time for photobleaching

$$\tau_{protein} > \tau_{photobleach} \qquad \text{(Eq. 3.3)}$$

During the recovery phase, when the time between image acquisition increased significantly, the photobleaching rate remained constant and the protein production rate was derived from the reference cell intensity. The intensity decay during this regime is described by the expression

$$I_{ref}^{ph,pr}(p) = I_{ref}(1)(1-\gamma)^{p-1} + v(p-1) \qquad \text{(Eq. 3.4)}$$

where v is the protein expression rate over the time period $(p_n - p_{n-1})*\Delta t$. A least squares fit was performed to extract the protein expression rate from the reference cell data. The entire FRAP image stack was then corrected to remove both the photobleaching effect as well as the protein expression process from the data.

3.3.6. Image processing: Image drift correction

A measurable intensity shift arose from user generated error during refocusing prior to each image acquisition to maximize the intensity. In addition, the additional noise that was evident in the manually collected data, relative to the noise in the automatically collected data, represented an additional error induced during refocusing. A xy-drift correction alignment was applied to the Matlab routine.

3.3.7. FRAP Data Analysis: Fitting of experimental recovery curves to a binding model

A deviation least squares fit of the cell interior intensity recovery was performed according to the following expression based on 1st order chemical kinetics in order to determine k_{off} from the observed increase in fluorescence in the cell interior. The least squares fit is carried out using the following derived equation and chosen to call the "partially photobleached binding interaction model"

$$[F_m(t)] = \frac{F_T F}{F+B} + \left(F_{m,i} - \frac{F_T F}{F+B}\right) e^{-k_{off}\frac{F+B}{F}t} \quad \text{(Eq. 3.5)}$$

where F_m is the mobile, fluorescent protein intensity, F_T the total, fluorescent protein concentration, F the total, mobile protein concentration, B is the total, immobile protein concentration and $F_{m,i}$ is the initial mobile and fluorescent protein concentration. Data derived from these experiments were analyzed under the assumptions that the bound fraction of molecules were at equilibrium over the time course of the experiment, and that a non-dissociative Langmuir model dictates the binding interaction localized at the cell pole surfaces.

3.4. Results

3.4.1. Streptavidin and SBP

In an initial attempt to develop the quantitative assay, the well-described interaction pair streptavidin and streptavidin binding peptide (SBP) was cloned into the co-localization assay destination vectors. During the co-localization screen, a positive interaction was determined when streptavidin was anchored to the cell poles via its fusion to DivIVA and when SBP was expressed as an N-terminal GFP fusion. The SBP-GFP fusion protein was recruited to the poles as a result of its binding with streptavidin (Fig 3.3). Once a positive interaction was determined, fluorescence photobleaching and recovery experiment was conducted in an attempt to measure the binding affinity between the interacting proteins. The preliminary experimental design involved the complete photobleaching of GFP-SBP bound to streptavidin on one cell pole and recording the recovery in the same area (Fig 3.4 A, B). With this design, we found that in addition to the bound GFP-SBP bleaching, approximately 40% of the mobile fraction was bleached as well. Furthermore, fluorescence recovery simply by diffusion of the mobile fraction into the region of polar DivIVA and streptavidin binding occurred at such a fast rate that it was impossible to determine the amount of photobleaching in the defined ROI. An alternative experimental design was employed to address these issues.

The coupling of FRAP and its inverse technique (iFRAP) allowed us to turn the rapid diffusion of GFP-SBP into an advantage. Using this approach, an ROI was defined in the center of the cell to bleach all of the mobile GFP-SBP molecules. As GFP-SBP rapidly diffuses, the total bleach pulse time (Table 3.1) ensured the complete bleaching of all mobile GFP-SBP. This bleaching event was seen at 2 seconds after the start of the experiment (Figure 3.4D).

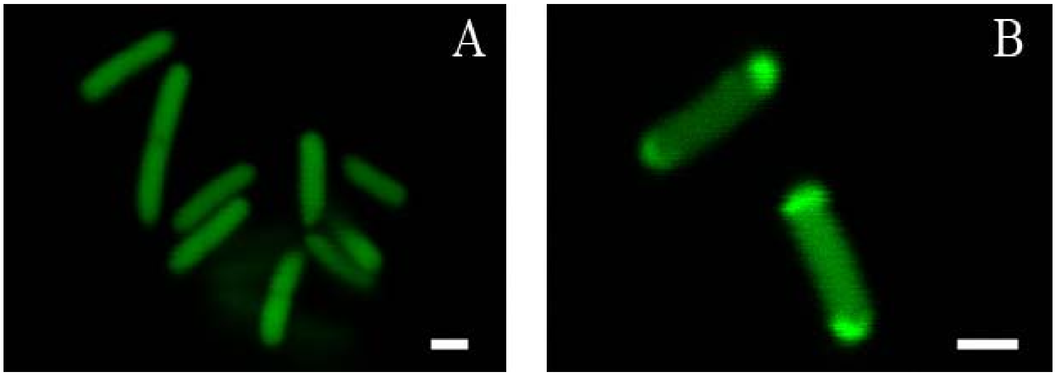

Figure 3.3 Detection of a positive interaction between DivIVA-Streptavidin and GFP-SBP. Images of cells showing localization of GFP-SBP before (A) and after (B) induction of DivIVA-Streptavidin expression.

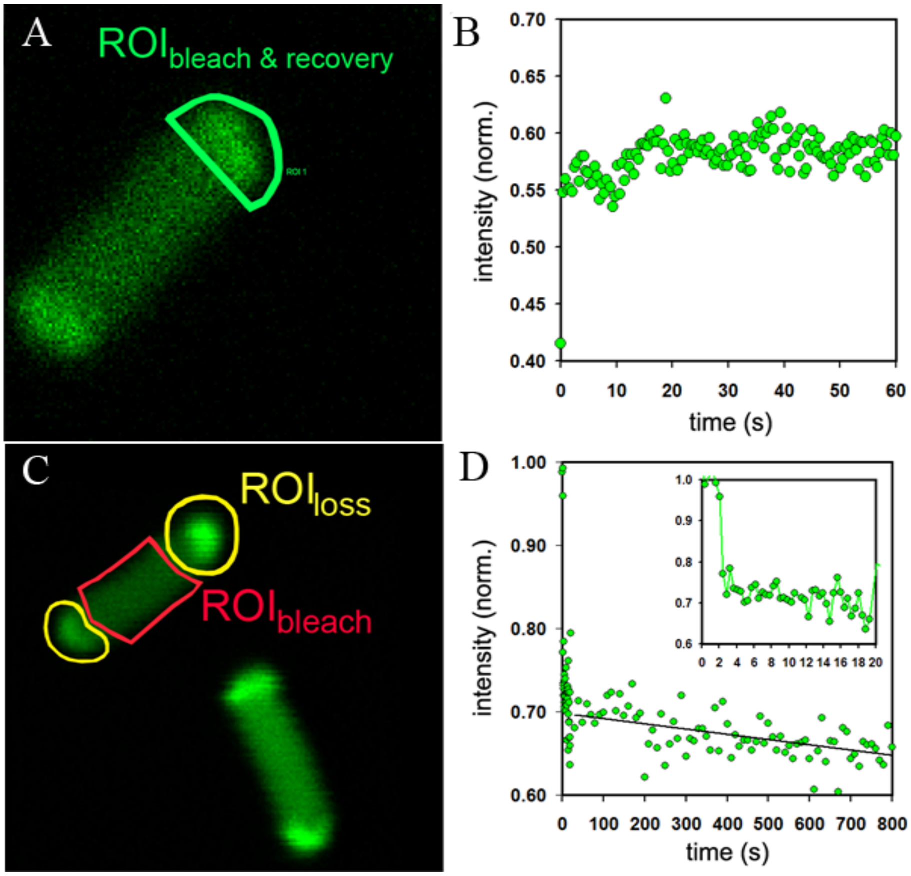

Figure 3.4 (A) Fluorescence image of GFP-SBP localized to the poles of *E. coli*. A semi-circular ROI was used to bleach the pole. (B) The resulting recovery curve after bleaching the localized GFP-SBP at the cell pole. (C) Live cell fluorescence image of GFP-SBP localized to the poles where the ROI defined in red is where the bleach pulse is applied. Fluorescence loss is monitored at the poles (D) Fluorescence loss curve following the photobleaching of mobile GFP-SBP indicating exchange between bound fluorescent GFP-SBP and mobile bleached GFP-SBP.

Fluorescence loss was monitored at the poles of the cells as bleached mobile GFP-SBP exchanged for bound GFP-SBP. Further, the fluorescence recovery was monitored in the center ROI ($\mathrm{ROI}_{\mathrm{bleach}}$) as the exchange occurred (Fig 3.4C). Again, a reference cell located in the same field of view served as a control for fluorescence loss due to image acquisition. Figure 3.4D shows the fluorescence loss curve acquired from one cell pole after photobleaching. The slow loss in fluorescence is indicative of the tight binding of streptavidin and SBP (K_d = 2.5 nM) [195]. This experimental design demonstrated that the binding events were measurable.

While the FRAP/iFRAP methodology proved to be effective in measuring binding, careful optimtimization of the image acquisition parameters were necessarity with this methodology in order to record a signal. The laser power for post-bleach imaging was a significant parameter that limited the recordable fluorescence recovery. It was essential to find a compromise between recording a fluorescence signal and unintential photobleaching while imaging was essential. Experiments failed when the rate of photobleaching exceeded the rate of binding exchange (Figure 3.5). As a result the ATOF setting was reduced to the minimal amount (2-2.5%) while a fluorescence signal was still detectible. In addition, the time interval between post-bleach images was increased to reduce the exposure of the FRAP and reference cells to the image laser.

3.4.2. Impα and NLS stability in vivo

Although the streptavidin and SBP interaction pair was used in the initial development of this assay, the Impα and NLS variants proved to be more valuable as a model system. As described in Chapter 2, Impα-NLS interactions offer a wide range of binding affinities from which to compare the biophysical data acquired from FRAP experiments (Table 2.3).

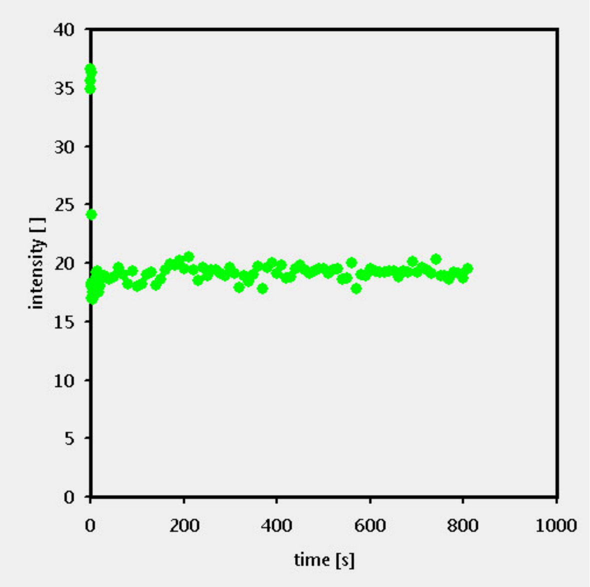

Figure 3.5 A FRAP experiment of Streptavidin and SBP interaction without measurable recovery. This occurred when the rate of background photobleaching exceeded the rate of protein exchange at the cell poles. Any mobile fluorophore contributing to recovery was unintentionally photobleached during image acquisition. In order to optimize imaging during recovery, the ATOF was set to optimize contact between the fluorescence at the cell poles and the recovery ROI, and to minimize unintentional background bleaching.

To substantiate the use of Impα and NLS peptides as an ideal model system for assay development, the molecular stability of the fusion proteins *in vivo* was a necessary parameter to address. Western blots were conducted to determine if the GFP-Impα fusion protein was cleaved *in vivo*. In Figure 3.6 both the insoluble and soluble fraction of GFP-Impα was analyzed. A visible band in all lanes immediately under the 75 kDa marker corresponds to the 73 kDa protein fusion, indicating that the protein is not cleaved at the linker site and remains intact *in vivo* and while extracted. However, once extracted from the cell, the solubility of the protein decreases and a more intense band is visible for the insoluble fraction verses the soluble fraction.

3.4.3. GFP-Impα protein concentration

In order to fit the experimental FRAP recovery data with a binding interaction model, several parameters must be determined. The model derived for this system requires knowledge of the *in vivo* concentration of GFP- Impα. This was achieved by correlating fluorescence intensity from known concentrations of purified GFP to the fluorescence intensity of GFP-Impα expressed in *E. coli*, where the methodology is described above. The protein concentration of GFP-Impα expressed in *E. coli* was measured using an ELISA based technique. These data were to serve as a comparison for measurement of protein concentration *in vivo* using fluorescence intensity. The protein concentration measured *in vivo* for cells expressing GFP-Impα was determined for each experiment and fell within the range of 50-100 µM. The protein concentration for GFP-Impα measured with ELISA *in vitro* was 0.37 ± 0.04 µM.

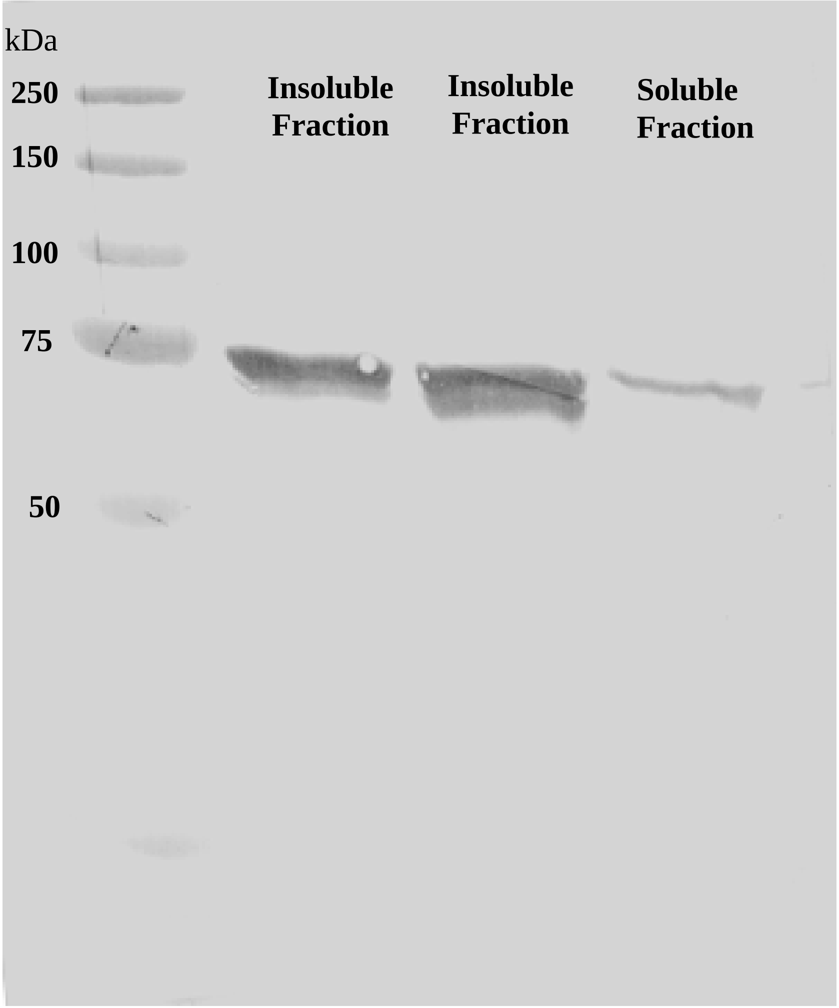

Figure 3.6 Western blot of GFP-Impα. The first two lanes were loaded with the insoluble fraction of the cell lysate and the third lane is loaded with the soluble fraction. The molecular weight of GFP-Impα is 73 kDa. It is apparent that the fusion between the proteins remained intact while expressed in *E. coli*.

3.4.4. FRAP analysis: Impα and Nuclear Localization Signals (NLSs)

Several interaction pairs were used to perform FRAP experiments (Table 3.5). In addition, we optimized the imaging parameters on the Leica confocal microscope to minimize background bleaching during image acquisition, while leaving the fluorescence field of view bright enough to detect fluorescence recovery in the center ROI. Table 3.2 describes the parameter settings that were designated in the FRAP application for each experiment. These parameters remained constant for all subsequent experiments. In addition, we noticed that the automatic acquisition of images post-bleach was unacceptable due to unintentional z-focal plane drift of the sample. Therefore, images were manually acquired at designated time intervals post-bleach for the duration of the experiment. The data output for an experiment is described in Table 3.4.

FRAP experiments were conducted for interactions between Impα and SV40 (wild type), SV40A7E, SV40A4, SV40T3. Impα was expressed as an N-terminal fusion and the NLS variants were expressed as DivIVA N-terminal fusions. Figure 3.7 shows the interaction between Impα and SV40A4. The mobile GFP-Impα is clearly visible in the pre-bleach images (Figure 3.7 A, B). A bleach laser was applied to ROI 2 for photobleaching of the mobile fluorophore. The bleach pulse applied to the ROI was of sufficient power to bleach all of the moble fluorescent protein by at least 50% (Figure 3.7 C, E). After the experiment, a qualitative analysis of the pre-bleach and post-bleach fluorescence intensity values was performed to quickly assess the experimental data (ie to qualitatively determine the extent of photobleaching and fluorescence recovery). After an experiment was complete, the CellConstruct routine was used to process and refine the FRAP image series to acquire protein concentration values,

Table 3.4: Data output after processing a FRAP image series with the CellConstruct routine.

Mobile protein concentration (GFP+Impα)	66.6	[uM]
Cell diameter	0.78	[um]
Cell length	2.22	[um]
Laser probe radius	0.168	[um]
Immobile protein surface density	0.003	[molecules nm^2]
Total protein concentration (GFP+Impα)	83.4	[uM]
Mobile + fluorescent protein after photobleach	-0.2	[uM]

Table 3.5: Quantification of Impα-NLS binding

Protein Fusion	K_d (nM)[*]	K_d (nM)[†] *in vitro*	k_{off}[‡] [s^{-1}] *in vitro*	k_{off} [s^{-1}][**] *in vivo*
SV40 (wt)	9 ± 4	52 ± 1	0.00007 ± 0.00003	ND
SV40A7E	283 ± 80	240 ± 3	0.00004 ± 0.00001	0.0004 ± 0.00015
SV40A4	335 ± 7	303 ± 3	0.00004 ± 0.00003	0.0002 ± 0.00017
SV40T3	3000 ± 1414	4352 ± 51	0.0001 ± 0.00002	0.0008 ± 0.00001

[*] Binding affinity determined by fluorescence anisotropy experiments described in [78].
[†] Binding affinity acquired in this study by fluorescence anisotropy.
[‡] k_{off} acquired in this study by fluorescence anisotropy.
[**] Calculated from best weighted non–linear, least squares fit to fluorescence recovery curve.

binding site density, and cell morphology information required to fit the photobleach model. Table 3.5 shows the output data for GFP-Impα and DivIVA-SV40A4 FRAP cell in Figure 3.7. The cytosol fluorescence intensity recovery was plotted as a function of time and a best weighted non–linear, least squares fit was applied to the fluorescence recovery curve (Figure 3.8). Again, slow recovery of fluorescence is indicative of the tight binding between Impα and SV40A4 (K_d = 335 nM), and is completely uncoupled from the high rate of molecular diffusion in the *E. coli* cytosol. Table 3.5 shows *in vivo* k_{off} data for SV40A7E, SV40A4, and SV40T3 derived from FRAP data. The SV40 wild type NLS has yet to be determined due to high rate of protein synthesis. In turn, this prevented the CellConstruct routine from efficiently processing the recovery data. Further optimization of the experimental routine is required for this data set.

3.4.5. Impα and NLS fluorescence anisotropy

Disassociation constants are readily available in the literature for Impα/NLS interactions (Table 2.3, [75-78]). However, there is the possibility that protein fusions used in this assay may have different disassociation constants or rates of association/disassociation. Fluorescence anisotropy was applied to measure the disassociation constants and the k_{off} rates of the interaction pairs analyzed by FRAP. Typical fluorescence anisotropy curves for SV40 and three NLS variants are presented in Figure 3.9. The anisotropy values are plotted as a function of Impα concentration. The *in vitro* binding data show similar results to the values reported previously (Table 3.5). In addition, we measured the k_{off} rates for each of the NLS peptides in order to compare the k_{off} rates determined by FRAP. The k_{off} rates between the *in vitro* and *in vivo* data differed by an order of magnitude. However, a trend between both data sets is apparent. The rate of disassociation increases as the binding affinity, defined by K_D, decreases (Table 3.5).

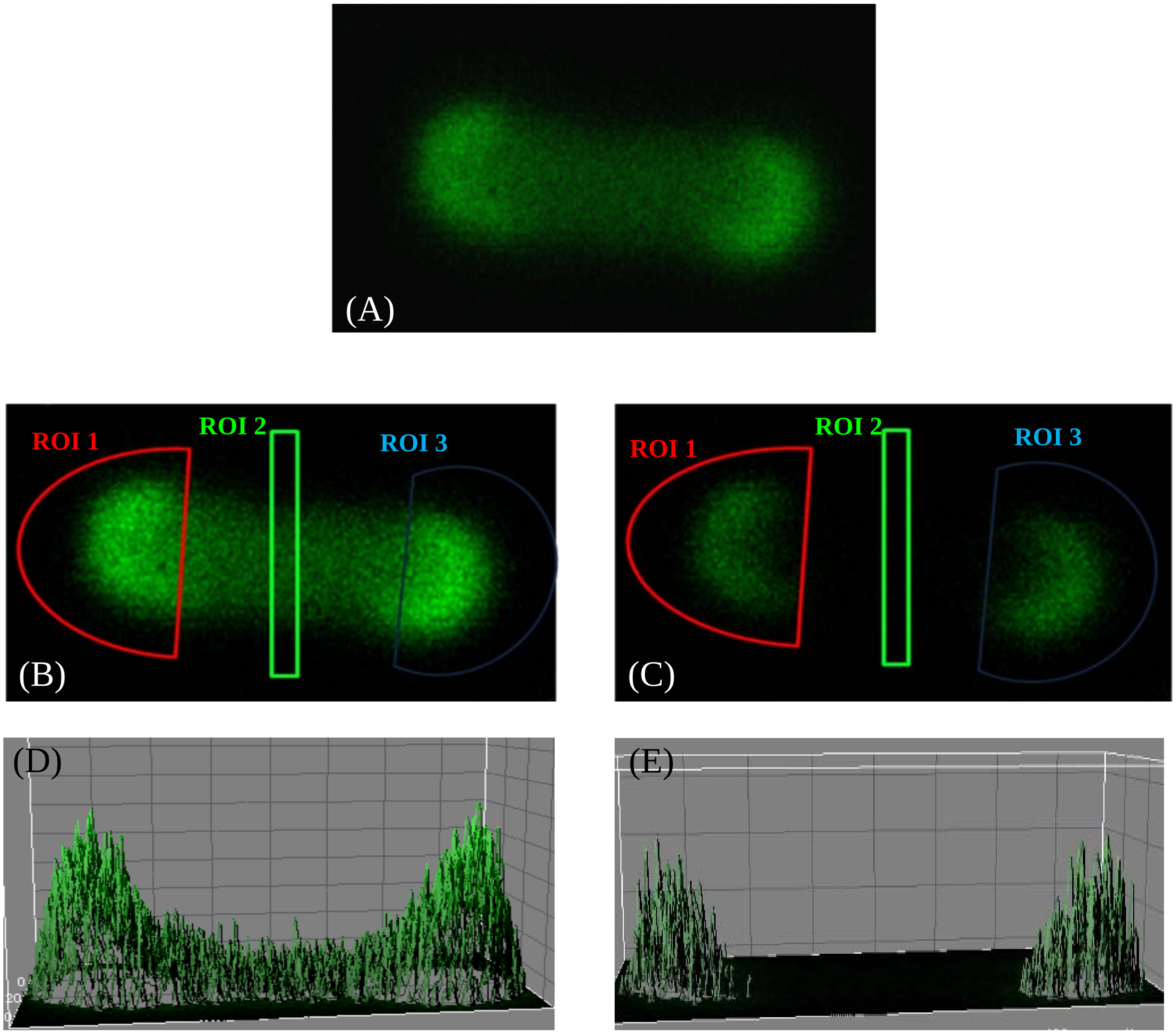

Figure 3.7 A FRAP experiment for the interaction between GFP-Impα and DivIVA-SV40A4. (A) The interacting proteins localized to the cell pole. (B) Pre-bleach image with appropriate confocal image settings required for FRAP experiment to commence. *t* = 0.0 sec pre-bleach, the bleach laser was set for 100% at ROI 2. (C) After photobleaching (*t* = 8.0 sec post-bleach), fluorescence recovery was plotted from ROI 2 fluorescence intensity data. ROI 1 and ROI 3 were arbitrary and used for a qualitative look at fluorescence loss at the cell poles after the experiment is complete. They are not required for data analysis of the recovery curve. Fluorescence intensity measured pre-bleach (D) and post-bleach (E).

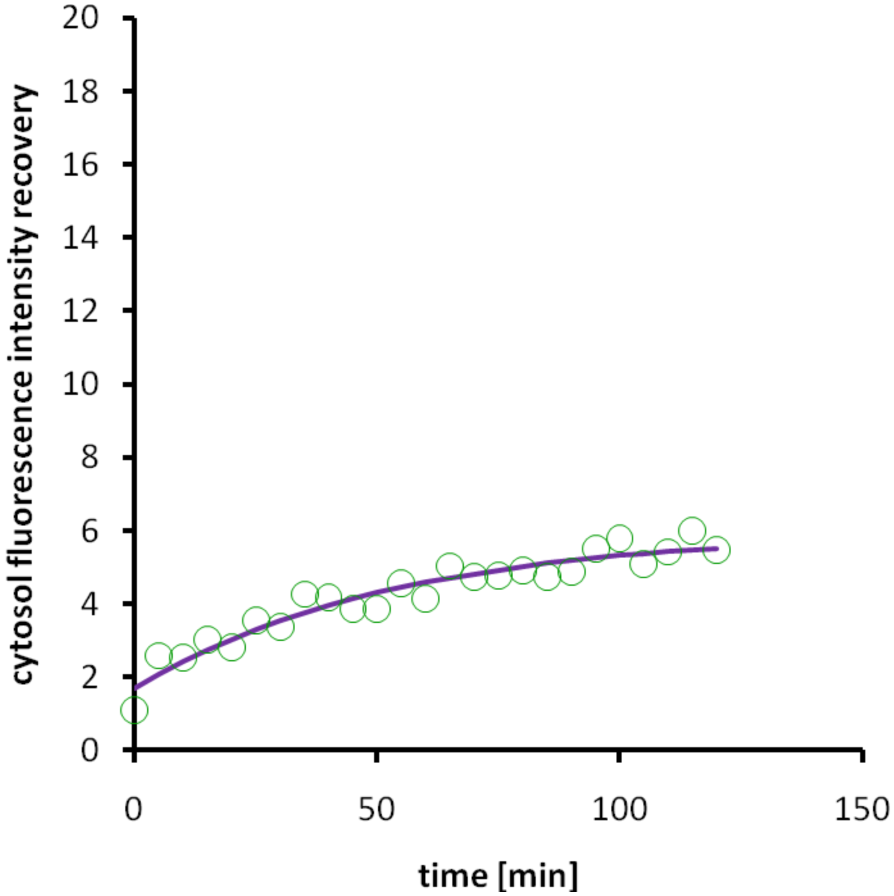

Figure 3.8 FRAP recovery curve for GFP-Impα and SV40A4 interaction fit with the partially photobleached binding interaction model.

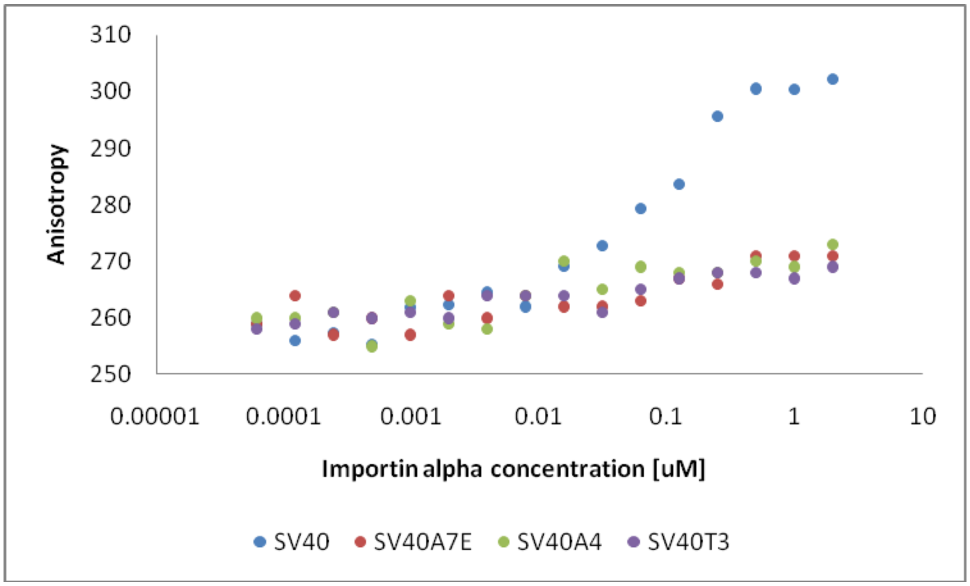

Figure 3.9 Florescence anisotropy plot for SV40 wild type, SV40A7E, SV40A4, SV40T3.

3.5. Discussion

In Chapter 2, we successfully modified and characterized a fluorescence based co-localization assay, which provided rapid identification of PPIs *in vivo*. In this study, we report a general, facile method to identify and quantify PPIs. Due to the unique spatio-temporal separation/localization of the fluorescence pattern resulting from a positive protein interactin, we applied a fluorescence recovery after photobleaching (FRAP) methodology to characterize the rate of disassociation (k_{off}) for the interacting proteins of interest. Typically, kinetics studies *in vivo* have focused on characterizing highly specific cellular processes. Here, we present the first generalized *in vivo* quantitative PPI screen that is applicable for prokaryotic and eukaryotic soluble proteins.

Taking advantage of the known interaction characteristics of streptavidin and streptavidin binding peptide (SBP), we sought to develop an efficient FRAP methodology and computationally interpret the recovery based on a derived mathematical model. To proceed with this task, it was first necessary to optimize the FRAP application and confocal parameters. Although the initial method was simple in principle and execution, it did not yield the correct image contrast and separation between binding events necessary for data interpretation. When defining the ROI strictly at the cell pole, the fluorescence recovery in this specific region should represent the exchange of the mobile GFP-SBP with the bound fraction at the DivIVA-streptavidin binding sites. However, upon plotting the initial recovery curves, difficulties arose with the original experimental design. A significant fraction of the mobile GFP-SBP was bleached as a result of rapid diffusion of GFP-SBP during the bleach time. In this case, potentially a bleached mobile GFP-SBP could be exchanged for a bleached bound GFP-SBP at the cell pole, thus introducing error in the recovery curve. In turn, this circumstance could lead to overestimation of the binding affinity. Therefore, a derivative FRAP technique (inverse FRAP) was used to measure recovery in a region adjacent to binding and proved to be more effective in measuring recovery. A rectangular ROI, centered perpendicular to the cell axis, was used to bleach all of the mobile fluorescent protein without any unintentional beaching of the bound fluorescent fraction at the cell poles. Using this technique, fluorescence recovery was measurable in the center ROI.

Although streptavidin and SBP proved valuable in the initial experimental design, this pair offered some disadvantages to refining our techniques for determining binding affinities. For example, the streptavidin binding system only offers a small range of interacting peptides with a limited range of binding affinities to test. Furthermore, biotin found in *E. coli* can compete with SBP for the binding to streptavidin at the poles, which may introduce unnecessary error. In Chapter 2, we used Impα to measure the sensitivity of the co-localization assay. Here, we turned again to Impα as a model system for developing and evaluating the performance of our quantitative techniques.

In addition to optimizing the necessary experimental parameters, computational methods were developed and refined simultaneously with assay development. In order to meet the required parameters for analysis and interpretation of a FRAP recovery curves, a MatLab routine was developed to extract quantative information for protein concentration, cell morphology, and beaching parameters. A significant development was the calculation of fluorescent protein concentration, by implementing a calibration procedure of the confocal at known settings and correlating the relationship between known *in vitro* concentrations of GFP with *E. coli* cells expressing GFP-fusion protein. Without the concentration of intracellular GFP, only relative measurements of kinetics could be obtained. According to the University of Alberta *E. coli* CyberCell statistical database [196] total protein concentrations in *E. coli* vary between 5-8 mM. Therefore, the protein concentration *in vivo* should be some fraction of this value. Indeed, the *in vivo* concentrations determined for GFP-Impα were between 50-100 µM, accounting for approximately 1% of the total proteome. Since quantifying protein concentrations in live cells using fluorescence microscopy is not a standard method, we sought to evaluate the validity of our method by comparing the protein concentrations acquired *in vivo* with an ELISA-based *in vitro* quantitation method. We found that the GFP-Impα concentration determined *in vitro* was on average two orders of magnitude lower than the measured GFP-Impα *in vivo*. This difference is not surprising since the ELISA only measured the soluble protein concentration. Western blots revealed that although the protein fusion is stable *in vivo*, it is partially insoluble when extracted from the cells. Insolubility and insufficient lysis efficiency may explain the discrepancy between the two data sets.

Finally, we utilized the optimized FRAP and computational methods to measure the dissociation of Impα with SV40 wild type and three NLS variants. The three NLS variants measured have significantly weaker affinity for Impα, and fluorescence recovery was measurable over the course of 1-2 hours. After processing the data and fitting the binding model, we determined the k_{off} rates for each variant. We predicted longer interaction times as K_D decreased. In fact, the rate of disassembly *in vivo* for the SV40T3 variant (highest K_d value at 3000nM corresponding to the weakest affinity for Impα) was 8×10^{-4} s^{-1}. SV40A4 and SV40A7E have similar disassociation constants and were predicted to have similar rates of disassociation. *In* *vivo* measurements were similar for both variants, where k_{off} for SV40A4 (335 nM) was 2 x 10^{-4} s^{-1} and k_{off} for SV40A7E (283 nM) was 4 x 10^{-4} s^{-1}. These rates of disassociation were significantly slower than the SV40T3 variant. This trend is in agreement with the *in vitro* rate of disassociation measured by fluorescence anisotropy although the values are off by an order of magnitude. It is interesting that the disassociation kinetics for these NLS peptides *in vivo* occurs at a faster rate compared to the disassociation *in vitro,* while the trend between the NLS variants remains. This raises questions to the physiological significance of this result and prompts further investigation. It is quite possible that the discrepancies in k_{off} values are due to differences in environmental effects. The intracellular milieu of *E. coli* is significantly more complex than the HEPES buffer used to measure disassociation *in vitro.* Additional FRAP experiments for other NLS variants are underway to establish if this trend holds true. Whether this result is significant for only the Impα/NLS system or appears in other PPI systems remains to be determined.

The disassociation kinetics for SV40 wild-type NLS have proved to be challenging in that the rate of fluorescence recovery is significantly slower than the rate of protein synthesis. We are currently looking into methods to reduce the rate of protein synthesis and increasing the contrast between the bound and unbound fraction of fluorescent protein post-bleach over the course of 3 hours. Simple approaches, such as reducing the environmental temperature around the cells during image acquisition or applying a low dose antibiotic, such as gentamycin or tetracycline, can be employed to reduce the rate of protein synthesis, thereby facilitating a greater likelihood of measuring fluorescence recovery. On the other hand, SV40 has a disassociation constant of 9 nM, which is classified as a strong, perminant interaction. The physiological significance of measuring the kinetics of such a strong interaction may not be necessary. In fact, this methodology is perhaps more applicable to weaker, transient interactions. Characterizing the kinetics of interactions between proteins involved in transient events such as signal transduction is more physiologically significant since the rate of binding is directly related to the functional transfer of a signal within a cell.

This study proves that FRAP coupled with co-localization is an efficient, quantitative method to detect PPIs. In the future, additional simulations could be extended to derive association kinetics, along with binding constants. Thus, the experimental methodology described here presents an opportunity to facilitate quantification of PPIs in any number of biological systems.

Chapter 4. Extracellular interactions: Characterization of *Azospirillum* Che1 mutants by AFM

This chapter is based on a manuscript reprinted from *FEMS Microbiology Letters*, 314 /2, A. Edwards, A. N., Siuti, P., Bible, A. N., Alexandre, G., Retterer, S. T., Doktycz, M. J. and Morrell-Falvey, J. L., "Characterization of cell surface and extracellular matrix remodeling of *Azospirillum brasilense* chemotaxis-like 1 signal transduction pathway mutants by atomic force microscopy." 131-139, Copyright (2011), with permission from John Wiley and Sons.

Data, images, and text relevant to this study are included in this chapter. Images are presented in color where they were published in black and white. Under the direction of the co-authors, I conducted the experiments, analyzed the resulting data, and drafted the manuscript. The co-authors responded with editorial comments and additional text where needed.

4.1 Introduction and Significance

Azospirillum brasilense are soil diazotrophic bacteria that colonize the roots of many economically important grass and cereal species [151]. Under conditions of high aeration and limiting availability of combined nitrogen, *A. brasilense* cells differentiate into aggregating cells and form dense flocs that are visible to the naked eye [160, 162]. Flocs are formed by cell-to-cell aggregation between non-motile cells embedded in a dense extracellular matrix [161]. Flocculation correlates with, and likely requires the production of, arabinose-rich extracellular polysaccharides (EPS) [164]. Scanning electron and fluorescence microscopy studies of *A. brasilense* aggregating cells indicates the presence of fibrillar material connecting cells to each other or to biotic or abiotic substrates [165, 166]. These fibrils seem to be absent in non-aggregating cells or mutants strains that are defective in aggregation, suggesting they may play a role in promoting this behavior [160, 167]. The detailed biochemical composition of this fibrillar material remains unknown, although it is possible that it is related to EPS production [164]. In support of this idea, the degree of bacterial aggregation appears to correlate with the amount and composition of EPS produced by several *A. brasilense* strains [160].

Chemotaxis is perhaps the most studied signal transduction pathway in bacteria (reviewed in [197-200]). Despite identification of homologous chemotaxis systems in phylogenetically distant bacteria and archaeal species, there is a great diversity in both the number of chemotaxis operons encoded within bacterial genomes and their physiological roles [200]. Recent studies have shown that the functions of chemotaxis-like pathways are not limited to regulation of motility patterns, but also include the regulation of biofilm formation, EPS production, and cell-to-cell interactions [201-204]. In prototypical chemotaxis, the histidine kinase CheA and the response regulator CheY form a two-component signal transduction system, which ultimately modulate the probability of changes in the direction of rotation of flagellar motors in response to specific environmental cues. Changes in the phosphorylation of CheY regulated by the CheA-CheY phosphorylation cascade modulate the affinity of CheY for the flagellar motor switch complex and thus chemotaxis. Surprisingly, in *A. brasilense,* strains carrying mutations in components of the Che1 chemotaxis-like pathway were found to be affected in their ability to interact by cell-to-cell aggregation and in flocculation. Mutant strains lacking functional CheA1 or CheY1 aggregate and flocculate significantly more than the wild type strain, suggesting that Che1 modulates the ability of *A. brasilense* cells to flocculate. However, the exact mechanism by which the Che1 pathway regulates cellular functions other than chemotaxis is not known [205]. Initial attempts at identifying extracellular structures produced specifically by the mutant strains lacking CheA1 and CheY1 and thus controlled by the activity of Che1 have failed, but an effect of Che1 on EPS production was suggested from differences in Congo Red staining of colonies [205]. Flocculation in *A. brasilense* has been previously correlated with changes in the structure and/or composition of the extracellular matrix (reviewed in [161]) and thus the current working hypothesis is that the Che1 pathway affects flocculation by modulating changes in the structure and/or composition of the extracellular matrix [205].

In this study, we tested this hypothesis by applying AFM techniques to investigate the cell surfaces of wild-type *A. brasilense* and its Che1 mutant strain derivatives (AB101 (Δ*cheA1*) and AB102 (Δ*cheY1*)). AFM was selected because it allows nanoscale resolution of biological materials without prior sample fixation. Resolution limitations associated with optical imaging methods and the fixation and dehydration procedures typically associated with classical EM techniques can inhibit visualization of extracellular structures and could have prevented identification of CheA1- or CheY1-specific extracellular structures produced during flocculation [205-207]. The data obtained using AFM conclusively identifies a distinctive remodeling of the extracellular matrix, likely via changes in EPS production, in AB101 (Δ*cheA1)* and AB102 (Δ*cheY1*) under flocculation conditions as well as remarkable differences in the structural organization of the aggregates formed by each of these two strains. Further analyses using a lectin-binding assay, flocculation inhibition, and comparison of LPS profiles are consistent with the hypothesis that the Che1 pathway modulates changes in the extracellular matrix that coincide with flocculation, although this effect is likely to be indirect because our data reveal distinct changes in the content or organization of the extracellular matrix of the Δ*cheA1* and Δ*cheY1* mutant strains.

4.2. Materials and Methods

4.2.1. Strains and growth conditions

Azospirillum brasilense wild type parental strain Sp7 (ATCC 29145) and mutant strains defective in CheA1 (strain AB101 (Δ*cheA1*)) and CheY1 (strain AB102 (Δ*cheY1*)) from the Che1 pathway were used in this study [205, 208]. Wild type and mutant strains were grown in nutrient TY (Tryptone-Yeast Extract) and a minimal salt medium (MMAB) [209]. To induce flocculation, cultures were first grown in nutrient TY (Tryptone-Yeast Extract) liquid medium overnight and normalized to an optical density (OD_{600}) of 1. Then, 250 µl of this culture was used to inoculate 5 ml of liquid MMAB with 20 mM malate or MMAB with 20 mM malate and 0.5 mM $NaNO_3$. Cultures were incubated at 28°C in 20 ml glass culture tubes with agitation on a platform shaker.

4.2.2. Quantification of flocculation

Absorbance readings (OD_{600}) were acquired for each growth condition to determine the amount of planktonic culture. Care was taken to ensure that the flocs had settled to the bottom of the tube before measurements were taken. To quantify the amount of flocculation, we modified a protocol described previously [160, 210]. Briefly, 1 ml of sample was subjected to mild sonication using a Branson Digital Sonifer Model 102C equipped with a 3.2 mm tapered micro tip. Settings for sonication included sonic pulses of 2 seconds on and 2 seconds off with the amplitude set at 10%. OD_{600} absorbance measurements were acquired immediately after sonication. The percentage of flocculation was calculated by the $(OD_a\text{-}OD_b/OD_a) \times 100$ where OD_a = optical density after sonication and OD_b = optical density before sonication. Optical microscopy was used to confirm disruption of the flocs and to verify that sonication did not lead to cell lysis.

4.2.3. AFM sample preparation

AFM samples were prepared as described previously, with slight modifications [211]. Briefly, 1 ml aliquots of bacteria grown in the conditions described above were harvested by centrifugation (8000 rpm) after 24 hours and 1 week of growth. The cells were resuspended in 100 ul of dH_2O and the cell suspension was added to a freshly cleaved mica surface. The samples were allowed to air dry 8-24 hours before imaging.

4.2.4. AFM image acquisition

Samples were imaged with a PicoPlus atomic force microscope (Agilent Technologies, Tempe, AZ) with a 100 µm multi-purpose large scanner. The instrument was operated in contact mode at 512 pixels per line scan with speeds ranging from 0.5 to 1.0 Hz. A Veeco MLCT-E cantilever with a nominal spring constant of 0.5 N/m and a resonant frequency ranging from 26-50 kHz was used for imaging. For all samples, first order flattened topography and deflection scans were acquired with sizes ranging from 1.5 to 75 µm.

4.2.5. Scanning electron microscopy (SEM) image acquisition

SEM samples were prepared in the same manner as described above for AFM samples. A Hitachi TM 1000 instrument was used for SEM imaging. Unlike conventional SEMs, standard fixative processes were not necessary for biological samples. Images were acquired with a magnification range of 20 to 10,000x with a resolution of 640 x 480 pixels. An accelerating voltage of 15 kV was applied in charge-up reduction observation mode at room temperature.

4.2.6. Lectin binding assay

Wild type and mutant strains were grown in 5 ml cultures as described above to induce flocculation. After 24 hrs, the cells were harvested, washed in PBS, and resuspended in 200 µl of PBS. FITC conjugated lentil (LcH; Sigma #L9262) and lima bean lectins (LBL; Sigma #L0264) were diluted to 5 mg/ml in PBS and 2 µl was added to the cell suspension to give a final concentration of 50 µg/ml. The mixture was then incubated at room temperature with shaking for 20 min. Cells were harvested at 8,000 rpm and washed with PBS before imaging with a Leica TCS SP2 scanning confocal microscope equipped with a Leica HCX PL APO 63x/1.40-0.60 oil objective lens. Leica LCS software (version 1537) was used for image acquisition. ImageJ was used to assess fluorescence intensity for each image by converting to a binary image and setting a consistent threshold level.

4.2.7. Flocculation inhibition assay

An aggregation bioassay previously described by Burdman et al [212, 213] was used with slight modifications to assess the roles of D-glucose and L-arabinose on flocculation. Briefly, wild type, AB101 (Δ*cheA1*), and AB102 (*ΔcheY1*) strains were grown in low C:N conditions (non-flocculating medium supplemented with 20 mM malate and 18 mM NH_4Cl) or in the high C:N ratio minimal medium which induces flocculation described above. After 24 hours, the culture of flocculating cells grown in high C:N ratio medium was sonicated for 20 s and then centrifuged at 13000 rpm for 2 min. The resulting supernatant was then added to cells grown under non-flocculating (low C:N) conditions along with 0.05, 0.1 or 0.5 M concentrations of D-glucose or L-arabinose. The cultures were incubated at 28˚C with shaking for 3-4 hours. Flocculation was quantified using the protocol described above.

4.2.8. Extraction of lipopolysaccharides

Lipopolysaccharides were extracted from all strains grown in TY and flocculation medium at 24 h and 1 week using an lipopolysaccharides extraction Kit (Intron Biotechnology)following the manufacturer's instructions. Equal aliquots of lipopolysaccharides extract were dissolved in sodium dodecyl sulfate (SDS) sample buffer, boiled for 5 min, and loaded onto a 4–20% Tris-HCl SDS-polyacrylamide gel electrophoresis gel (Bio-Rad). Samples were electrophoresed at 150 V for 1 h. Gels were silver stained as described (Kittelberger & Hilbink, 1993).

4.3. Results

4.3.1. Flocculation

Consistent with previous work, we observed differences in the flocculation behavior of *A. brasilense* mutant strains deficient in CheA1 and CheY1 compared to wild type cells grown under conditions of nutrient and aeration stress in malate containing medium. Differences in the flocculation phenotype were observed and quantified at 24 hr and 1 week after inoculation (Table 4.1). At the 24 hr time point, aggregative structures were clearly visible for AB101 (Δ*cheA1)* and AB102 (Δ*cheY1*). These small macroscopic aggregates could be detected as early as 8 hrs after inoculation. The small flocs appeared as macroscopic flakes of cell material dispersed throughout the medium or settled at the bottom of the tube. The amount of flocculation relative to planktonic cells was increased after 1 week of incubation under these conditions (Table 4.1). Unlike the mutant strains, the wild type strain did not exhibit any significant flocculation behavior at the 24 hr time point. The wild type strain did, however, have

Table 4.1: Quantification of flocculation.

Strain	**Percent aggregation 24 hours**	**Percent aggregation 1 week**
Wild type Sp7	0.01 ± 0.67	32.3 ± 9.50
AB101 (Δ*cheA1*)	52.0 ± 0.07	95.0 ± 0.61
AB102 (Δ*cheY1*)	86.3 ± 0.02	93.5 ± 0.38

a significant flocculation phenotype after 1 week of incubation, which is consistent with previous work [205] (Table 4.1).

4.3.2. Comparison of wild type and Che1 mutant cells by AFM and SEM imaging

Since the mutant strains displayed a premature flocculation phenotype compared to wild type cells, AFM and SEM methods were used to characterize planktonic wild type cells and flocculating AB101 (Δ*cheA1)* and AB102 (Δ*cheY1*) cells at 24 hrs (Figure 4.1 A-I). To maintain the physical structure of the extracellular matrix, chemical fixation procedures were not used. Rather, the cells were air-dried at room temperature on a mica substrate for AFM and SEM imaging. During the immobilization procedure, we observed that the wild type cells remained motile on the mica substrate as the liquid receded during preparation, whereas the mutant cells did not appear to move. The motility of the wild type strain may explain why all the cells are seen oriented side-by-side as a monolayer after 8-24 hrs of drying (Figure 4.1 A-C). A cross-section measurement from the topographic image of wild type cells indicates a uniform monolayer of cells approximately 500-700 nm in height (Figure 4.2 D, E). In contrast, AFM and SEM analyses revealed a different pattern of cell organization on the surface of the mica substrate for the mutant strains (Figure 4.1 D-I). Strains AB101 (Δ*cheA1)* and AB102 (Δ*cheY1*) aggregated and did not move on the substrate prior to observation and were thus distributed randomly over the substrate as patches of cells (Fig 4.1D, G). Images of larger aggregate structures were difficult to acquire since the height of the cell aggregate was significantly greater than the maximum servo range (± 4300 nm) of the AFM scanner. This indicates a complex three-dimensional organization of cell aggregates. In some cases, the AFM cantilever could be centered on top of a large aggregate for image acquisition (Figure 4.1 E, H). A cross-section

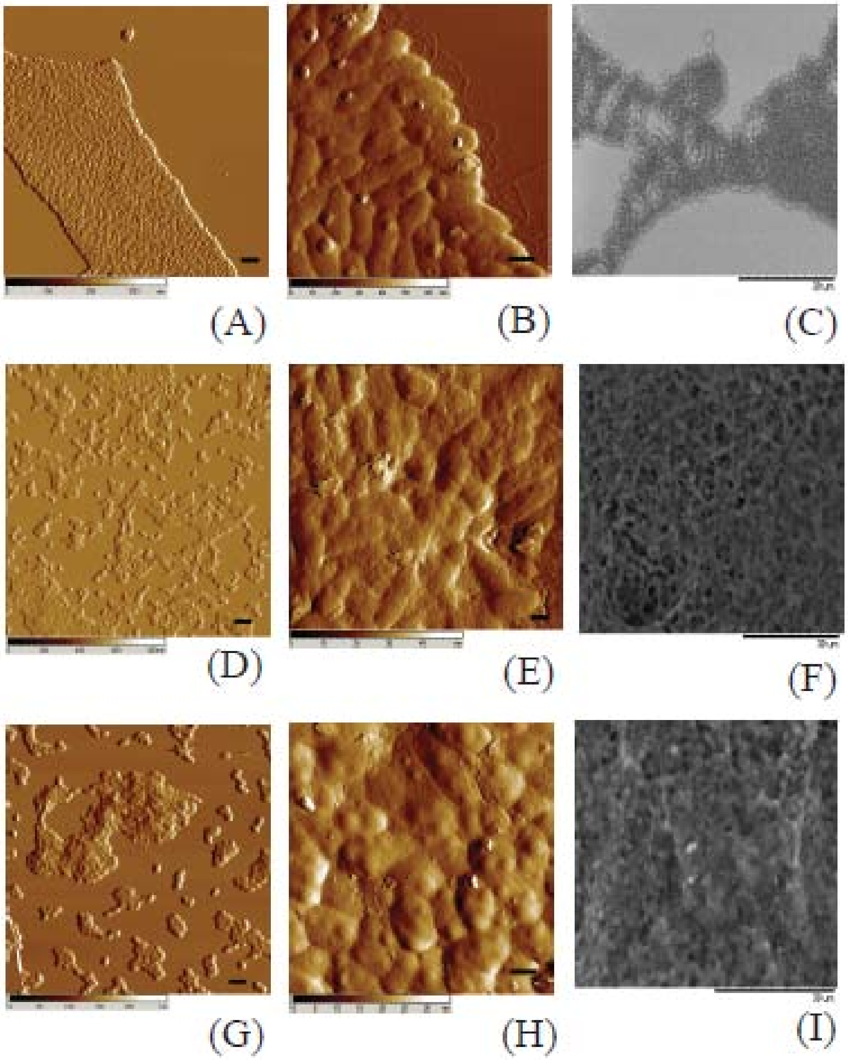

Figure 4.1 AFM and SEM images of *A. brasilense* Sp7 and mutant strains after 24 hours. Wild type Sp7 cells dried as a side-by-side monolayer of cells between 500-700 nm in height (A-C). AFM and SEM images *che1* mutant strains AB101 (Δ*cheA1*) (D-F). AFM and SEM images AB102 (Δ*cheY1*) (G-I). Scale bars for (A, D, G) represent 5 µm. Scale bars for (B, E, H) represent 500 nm. Scale bars on the SEM images (C), (F), (I) represent 30 µm.

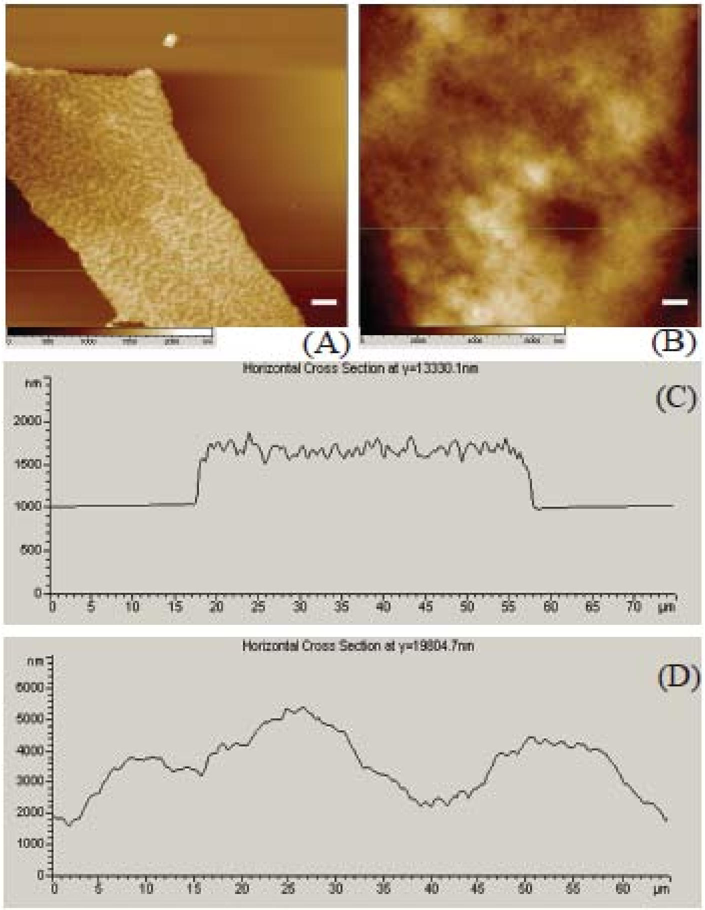

Figure 4.2 AFM micrographs of Sp7 cells (A) and AB101 (ΔcheA1) (B) after air drying. (C) Wild type Sp7 cells dried as a side-by-side monolayer of cells between 500-700 nm in height. (D) AB101 (Δ*cheA1)* flocs demonstrated a different pattern of cell organization when dried on the mica with much greater variations in height (ranging 3000 nm) over the floc structure. All scale bars represent 5 µm.

measurement taken from a topographic image of an AB101 (Δ*cheA1)* aggregate shows the height variation within the floc to be as great as 3 µm (Figure 4.2 B, D). AFM analysis and low magnification SEM analysis (75 µm^2) indicated that the flocculating mutant cells were tightly associated with each other and appeared to be encased in a thick extracellular matrix (Figure 4.1 F, I). In contrast, the extracellular matrix surrounding the non-flocculating wild type cells appeared less electron-dense and did not appear to extend beyond individual cells (Figure 4.1 C).

4.3.3. Comparison of extracellular matrix structures by AFM

Examination of AFM images revealed that the extracellular matrix of AB101 (ΔcheA1) and AB102 (ΔcheY1) contained fibrillar material at 24 h (Figure 4.3C and D and Figure 4.4 C and D). The extracellular matrix of AB101 (ΔcheA1) and AB102 (ΔcheY1) appeared as a ridged structure on the surface of cells with fibrils protruding from the cells (Figure 4.3C and D, Figure 4.4 C and D). In contrast, the extracellular material surrounding cells of the nonflocculating wild-type strain appeared to be smooth and globular at 24 h (Figure 4.4). Numerous high-resolution scans of wild-type nonflocculating cells failed to reveal fibrillar material (Figure 4.3 and data not shown). After 1 week, however, fibrillar material was observed for flocculating wild-type cells (Figure 4.3B and 4.4B). Despite the apparent similarity of the macroscopic flocculation phenotype of the mutant strains, analyses of AFM topography and deflection images revealed a dissimilarity in the organizational pattern of the aggregating cells (Figs 4.5). The most striking difference was observed in comparing the extracellular material of AB102 (ΔcheY1) with that of AB101 (ΔcheA1) or wild-type cells. A network of extracellular material is visible between the AB102 (ΔcheY1) cells as early as 24 h (data not shown) and becomes more

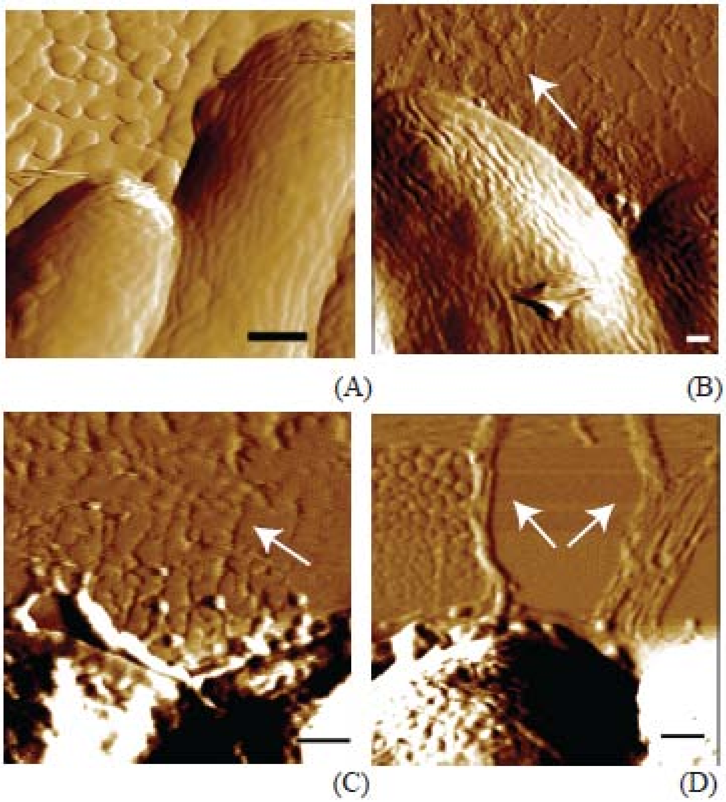

Figure 4.3 Flocculating che1 mutants produce a fibrillar material during premature flocculation. (A) Nonflocculating wild-type Sp7 at 24 h; (B) flocculating wild-type Sp7 at 1 week; (C) flocculating mutant strain AB101 (ΔcheA1) at 24 h; (D) flocculating mutant strain AB102(ΔcheY1) at 24 h. The white arrows point to the fibrillar material. All scale bars represent 200 nm.

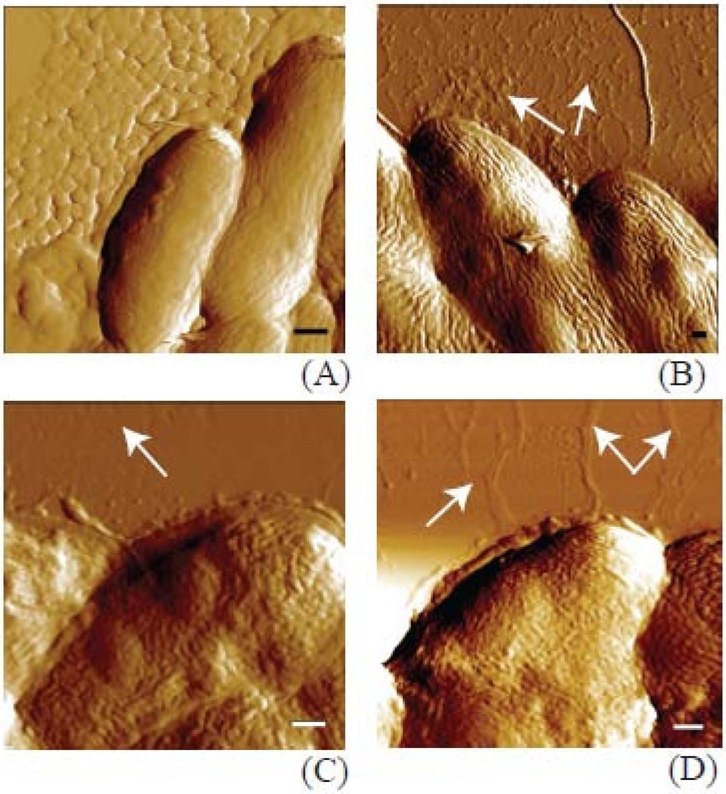

Figure 4.4 AFM 5x5 µm deflection scans of wild-type and mutant strains. (A) non-flocculating Wild type Sp7 at 24 hrs; (B) flocculating Wild type Sp7 at 1 week; (C) flocculating mutant strain AB101(*ΔcheA1*) at 24 hrs; (D) flocculating mutant strain AB102 (Δ*cheY1*) at 24 hrs. The white arrows point to the fibrillar material. Scale bars represent 200 nm.

distinct after 1 week (Figure 4.5C, F, and I). Line scans across the flocs indicate that AB102 (ΔcheY1) cells are embedded in a matrix that spans approximately 400nm between cells (Figure 4.5 I). This tight organization is not observed in flocs formed by AB101 (ΔcheA1) (Figure 4.5 H). In this strain, as well as in flocculating wild-type cells, individual cells are distinctly defined within the flocs and no obvious features are observed between the cells (Figure 4.5 I).

4.3.4. Flocculation inhibition assay

Previous studies have shown a correlation between flocculation and the production of arabinose-rich extracellular polysaccharides [164]. Based on this hypothesis, we next tested whether specific sugars found in the matrix were contributing to the premature flocculation phenotype of the Che1 mutants using a flocculation inhibition assay. We focused on the roles of glucose and arabinose since these sugars are primary components in EPS for planktonic and flocculating cells, respectively [164]. For this assay, wild type and mutant cells were grown in high C:N ratio liquid media for 24 hr, conditions that induce flocculation in the mutant strains but not the wild type strain. The cultures were then sonicated to break up the flocs and centrifuged to remove the cells. The remaining supernatant was then added to a culture of cells that were grown under non-flocculating conditions (low C:N ratio media) and cultured for an additional four hours. The addition of supernatant from flocculating cells to non-flocculating cell cultures has been shown previously to induce flocculation [212, 213]. If glucose or arabinose residues participate in the cell-to-cell adhesion mechanism during flocculation, however, the addition of either sugar along with the culture supernatant should block the binding sites and inhibit flocculation.

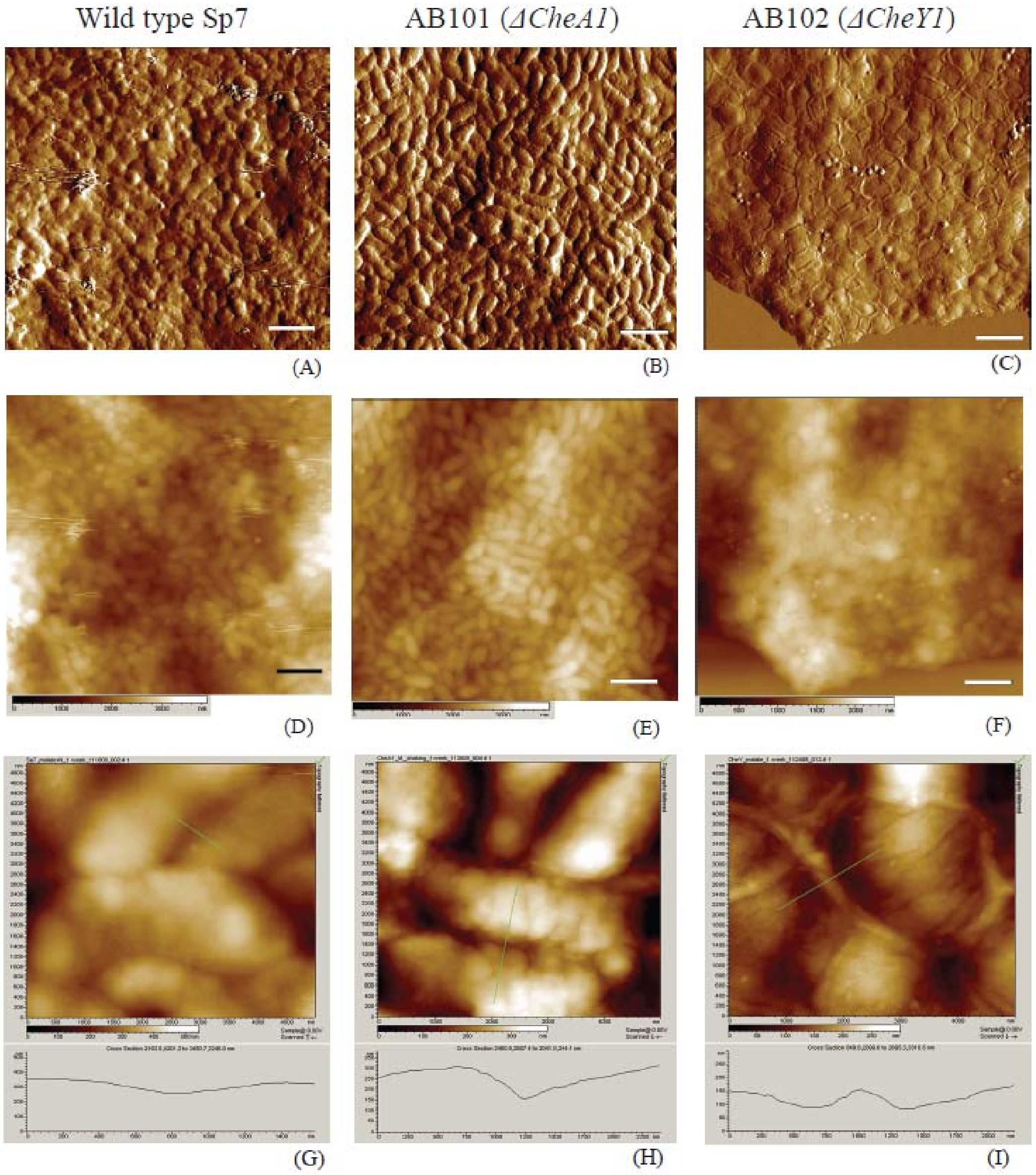

Figure 4.5 AFM images revealed dissimilarity in the organization of flocs between the two mutant strains. (A) Wild-type Sp7deflection; (B) AB101 (ΔcheA1) deflection; (C) AB102 (ΔcheY1) deflection; (D) Wild-type Sp7topography; (E) AB101 (ΔcheA1) topography; (F) AB102 (ΔcheY1) topography; (G) 5 mm^2 micrograph with a height cross-section measurement between wild-type cells; (H) between AB101 (ΔcheA1) cells; and (I) between AB102 (ΔcheY1) cells revealing a distinct extracellular material not observed for wild type or AB101 (ΔcheA1). Scale bars represent 5 mm.

As expected, the addition of supernatant from flocculating AB101 (*ΔcheA1*) to non-flocculating AB101 (*ΔcheA1*) cell cultures induced flocculation (Figure 4.6). The same result was obtained with the AB102 (*ΔcheY1*) cultures (Figure 4.6). We did not observe flocculation in the wild type culture after addition of supernatant derived from wild type cells grown in high C:N ratio media for 24 hr, consistent with the observation that the wild type cells were not flocculating when harvested (data not shown). The addition of 0.5M arabinose along with the supernatant was able to significantly reduce flocculation in both mutant strains, from approximately 90% to 55% flocculation for the AB101 (*ΔcheA1*) strain and from approximately 85% to less than 10% flocculation for AB102 (*ΔcheY1*) strain (Figure 4.6 A). The AB102 (*ΔcheY1*) strain was much more sensitive than AB101 (*ΔcheA1*) to the effects of arabinose addition, showing a significant reduction in flocculation with the addition of only 0.05M arabinose (Figure 4.6 A). Only high concentrations of glucose (0.5M), however, reduced flocculation in the mutant strains. Again, the AB102 (*ΔcheY1*) strain seemed to be more sensitive to the addition of glucose, showing almost complete blockage of flocculation after addition of 0.5M glucose with culture supernatant (Figure 4.6 B).

4.3.5. Lectin binding assay

Although CheA1 and CheY1 are encoded within the same operon and are proposed to participate in the same biochemical pathway [205, 209], AFM analysis and the flocculation inhibition assay suggest that mutants lacking CheA1 or CheY1 function may have differences in the extracellular matrix structure and/or composition. To further investigate this possibility, we used FITC-conjugated lectins to probe for specific carbohydrates present on the cell surface or in the extracellular matrix of the mutant cells. Lectins are proteins that recognize and bind specific

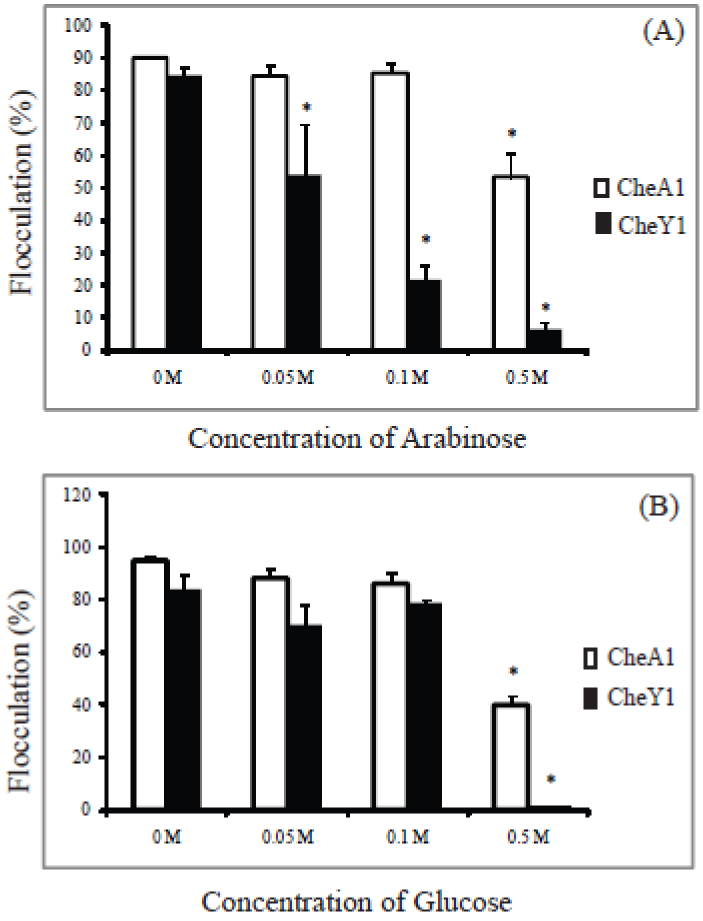

Figure 4.6 The effect of L-arabinose (A) and D-glucose (B) on flocculation for che1 mutants. The data in both (A) and (B) represent the average of three replicates for one representative experiment per strain. The asterisks represent significant differences in binding inhibition between the monosaccharide treated cultures as analyzed by one- and two-way ANOVA ($P = 0.05$).

carbohydrate residues [214], which make them ideal probes for investigating mono- or oligosaccharides in EPS or other extracellular structures. Previous studies have utilized fluorescently conjugated lectins to target sugars and protein receptors expressed on the surface of *A. brasilense* and *A. lipoferum* [170, 215, 216]. To further investigate differences in the extracellular matrix, we used FITC-conjugated lentil lectin (LcH) (affinity for amannose and α-glucose) and lima bean lectin (LBL) (affinity for N-acetyl galactosamine) to probe for specific carbohydrates present on or around the cell surface. Wild type cells did not show any significant binding of either lectin after 24 h of growth as determined by fluorescence imaging and statistical analysis (Figure 4.7; Table 4.2). Both lectins were found to stain AB101 (ΔcheA1) cells and the surrounding material (Figure 4.7B and H). In comparison with AB101, AB102 (ΔcheY1) cells displayed reduced staining by both lectins (Figure 4.7C and I). When normalized to the fluorescence signal of Syto61 that stains all cells (Figure 4D–F and J–L), the lectin fluorescence signal detected for AB102 (ΔcheY1) floc significantly ($P = 0.05$) reduced for both lectins with respect to AB101 (Table 4.2).

4.3.6. Lipopolysaccharide profiles

The lipopolysaccharides profiles of the mutant and wild type strains grown under flocculating and nonflocculating conditions were compared. Under conditions of growth in rich medium (TY), all strains had similar lipopolysaccharides profiles (Figure 4.8). Differences in lipopolysaccharides profiles were detected between the strains as early as 24 h of incubation in flocculation medium, which corresponds to the time at which both mutant strains, but not the wild type strain, flocculate. Under these conditions and compared with the lipopolysaccharides

Table 4.2 Quantification of lectin binding

	Wild type Sp7	**AB101 (Δ*cheA1*)**	**AB102 (Δ*cheY1*)**
Fluorescence intensity ratio for LcH:Syto61	0.00	0.70*†	0.01*†
Fluorescence intensity ratio for LBL:Syto61	0.00	0.42*†	0.04*†

*Significant difference between wild-type (*P* = 0.05).
†Significant difference between mutants (*P* = 0.05).

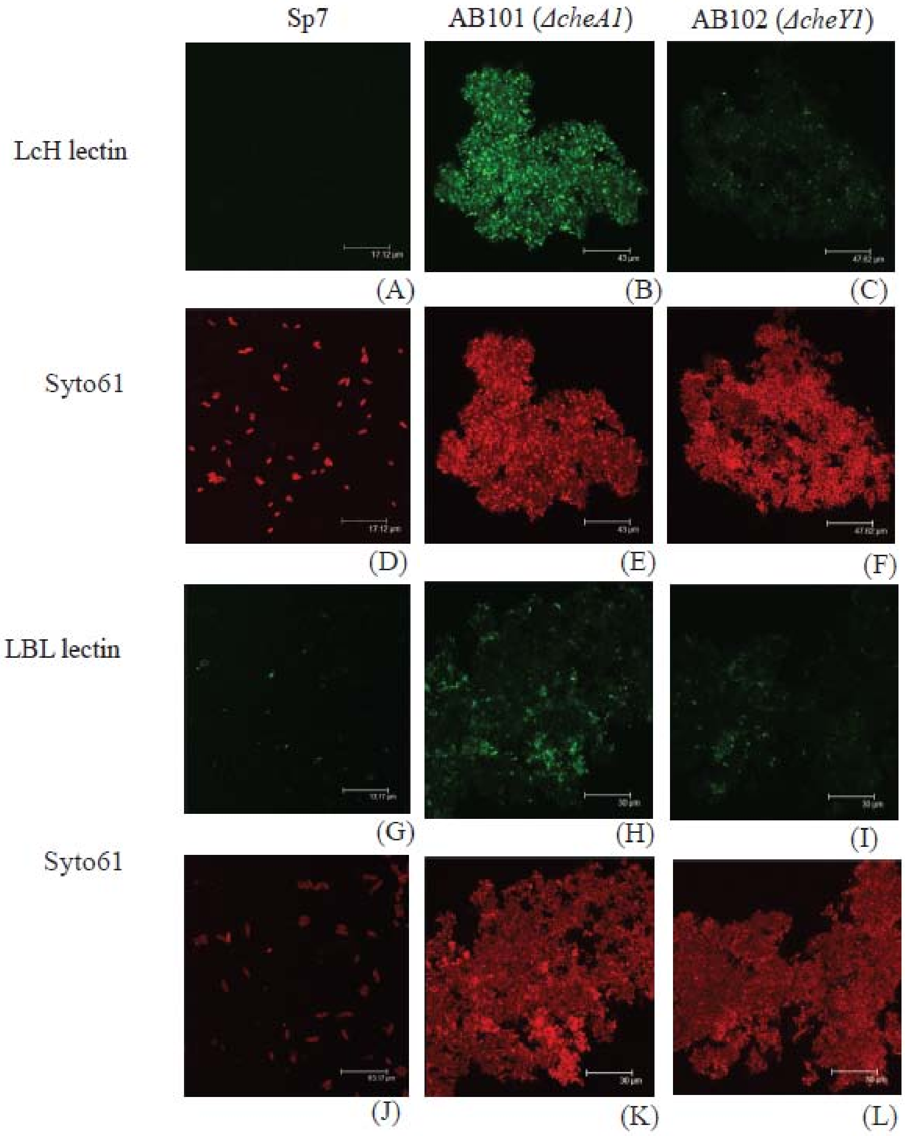

Figure 4.7 The che1 mutants differentially bind lentil (LcH) and lima bean (LBL) lectins. (A, D) wild-type stained with LcH and Syto61; (B, E) AB101(ΔcheA1) stained with LcH and Syto61; (C, F) AB102(ΔcheY1) stained with LcH and Syto61; (G, J) wild-type stained with LBL and Syto61; (H, K) AB101(ΔcheA1) stained with LBL and Syto61; (I, L) AB102(ΔcheY1) stained with LBL and Syto61.

profile of the wild-type strain, a low-molecular-weight band (arrow 2, Figure 4.8) is absent from the profile of both mutant strains while another low molecular-weight band (arrow 3, Figure 4.8) is significantly reduced. A higher molecular weight band (Figure 5, arrow 1) is also clearly visible for all strains, but more abundant in the lipopolysaccharides profile of both mutant strains at 24 h. After 1 week of incubation, the wild-type strain flocculated and its lipopolysaccharides profile mirrored that of the flocculated mutant strains: the lower molecular weight bands (arrows 2 and 3, Figure 4.8) are significantly fainter while a higher molecular weight band (arrow 1, Figure 4.8) shows an increase in relative abundance. Collectively, the data suggest that changes in the lipopolysaccharides profiles of flocculated cells are comparable for all strains, and that changes in lipopolysaccharides profiles are correlated and coincident with flocculation.

4.4. Discussion

In this study, we have used high-resolution atomic force microscopy to investigate the cell surface and the surrounding matrix of the *A. brasilense ΔcheA1* and *ΔcheY1* mutant cells during flocculation. The mechanism and regulation of flocculation in *A. brasilense* are receiving increased attention because flocculation is thought to contribute to the ability of cells to endure various stresses and is likely to be important for efficient plant root surface colonization [162, 168, 217-219]. Several investigations in recent years have supported the hypothesis that extracellular polysaccharides and outer membrane proteins are involved in cell-to-cell aggregation of *A. brasilense* spp. leading to flocculation in *Azospirillum* spp. [164, 170, 213, 215, 217]. Comparisons between AFM micrographs of planktonic and flocculating cells from this study indicate differences in cell surface characteristics that correlate to increased

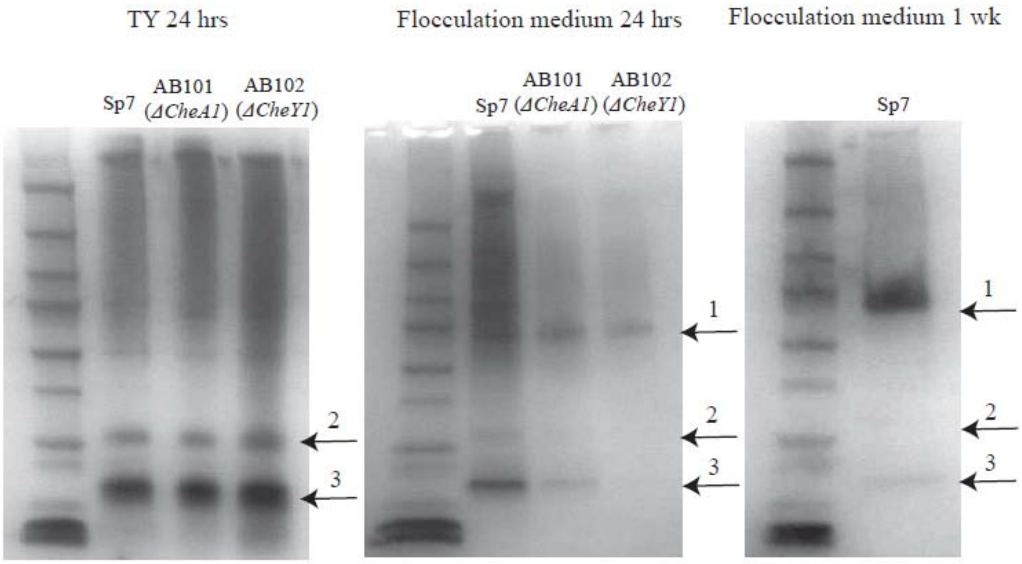

Figure 4.8 Lipopolysaccharides profile of wild-type Sp7 and mutant strains grown in nutrient TY and flocculation medium. Arrows indicate the bands discussed in the text.

flocculation behavior. Specifically, we detected fibrillar extracellular material at the edge of floc structures in both CheA1 and CheY1 mutant strains, which show premature flocculation behavior compared to wild type cells. The AFM images further indicate that this extracellular material is associated with the cell surface and encases multiple cells, suggesting that it may be particularly adhesive. It is interesting to note that the fibrillar material appeared to be more abundant on the surface of the AB102 (*ΔcheY1*) mutant strain, which correlates with the greater amount of flocculation consistently observed for this strain. Whether this fibrillar material associated with flocculating cells is related to or has a role similar to that of the fibrillar structures reportedly formed by *A. brasilense* Cd cells during aggregative attachment to wheat roots and sand particles remains to be determined [166].

Because CheA1 and CheY1 are encoded within the same operon and are proposed to participate in the same biochemical pathway, it may be expected that mutations in these components would result in similar phenotypes. Close examination of the strains with AFM, however, show clear distinctions between the strains in terms of cell organization within the flocs. Although the cells were adherent and embedded in a complex matrix, the *cheY1* mutant had distinct cell-to-cell contacts separated by a thick mucosal layer which was visible by AFM after 1 week. This layer formed a tight network around each individual cell within the floc. This tight organization was not observed in flocs formed by AB101 (Δ*cheA1)*. Rather, individual cells were distinctly defined within the flocs and no obvious features were observed between the cells.

Because it is impossible to determine the composition of this material from imaging alone, we used flocculation inhibition and lectin binding assays to begin comparing the two mutant strains in more detail. In addition to EPS, outer membrane proteins, porins, and cell surface lectins may play a role in the flocculation behavior of *Azospirillum* [161]. The results of the lectin binding assay suggest that the strain deficient in *cheA1* produces an EPS that is more abundant in α-mannose and/or α-glucose, and N-acetyl galactosamine than the EPS produced by AB102 (*ΔcheY1*). Previous studies have shown that the glucose content of EPS is significantly lower during flocculation in the wild type Sp7 strain and in other mutant derivative strains with increased aggregation capacity [164]. Consistent with these data, the AB102 (*ΔcheY1)* strain displays a stronger flocculation phenotype and appears to have a reduced mannose and/or glucose content compared to the AB101 strain. An alternative explanation for these data is that the structural organization of the AB102 (*ΔcheY1)* floc reduces the accessibility of the sugar residues to the lectin, thus limiting the amount of lectin that binds to the cells and surrounding matrix.

Even though the two mutant strains showed different binding affinities for lectins, indicating possible differences in polysaccharide composition of the EPS produced during flocculation, these results do not necessarily show the contribution of specific polysaccharides in aggregation. It has been previously reported that the arabinose content of EPS for aggregating wild type Sp7 and several Tn5 mutant strains greatly increases concomitantly with an increase in aggregation while the glucose content of EPS is reduced [164, 213]. Bahat-Samet et al [164] also demonstrated that the EPS composition in wild type cells is modified over time from a glucose rich EPS to an arabinose rich EPS and that this correlates directly to flocculation observed in minimal medium with limited nitrogen supplementation. Consistent with this observation, the *cheY1* mutant, which has a stronger flocculation phenotype, was more sensitive to the addition of arabinose in the flocculation inhibition assay, establishing the importance of L-arabinose during flocculation for the *cheY1* deficient strain. However, inhibition of flocculation was not observed for AB101 (Δ*cheA1)* at similar concentrations of L-arabinose, suggesting that the sugar residues comprising the matrix of this mutant strain are different in structure and/or abundance. These data support the possibility of a different mechanism of cellular aggregation between AB101 and AB102 strains. These data may also support the possibility of differential regulation of cellular aggregation between the strains. In other words, if the EPS composition is modified over time from a glucose rich EPS to an arabinose rich EPS which correlates to flocculation, then it is possible that the phenotypes of the two mutants may represent different stages of the flocculation process, with the CheY1 mutant being more advanced than the CheA1 mutant. This finding is significant since no other differences were highlighted previously between these two mutant strains. They are also unexpected since in accordance with the general paradigm of chemotaxis molecular pathways; AB101 and AB102 belong to the same signaling network and are expected to have similar phenotypes. However, the exact molecular mechanism underlying these differences remains to be determined.

Taken together, these results reveal that the extracellular matrix is structurally different depending on the flocculating behavior of the bacteria and thus support the notion that flocculation in *A. brasilense* is due to remodeling of the cell surface and associated with changes in the adhesive properties of the cell surface. The extent of this difference could be observed visually with the AFM where the matrix changes from a smooth, less adhesive substance (non-flocculating wild type cells) to a fibrous, sticky substance which appears to promote cell-to-cell adhesion (flocculating mutant strains). Given the adhesive properties of various EPS and the previous demonstration that EPS are involved in flocculation in wild type *A. brasilense* [164, 213], it is likely that changes in EPS structure or composition may also be involved in mediating Che1-dependent flocculation.

Chapter 5. Conclusions and future directions

5.1. Summary

The work presented here, represents a comprehensive investigation of both intra and extracellular interactions using advance microscopic techniques. We have facilitated the development of a fluorescence based assay for identification and quantification of PPIs *in vivo*. This represents a significant step forward in the advancement of *in vivo* tools to characterize protein interactions. More importantly, this assay is uniquely suited as a general quantitative screen *in vivo*, where it can be applied to multiple systems suitable for biological network analysis.

In addition, this work took advantage of the high resolution capabilities of AFM to investigate extracellular nanostructures mediating *A. brasilense* cell-to-cell interactions during flocculation. AFM revealed that the wild-type strain produces a smooth mucosal extracellular matrix after 24 h, the flocculating Che1 mutant strains produce distinctive extracellular fibril structures. Further analyses using flocculation inhibition, lectin-binding assays, and comparison of lipopolysaccharides profiles suggest that the extracellular matrix differs between the cheA1 and the cheY1 mutants, despite an apparent similarity in the macroscopic floc structures. As a result, the data in this study indicate that disruption of the Che1pathway is correlated with distinctive changes in the extracellular matrix, which likely result from changes in surface polysaccharides structure and/or composition.

5.2. Future Directions

Although we have demonstrated success with the intracellular and extracellular methodologies that were developed with this project, there will always be a need to improve upon existing methods. For example, the co-localization/FRAP assay is currently limited to quantification of the k_{off} rate for PPIs under investigation. However, we are actively working on a simulation to mathematically fit FRAP recovery curves while acquiring k_{on} data. The new binding models will incorporate an additional parameter, the number of available binding sites at the cell pole. This parameter is benchmarked against a model of DivIVA coverage at the cell poles derived from TEM data [220] . The TEM work reported by Stahlberg et. al. revealed that DivIVA oligomerizes in a stringed "doggy-bone" structures. These strings then form a mesh-work of protein along the negative curvature of the cell pole [220, 221]. Moreover, they calculated the dimensions of an individual "doggy-bone" shaped particle. Each particle is comprised of a DivIVA hexameric or octomeric oligomer where each of these particles are 22.4 ± 3 nm long and 2.0 ± 0.4 nm wide. For the co-localization assay, each particle will have 6-8 total binding sites where the maximum number of available binding sites is 0.023 sites per nm^2 to 0.031 sites per nm^2. The data acquired from the CellConstruct routine are imported into a MatLab ProteinDisplacement routine. The total protein concentration observed during experiments is introduced into the allowed to reach equilibrium in terms of the bound fraction. A simulated bleach pulse is applied and the best fit values are selected as the simulation runs through recovery (Figure 5.1). The simulation routine is in the early stages of development, but preliminary results are promising.

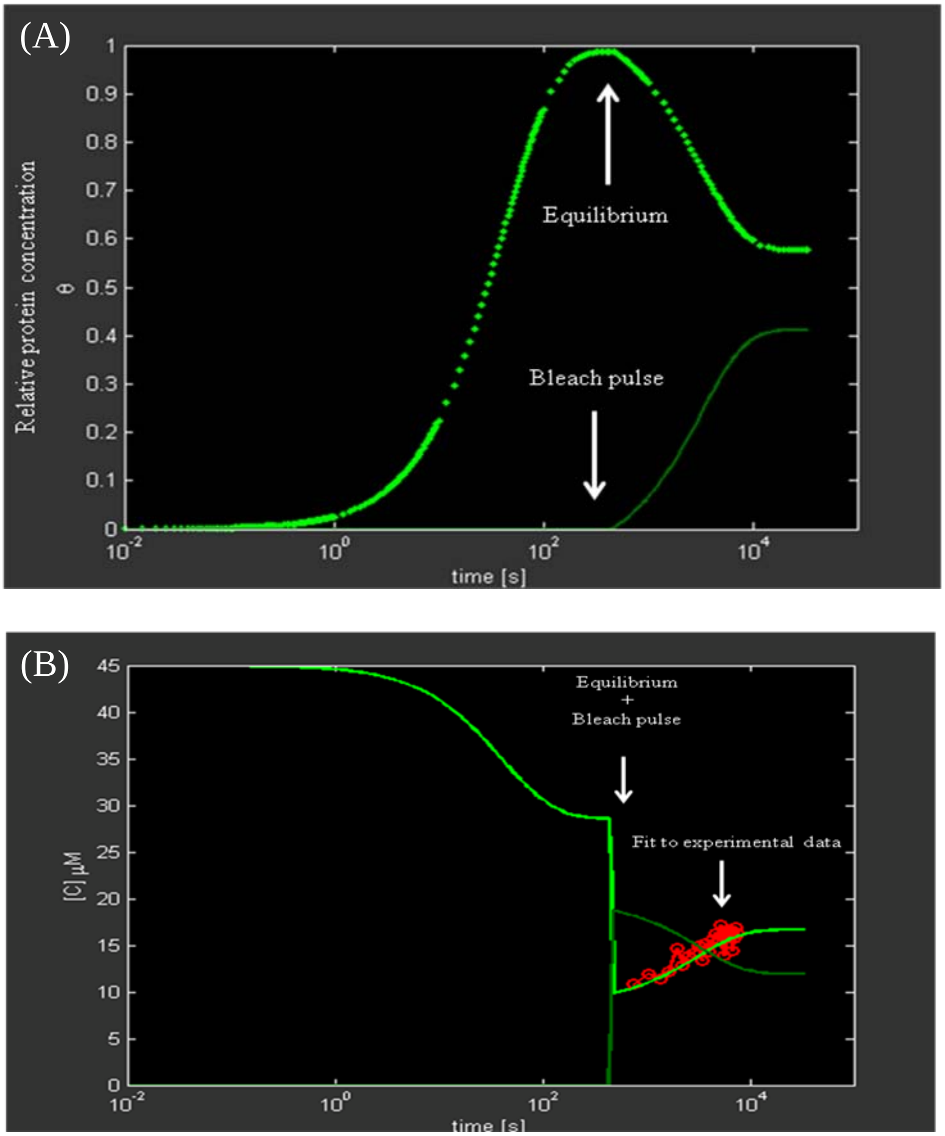

Figure 5.1 MatLab ProteinDisplacement routine. (A) Simulation of all mobile fluorescent protein in an *E. coli* cell. Here, protein saturation is normalized to a value of 1 (where 1 is the equilibrium state) and plotted as a function of time (s). The bright green plot represents fluorescent protein and the dark green represents photobleached protein. A bleach pulse is simulated at the equilibrium state, reducing the amount of fluorescent protein and increasing the amount of photobleached protein as a function of time. (B) A simulation is fit to the experimental data in order to calculate k_{off} and k_{on} rates. The number of available binding sites at the poles and the probable K_D value is put into the simulation. After the bleach pulse is applied, recovery occurs. The simulation is run against the experimental data to determine the best fit.

LIST OF REFERENCES

1. Melhado, E.M., ***Jacob Berzelius, the emergence of his chemical system*** 1981, Madison: Almqvist & Wiksell International
2. Alberts, B., *The cell as a collection of protein machines: preparing the next generation of molecular biologists.* Cell, 1998. **92**(3): p. 291-4.
3. Cusick, M.E., et al., *Interactome: gateway into systems biology.* Hum Mol Genet, 2005. **14 Spec No. 2**: p. R171-81.
4. Nooren, I.M. and J.M. Thornton, *Diversity of protein-protein interactions.* Embo J, 2003. **22**(14): p. 3486-92.
5. Rohs, R., et al., *Origins of specificity in protein-DNA recognition.* Annu Rev Biochem. **79**: p. 233-69.
6. Katsamba, P.S., S. Park, and I.A. Laird-Offringa, *Kinetic studies of RNA-protein interactions using surface plasmon resonance.* Methods, 2002. **26**(2): p. 95-104.
7. Masi, A., et al., *Optical methods in the study of protein-protein interactions.* Adv Exp Med Biol. **674**: p. 33-42.
8. Gavin, A.C., et al., *Functional organization of the yeast proteome by systematic analysis of protein complexes.* Nature, 2002. **415**(6868): p. 141-7.
9. Valente, A.X., et al., *Functional organization of the yeast proteome by a yeast interactome map.* Proc Natl Acad Sci U S A, 2009. **106**(5): p. 1490-5.
10. Reichmann, D., et al., *The molecular architecture of protein-protein binding sites.* Curr Opin Struct Biol, 2007. **17**(1): p. 67-76.
11. Shen, J., et al., *Predicting protein-protein interactions based only on sequences information.* Proc Natl Acad Sci U S A, 2007. **104**(11): p. 4337-41.
12. Panjkovich, A. and P. Aloy, *Predicting protein-protein interaction specificity through the integration of three-dimensional structural information and the evolutionary record of protein domains.* Mol Biosyst. **6**(4): p. 741-9.
13. Soong, T.T., K.O. Wrzeszczynski, and B. Rost, *Physical protein-protein interactions predicted from microarrays.* Bioinformatics, 2008. **24**(22): p. 2608-14.
14. Charbonnier, S., O. Gallego, and A.C. Gavin, *The social network of a cell: recent advances in interactome mapping.* Biotechnol Annu Rev, 2008. **14**: p. 1-28.
15. Phizicky, E.M. and S. Fields, *Protein-protein interactions: methods for detection and analysis.* Microbiol Rev, 1995. **59**(1): p. 94-123.
16. Piehler, J., *New methodologies for measuring protein interactions in vivo and in vitro.* Curr Opin Struct Biol, 2005. **15**(1): p. 4-14.
17. Berggard, T., S. Linse, and P. James, *Methods for the detection and analysis of protein-protein interactions.* Proteomics, 2007. **7**(16): p. 2833-42.
18. Kuroda, K., et al., *Systems for the detection and analysis of protein-protein interactions.* Appl Microbiol Biotechnol, 2006. **71**(2): p. 127-36.
19. Phizicky, E., et al., *Protein analysis on a proteomic scale.* Nature, 2003. **422**(6928): p. 208-15.
20. Zhou, M. and T.D. Veenstra, *Proteomic analysis of protein complexes.* Proteomics, 2007. **7**(16): p. 2688-97.
21. Ratner, D., *The interaction bacterial and phage proteins with immobilized Escherichia coli RNA polymerase.* J Mol Biol, 1974. **88**(2): p. 373-83.
22. Shoemaker, B.A. and A.R. Panchenko, *Deciphering protein-protein interactions. Part I. Experimental techniques and databases.* PLoS Comput Biol, 2007. **3**(3): p. e42.

23. Xu, X., et al., *The tandem affinity purification method: an efficient system for protein complex purification and protein interaction identification.* Protein Expr Purif, 2010. **72**(2): p. 149-56.
24. Arifuzzaman, M., et al., *Large-scale identification of protein-protein interaction of Escherichia coli K-12.* Genome Res, 2006. **16**(5): p. 686-91.
25. Butland, G., et al., *Interaction network containing conserved and essential protein complexes in Escherichia coli.* Nature, 2005. **433**(7025): p. 531-7.
26. Ho, Y., et al., *Systematic identification of protein complexes in Saccharomyces cerevisiae by mass spectrometry.* Nature, 2002. **415**(6868): p. 180-3.
27. Krogan, N.J., et al., *Global landscape of protein complexes in the yeast Saccharomyces cerevisiae.* Nature, 2006. **440**(7084): p. 637-43.
28. Pelletier, D.A., et al., *A General System for Studying Protein-Protein Interactions in Gram-Negative Bacteria.* J Proteome Res, 2008. **7**(8): p. 3319-3328.
29. MacBeath, G., *Protein microarrays and proteomics.* Nat Genet, 2002. **32 Suppl**: p. 526-32.
30. Zhu, H., et al., *Global analysis of protein activities using proteome chips.* Science, 2001. **293**(5537): p. 2101-5.
31. Haab, B.B., M.J. Dunham, and P.O. Brown, *Protein microarrays for highly parallel detection and quantitation of specific proteins and antibodies in complex solutions.* Genome Biol, 2001. **2**(2): p. RESEARCH0004.
32. Mitchell, P., *A perspective on protein microarrays.* Nat Biotechnol, 2002. **20**(3): p. 225-9.
33. Caputo, E., R. Moharram, and B.M. Martin, *Methods for on-chip protein analysis.* Anal Biochem, 2003. **321**(1): p. 116-24.
34. Javanmard, M., et al., *A Microfluidic Platform for Characterization of Protein-Protein Interactions.* IEEE Sens J, 2009. **9**(8): p. 883-891.
35. Srisa-Art, M., et al., *Analysis of protein-protein interactions by using droplet-based microfluidics.* Chembiochem, 2009. **10**(10): p. 1605-11.
36. Rivas, G., F. Ferrone, and J. Herzfeld, *Life in a crowded world.* EMBO Rep, 2004. **5**(1): p. 23-7.
37. Zhou, Y.L., et al., *Macromolecular crowding enhances the binding of superoxide dismutase to xanthine oxidase: implications for protein-protein interactions in intracellular environments.* Int J Biochem Cell Biol, 2006. **38**(11): p. 1986-94.
38. Sun, J. and H. Weinstein, *Toward realistic modeling of dynamic processes in cell signaling: quantification of macromolecular crowding effects.* J Chem Phys, 2007. **127**(15): p. 155105.
39. Jarvik, J. and D. Botstein, *Conditional-lethal mutations that suppress genetic defects in morphogenesis by altering structural proteins.* Proc Natl Acad Sci U S A, 1975. **72**(7): p. 2738-42.
40. Moir, D., et al., *Cold-sensitive cell-division-cycle mutants of yeast: isolation, properties, and pseudoreversion studies.* Genetics, 1982. **100**(4): p. 547-63.
41. Novick, P., B.C. Osmond, and D. Botstein, *Suppressors of yeast actin mutations.* Genetics, 1989. **121**(4): p. 659-74.

42. Rokop, M.E. and A.D. Grossman, *Intragenic and extragenic suppressors of temperature sensitive mutations in the replication initiation genes dnaD and dnaB of Bacillus subtilis.* PLoS One, 2009. **4**(8): p. e6774.
43. Dobzhansky, T., *Genetics of Natural Populations. Xiii. Recombination and Variability in Populations of Drosophila Pseudoobscura.* Genetics, 1946. **31**(3): p. 269-90.
44. Fields, S. and O. Song, *A novel genetic system to detect protein-protein interactions.* Nature, 1989. **340**(6230): p. 245-6.
45. Parrish, J.R., K.D. Gulyas, and R.L. Finley, Jr., *Yeast two-hybrid contributions to interactome mapping.* Curr Opin Biotechnol, 2006. **17**(4): p. 387-93.
46. Fields, S., *High-throughput two-hybrid analysis. The promise and the peril.* FEBS J, 2005. **272**(21): p. 5391-9.
47. Uetz, P., et al., *A comprehensive analysis of protein-protein interactions in Saccharomyces cerevisiae.* Nature, 2000. **403**(6770): p. 623-7.
48. Ito, T., et al., *A comprehensive two-hybrid analysis to explore the yeast protein interactome.* Proc Natl Acad Sci U S A, 2001. **98**(8): p. 4569-74.
49. Li, S., et al., *A map of the interactome network of the metazoan C. elegans.* Science, 2004. **303**(5657): p. 540-3.
50. Giot, L., et al., *A protein interaction map of Drosophila melanogaster.* Science, 2003. **302**(5651): p. 1727-36.
51. Bader, J.S. and J. Chant, *Systems biology. When proteomes collide.* Science, 2006. **311**(5758): p. 187-8.
52. Lievens, S., I. Lemmens, and J. Tavernier, *Mammalian two-hybrids come of age.* Trends Biochem Sci, 2009. **34**(11): p. 579-88.
53. Johnsson, N. and A. Varshavsky, *Split ubiquitin as a sensor of protein interactions in vivo.* Proc Natl Acad Sci U S A, 1994. **91**(22): p. 10340-4.
54. Stagljar, I., et al., *A genetic system based on split-ubiquitin for the analysis of interactions between membrane proteins in vivo.* Proc Natl Acad Sci U S A, 1998. **95**(9): p. 5187-92.
55. Iyer, K., et al., *Utilizing the split-ubiquitin membrane yeast two-hybrid system to identify protein-protein interactions of integral membrane proteins.* Sci STKE, 2005 (275): p. l3.
56. Vaynberg, J. and J. Qin, *Weak protein-protein interactions as probed by NMR spectroscopy.* Trends Biotechnol, 2006. **24**(1): p. 22-7.
57. O'Connell, M.R., R. Gamsjaeger, and J.P. Mackay, *The structural analysis of protein-protein interactions by NMR spectroscopy.* Proteomics, 2009. **9**(23): p. 5224-32.
58. Zuiderweg, E.R., *Mapping protein-protein interactions in solution by NMR spectroscopy.* Biochemistry (Mosc), 2002. **41**(1): p. 1-7.
59. Vaynberg, J., et al., *Structure of an ultraweak protein-protein complex and its crucial role in regulation of cell morphology and motility.* Mol Cell, 2005. **17**(4): p. 513-23.
60. Navratilova, I., M. Dioszegi, and D.G. Myszka, *Analyzing ligand and small molecule binding activity of solubilized GPCRs using biosensor technology.* Anal Biochem, 2006. **355**(1): p. 132-9.
61. Chen, K., H. Obinata, and T. Izumi, *Detection of G protein-coupled receptor-mediated cellular response involved in cytoskeletal rearrangement using surface plasmon resonance.* Biosens Bioelectron. **25**(7): p. 1675-80.

62. Hruby, V.J. and G. Tollin, *Plasmon-waveguide resonance (PWR) spectroscopy for directly viewing rates of GPCR/G-protein interactions and quantifying affinities.* Curr Opin Pharmacol, 2007. **7**(5): p. 507-14.
63. Reimhult, E., et al., *A multitechnique study of liposome adsorption on Au and lipid bilayer formation on SiO2.* Langmuir, 2006. **22**(7): p. 3313-9.
64. Tawa, K. and K. Morigaki, *Substrate-supported phospholipid membranes studied by surface plasmon resonance and surface plasmon fluorescence spectroscopy.* Biophys J, 2005. **89**(4): p. 2750-8.
65. Harding, P.J., et al., *Direct analysis of a GPCR-agonist interaction by surface plasmon resonance.* Eur Biophys J, 2006. **35**(8): p. 709-12.
66. Rich, R.L. and D.G. Myszka, *Higher-throughput, label-free, real-time molecular interaction analysis.* Anal Biochem, 2007. **361**(1): p. 1-6.
67. Maynard, J.A., et al., *Surface plasmon resonance for high-throughput ligand screening of membrane-bound proteins.* Biotechnol J, 2009. **4**(11): p. 1542-58.
68. Boozer, C., et al., *Looking towards label-free biomolecular interaction analysis in a high-throughput format: a review of new surface plasmon resonance technologies.* Curr Opin Biotechnol, 2006. **17**(4): p. 400-5.
69. Jameson, D.M. and G. Mocz, *Fluorescence polarization/anisotropy approaches to study protein-ligand interactions: effects of errors and uncertainties.* Methods Mol Biol, 2005. **305**: p. 301-22.
70. Mocz, G., *Information content of fluorescence polarization and anisotropy.* J Fluoresc, 2006. **16**(4): p. 511-24.
71. Park, S.H. and R.T. Raines, *Fluorescence polarization assay to quantify protein-protein interactions.* Methods Mol Biol, 2004. **261**: p. 161-6.
72. Lakowicz, J.R., ***Principles of Fluorescence Spectroscopy***. 3 ed. 2006, New York: Springer.
73. Leopoldo, M., et al., *Developments in fluorescent probes for receptor research.* Drug Discov Today, 2009. **14**(13-14): p. 706-12.
74. Gradinaru, C.C., et al., *Fluorescence anisotropy: from single molecules to live cells.* Analyst. **135**(3): p. 452-9.
75. Fanara, P., et al., *Quantitative analysis of nuclear localization signal (NLS)-importin alpha interaction through fluorescence depolarization. Evidence for auto-inhibitory regulation of NLS binding.* J Biol Chem, 2000. **275**(28): p. 21218-23.
76. Hodel, M.R., A.H. Corbett, and A.E. Hodel, *Dissection of a nuclear localization signal.* J Biol Chem, 2001. **276**(2): p. 1317-25.
77. Harreman, M.T., et al., *Regulation of nuclear import by phosphorylation adjacent to nuclear localization signals.* J Biol Chem, 2004. **279**(20): p. 20613-21.
78. Hodel, A.E., et al., *Nuclear localization signal receptor affinity correlates with in vivo localization in Saccharomyces cerevisiae.* J Biol Chem, 2006. **281**(33): p. 23545-56.
79. Rost, F.W.D., *Fluorescence Microscopy*. Vol. 2. 1995, New York, NY: Cambridge University Press.
80. Du, W., et al., *Optical molecular imaging for systems biology: from molecule to organism.* Anal Bioanal Chem, 2006. **386**(3): p. 444-57.
81. Ntziachristos, V., *Going deeper than microscopy: the optical imaging frontier in biology.* Nat Methods. **7**(8): p. 603-14.

82. Davenport, D.N., J. A. C. . *Luminescence in Hydromedusae* in *Proceedings of the Royal Society of Loudon*. 1955: The Royal Society.
83. Shimomura, O., F.H. Johnson, and Y. Saiga, *Extraction, purification and properties of aequorin, a bioluminescent protein from the luminous hydromedusan, Aequorea.* J Cell Comp Physiol, 1962. **59**: p. 223-39.
84. Shimomura, O., F.H. Johnson, and H. Morise, *Mechanism of the luminescent intramolecular reaction of aequorin.* Biochemistry (Mosc), 1974. **13**(16): p. 3278-86.
85. Morise, H., et al., *Intermolecular energy transfer in the bioluminescent system of Aequorea.* Biochemistry (Mosc), 1974. **13**(12): p. 2656-62.
86. Shimomura, O., *The discovery of aequorin and green fluorescent protein.* J Microsc, 2005. **217**(Pt 1): p. 1-15.
87. Chalfie, M., et al., *Green fluorescent protein as a marker for gene expression.* Science, 1994. **263**(5148): p. 802-5.
88. Zhang, J., et al., *Creating new fluorescent probes for cell biology.* Nat Rev Mol Cell Biol, 2002. **3**(12): p. 906-18.
89. Shaner, N.C., et al., *Improved monomeric red, orange and yellow fluorescent proteins derived from Discosoma sp. red fluorescent protein.* Nat Biotechnol, 2004. **22**(12): p. 1567-72.
90. Patterson, G.H. and J. Lippincott-Schwartz, *A photoactivatable GFP for selective photolabeling of proteins and cells.* Science, 2002. **297**(5588): p. 1873-7.
91. Baker, S.M., R.W. Buckheit, 3rd, and M.M. Falk, *Green-to-red photoconvertible fluorescent proteins: tracking cell and protein dynamics on standard wide-field mercury arc-based microscopes.* BMC Cell Biol. **11**: p. 15.
92. Amos, W.B. and J.G. White, *How the confocal laser scanning microscope entered biological research.* Biol Cell, 2003. **95**(6): p. 335-42.
93. Minsky, M., *Memoir on Inventing the Confocal Scanning Microscope.* Scanning, 1988. **10**: p. 128-138.
94. Semwogerere, D.W., E R, *Confocal Microscopy*, in ***Encyclopedia of Biomaterials and Biomedical Engineering*** G.L.B.G. Wnek, Editor. 2005.
95. Piston, D.W. and G.J. Kremers, *Fluorescent protein FRET: the good, the bad and the ugly.* Trends Biochem Sci, 2007. **32**(9): p. 407-14.
96. Wallrabe, H. and A. Periasamy, *Imaging protein molecules using FRET and FLIM microscopy.* Curr Opin Biotechnol, 2005. **16**(1): p. 19-27.
97. Nguyen, A.W. and P.S. Daugherty, *Evolutionary optimization of fluorescent proteins for intracellular FRET.* Nat Biotechnol, 2005. **23**(3): p. 355-60.
98. Ai, H.W., et al., *Directed evolution of a monomeric, bright and photostable version of Clavularia cyan fluorescent protein: structural characterization and applications in fluorescence imaging.* Biochem J, 2006. **400**(3): p. 531-40.
99. Subach, F.V., et al., *Red fluorescent protein with reversibly photoswitchable absorbance for photochromic FRET.* Chem Biol. **17**(7): p. 745-55.
100. Rizzo, M.A., et al., *An improved cyan fluorescent protein variant useful for FRET.* Nat Biotechnol, 2004. **22**(4): p. 445-9.
101. Nagai, T., et al., *A variant of yellow fluorescent protein with fast and efficient maturation for cell-biological applications.* Nat Biotechnol, 2002. **20**(1): p. 87-90.

102. Terskikh, A.V., et al., *Analysis of DsRed Mutants. Space around the fluorophore accelerates fluorescence development.* J Biol Chem, 2002. **277**(10): p. 7633-6.
103. Campbell, R.E., et al., *A monomeric red fluorescent protein.* Proc Natl Acad Sci U S A, 2002. **99**(12): p. 7877-82.
104. Buntru, A., T. Zimmermann, and C.R. Hauck, *Fluorescence resonance energy transfer (FRET)-based subcellular visualization of pathogen-induced host receptor signaling.* BMC Biol, 2009. **7**: p. 81.
105. Bacart, J., et al., *The BRET technology and its application to screening assays.* Biotechnol J, 2008. **3**(3): p. 311-24.
106. Xu, X., et al., *Imaging protein interactions with bioluminescence resonance energy transfer (BRET) in plant and mammalian cells and tissues.* Proc Natl Acad Sci U S A, 2007. **104**(24): p. 10264-9.
107. Xu, Y., D.W. Piston, and C.H. Johnson, *A bioluminescence resonance energy transfer (BRET) system: application to interacting circadian clock proteins.* Proc Natl Acad Sci U S A, 1999. **96**(1): p. 151-6.
108. Hu, C.D., Y. Chinenov, and T.K. Kerppola, *Visualization of interactions among bZIP and Rel family proteins in living cells using bimolecular fluorescence complementation.* Mol Cell, 2002. **9**(4): p. 789-98.
109. Magliery, T.J., et al., *Detecting protein-protein interactions with a green fluorescent protein fragment reassembly trap: scope and mechanism.* J Am Chem Soc, 2005. **127**(1): p. 146-57.
110. Shyu, Y.J., et al., *Identification of new fluorescent protein fragments for bimolecular fluorescence complementation analysis under physiological conditions.* Biotechniques, 2006. **40**(1): p. 61-6.
111. Wilson, C.G., T.J. Magliery, and L. Regan, *Detecting protein-protein interactions with GFP-fragment reassembly.* Nat Methods, 2004. **1**(3): p. 255-62.
112. Rebois, R.V., et al., *Combining protein complementation assays with resonance energy transfer to detect multipartner protein complexes in living cells.* Methods, 2008. **45**(3): p. 214-8.
113. Sprague, B.L. and J.G. McNally, *FRAP analysis of binding: proper and fitting.* Trends Cell Biol, 2005. **15**(2): p. 84-91.
114. McNally, J.G., *Quantitative FRAP in analysis of molecular binding dynamics in vivo.* Methods Cell Biol, 2008. **85**: p. 329-51.
115. Carrero, G., et al., *Quantification of protein-protein and protein-DNA interactions in vivo, using fluorescence recovery after photobleaching.* Methods Enzymol, 2004. **375**: p. 415-42.
116. Hinow, P., et al., *The DNA binding activity of p53 displays reaction-diffusion kinetics.* Biophys J, 2006. **91**(1): p. 330-42.
117. Lele, T., et al., *An improved mathematical approach for determination of molecular kinetics in living cells with FRAP*. Mech Chem Biosyst, 2004. **1**(3): p. 181-90.
118. Sprague, B.L., et al., *Analysis of binding reactions by fluorescence recovery after photobleaching.* Biophys J, 2004. **86**(6): p. 3473-95.
119. Slepchenko, B.M., et al., *Quantitative cell biology with the Virtual Cell.* Trends Cell Biol, 2003. **13**(11): p. 570-6.

120. Farla, P., et al., *The androgen receptor ligand-binding domain stabilizes DNA binding in living cells.* J Struct Biol, 2004. **147**(1): p. 50-61.
121. Carrero, G., et al., *Using FRAP and mathematical modeling to determine the in vivo kinetics of nuclear proteins.* Methods, 2003. **29**(1): p. 14-28.
122. Sprague, B.L., et al., *Analysis of binding at a single spatially localized cluster of binding sites by fluorescence recovery after photobleaching.* Biophys J, 2006. **91**(4): p. 1169-91.
123. McNally, J.G., et al., *The glucocorticoid receptor: rapid exchange with regulatory sites in living cells.* Science, 2000. **287**(5456): p. 1262-5.
124. Schulmeister, S., et al., *Protein exchange dynamics at chemoreceptor clusters in Escherichia coli.* Proc Natl Acad Sci U S A, 2008. **105**(17): p. 6403-8.
125. Jefferson, K.K., *What drives bacteria to produce a biofilm?* FEMS Microbiol Lett, 2004. **236**(2): p. 163-73.
126. Kumar, A.S., K. Mody, and B. Jha, *Bacterial exopolysaccharides--a perception.* J Basic Microbiol, 2007. **47**(2): p. 103-17.
127. Flemming, H.C. and J. Wingender, *The biofilm matrix.* Nat Rev Microbiol. **8**(9): p. 623-33.
128. Abu-Lail, N.I. and T.A. Camesano, *Polysaccharide properties probed with atomic force microscopy.* J Microsc, 2003. **212**(Pt 3): p. 217-38.
129. Okeke, I.N. and J.P. Nataro, *Enteroaggregative Escherichia coli.* Lancet Infect Dis, 2001. **1**(5): p. 304-13.
130. Vial, P.A., et al., *Characterization of enteroadherent-aggregative Escherichia coli, a putative agent of diarrheal disease.* J Infect Dis, 1988. **158**(1): p. 70-9.
131. Ljungh, A.W., T., *Fimbriation in relation to hydrophobicity of bacteria in urinary tract infection.* Eur J Clin Microbiol, 1985. **3**: p. 568-570.
132. Wai, S.N., A. Takade, and K. Amako, *The hydrophobic surface protein layer of enteroaggregative Escherichia coli strains.* FEMS Microbiol Lett, 1996. **135**(1): p. 17-22.
133. Kaplan, H.B., *Cell-cell interactions that direct fruiting body development in Myxococcus xanthus.* Curr Opin Genet Dev, 1991. **1**(3): p. 363-9.
134. Ward, M.J. and D.R. Zusman, *Motility in Myxococcus xanthus and its role in developmental aggregation.* Curr Opin Microbiol, 1999. **2**(6): p. 624-9.
135. Jelsbak, L. and L. Sogaard-Andersen, *Cell behavior and cell-cell communication during fruiting body morphogenesis in Myxococcus xanthus.* J Microbiol Methods, 2003. **55**(3): p. 829-39.
136. Dworkin, M., *Fibrils as extracellular appendages of bacteria: their role in contact-mediated cell-cell interactions in Myxococcus xanthus.* Bioessays, 1999. **21**(7): p. 590-5.
137. Behmlander, R.M. and M. Dworkin, *Biochemical and Structural-Analyses of the Extracellular-Matrix Fibrils of Myxococcus-Xanthus.* Journal of Bacteriology, 1994. **176**(20): p. 6295-6303.
138. Yang, Z., et al., *Myxococcus xanthus dif genes are required for biogenesis of cell surface fibrils essential for social gliding motility.* J Bacteriol, 2000. **182**(20): p. 5793-8.
139. Bellenger, K., et al., *A CheW homologue is required for Myxococcus xanthus fruiting body development, social gliding motility, and fibril biogenesis.* J Bacteriol, 2002. **184**(20): p. 5654-60.
140. Branda, S.S., et al., *Biofilms: the matrix revisited.* Trends Microbiol, 2005. **13**(1): p. 20-6.

141. Tielen, P., et al., *Extracellular enzymes affect biofilm formation of mucoid Pseudomonas aeruginosa.* Microbiology. **156**(Pt 7): p. 2239-52.
142. Ryder, C., M. Byrd, and D.J. Wozniak, *Role of polysaccharides in Pseudomonas aeruginosa biofilm development.* Curr Opin Microbiol, 2007. **10**(6): p. 644-8.
143. Wozniak, D.J., et al., *Alginate is not a significant component of the extracellular polysaccharide matrix of PA14 and PAO1 Pseudomonas aeruginosa biofilms.* Proc Natl Acad Sci U S A, 2003. **100**(13): p. 7907-12.
144. Diggle, S.P., et al., *The galactophilic lectin, LecA, contributes to biofilm development in Pseudomonas aeruginosa.* Environ Microbiol, 2006. **8**(6): p. 1095-104.
145. Tielker, D., et al., *Pseudomonas aeruginosa lectin LecB is located in the outer membrane and is involved in biofilm formation.* Microbiology, 2005. **151**(Pt 5): p. 1313-23.
146. Whitchurch, C.B., et al., *Extracellular DNA required for bacterial biofilm formation.* Science, 2002. **295**(5559): p. 1487.
147. Vilain, S., et al., *DNA as an adhesin: Bacillus cereus requires extracellular DNA to form biofilms.* Appl Environ Microbiol, 2009. **75**(9): p. 2861-8.
148. Suzuki, H., et al., *Characterization of extracellular DNA production and flocculation of the marine photosynthetic bacterium Rhodovulum sulfidophilum.* Appl Microbiol Biotechnol, 2009. **84**(2): p. 349-56.
149. Genevaux, P., et al., *Identification of Tn10 insertions in the rfaG, rfaP, and galU genes involved in lipopolysaccharide core biosynthesis that affect Escherichia coli adhesion.* Arch Microbiol, 1999. **172**(1): p. 1-8.
150. Danhorn, T. and C. Fuqua, *Biofilm formation by plant-associated bacteria.* Annu Rev Microbiol, 2007. **61**: p. 401-22.
151. Steenhoudt, O. and J. Vanderleyden, *Azospirillum, a free-living nitrogen-fixing bacterium closely associated with grasses: genetic, biochemical and ecological aspects.* FEMS Microbiol Rev, 2000. **24**(4): p. 487-506.
152. Somers, E., J. Vanderleyden, and M. Srinivasan, *Rhizosphere bacterial signalling: A love parade beneath our feet.* Critical Reviews in Microbiology, 2004. **30**(4): p. 205-240.
153. Okon, Y. and Y. Kapulnik, *Development and Function of Azospirillum-Inoculated Roots.* Plant and Soil, 1986. **90**(1-3): p. 3-16.
154. Perrig, D., et al., *Plant-growth-promoting compounds produced by two agronomically important strains of Azospirillum brasilense, and implications for inoculant formulation.* Appl Microbiol Biotechnol, 2007. **75**(5): p. 1143-50.
155. Hartmann, A., and Simmer, W. , *Physiology of Azospirillum*, in *Azospirillum/plant associations*, Y. Okon, Editor. 1994, CRC Press, Inc: Boca Raton.
156. Tien, T.M., M.H. Gaskins, and D.H. Hubbell, *Plant Growth Substances Produced by Azospirillum brasilense and Their Effect on the Growth of Pearl Millet (Pennisetum americanum L.).* Appl Environ Microbiol, 1979. **37**(5): p. 1016-1024.
157. Bottini, R., et al., *Identification of Gibberellin-A1, Gibberellin-A3 and Iso-A3 in Cultures of Azospirillum-Lipoferum.* Plant Physiology, 1989. **90**(1): p. 45-47.
158. Marchal, K. and J. Vanderleyden, *The "oxygen paradox" of dinitrogen-fixing bacteria.* Biology and Fertility of Soils, 2000. **30**(5-6): p. 363-373.
159. Sadasivan, L. and C.A. Neyra, *Flocculation in Azospirillum brasilense and Azospirillum lipoferum: exopolysaccharides and cyst formation.* J Bacteriol, 1985. **163**(2): p. 716-23.

160. Burdman, S., et al., *Aggregation in Azospirillum brasilense: effects of chemical and physical factors and involvement of extracellular components.* Microbiology, 1998. **144 (7)**: p. 1989-99.
161. Burdman, S., Y. Okon, and E. Jurkevitch, *Surface characteristics of Azospirillum brasilense in relation to cell aggregation and attachment to plant roots.* Critical Reviews in Microbiology, 2000. **26**(2): p. 91-110.
162. Sadasivan, L. and C.A. Neyra, *Flocculation in Azospirillum-Brasilense and Azospirillum-Lipoferum - Exopolysaccharides and Cyst Formation.* Journal of Bacteriology, 1985. **163**(2): p. 716-723.
163. Shapiro, J.A., *Thinking about bacterial populations as multicellular organisms.* Annu Rev Microbiol, 1998. **52**: p. 81-104.
164. Bahat-Samet, E., S. Castro-Sowinski, and Y. Okon, *Arabinose content of extracellular polysaccharide plays a role in cell aggregation of Azospirillum brasilense.* FEMS Microbiol Lett, 2004. **237**(2): p. 195-203.
165. Bashan, Y., H. Levanony, and E. Klein, *Evidence for a Weak Active External Adsorption of Azospirillum-Brasilense Cd to Wheat Roots.* Journal of General Microbiology, 1986. **132**: p. 3069-3073.
166. Bashan, Y., et al., *Evidence That Fibrillar Anchoring Is Essential for Azospirillum-Brasilense Cd Attachment to Sand.* Plant and Soil, 1991. **132**(1): p. 73-83.
167. Skvortsov, I.M. and V.V. Ignatov, *Extracellular polysaccharides and polysaccharide-containing biopolymers from Azospirillum species: properties and the possible role in interaction with plant roots.* FEMS Microbiol Lett, 1998. **165**(2): p. 223-9.
168. Katupitiya, S., et al., *A Mutant of Azospirillum-Brasilense Sp7 Impaired in Flocculation with a Modified Colonization Pattern and Superior Nitrogen-Fixation in Association with Wheat.* Applied and Environmental Microbiology, 1995. **61**(5): p. 1987-1995.
169. Umali-Garcia, M., et al., *Association of Azospirillum with Grass Roots.* Applied and Environmental Microbiology, 1980. **39**(1): p. 219-226.
170. Mora, P., et al., *Azospirillum brasilense Sp7 produces an outer-membrane lectin that specifically binds to surface-exposed extracellular polysaccharide produced by the bacterium.* Archives of Microbiology, 2008. **189**(5): p. 519-524.
171. Knoll M, R.E., *Das Elektronenmikroskop.* Zeitschrift fu¨r Physik, 1932. **78**: p. 318–339.
172. Porter, K.R., A. Claude, and E.F. Fullam, *A Study of Tissue Culture Cells by Electron Microscopy : Methods and Preliminary Observations.* J Exp Med, 1945. **81**(3): p. 233-46.
173. Parot, P., et al., *Past, present and future of atomic force microscopy in life sciences and medicine.* J Mol Recognit, 2007. **20**(6): p. 418-31.
174. Dufrene, Y.F., *Using nanotechniques to explore microbial surfaces.* Nat Rev Microbiol, 2004. **2**(6): p. 451-60.
175. Alonso, J.L. and W.H. Goldmann, *Feeling the forces: atomic force microscopy in cell biology.* Life Sci, 2003. **72**(23): p. 2553-60.
176. Jonas, K., et al., *Roles of curli, cellulose and BapA in Salmonella biofilm morphology studied by atomic force microscopy.* BMC Microbiol, 2007. **7**: p. 70.
177. Ding, Z., et al., *A novel cytology-based, two-hybrid screen for bacteria applied to protein-protein interaction studies of a type IV secretion system.* J Bacteriol, 2002. **184**(20): p. 5572-82.

178. Edwards, D.H., H.B. Thomaides, and J. Errington, *Promiscuous targeting of Bacillus subtilis cell division protein DivIVA to division sites in Escherichia coli and fission yeast.* Embo J, 2000. **19**(11): p. 2719-27.
179. Venkataraman, S., et al., *Automated analysis of fluorescence microscopy images to identify protein-protein interactions.* International Journal of Biomedical Imaging, 2006. **2006**(Article ID 69851): p. 10 pages.
180. Hartley, J.L., G.F. Temple, and M.A. Brasch, *DNA cloning using in vitro site-specific recombination.* Genome Res, 2000. **10**(11): p. 1788-95.
181. Conti, E. and J. Kuriyan, *Crystallographic analysis of the specific yet versatile recognition of distinct nuclear localization signals by karyopherin alpha.* Structure, 2000. **8**(3): p. 329-38.
182. Lange, A., et al., *Classical nuclear localization signals: definition, function, and interaction with importin alpha.* J Biol Chem, 2007. **282**(8): p. 5101-5.
183. Sambrook, J., E.R. Fritsch, and T. Maniatis, *Molecular cloning laboratory manual*. Vol. 2nd. 1989, Cold Spring Harbor, NY: Cold Spring Harbor Laboratory.
184. Heim, R., A.B. Cubitt, and R.Y. Tsien, *Improved green fluorescence.* Nature, 1995. **373**(6516): p. 663-4.
185. Wach, A., *PCR-synthesis of marker cassettes with long flanking homology regions for gene disruptions in S. cerevisiae.* Yeast, 1996. **12**(3): p. 259-65.
186. Conti, E., et al., *Crystallographic analysis of the recognition of a nuclear localization signal by the nuclear import factor karyopherin alpha.* Cell, 1998. **94**(2): p. 193-204.
187. Guzman, L.M., et al., *Tight regulation, modulation, and high-level expression by vectors containing the arabinose PBAD promoter.* J Bacteriol, 1995. **177**(14): p. 4121-30.
188. Chang, A.C. and S.N. Cohen, *Construction and characterization of amplifiable multicopy DNA cloning vehicles derived from the P15A cryptic miniplasmid.* J Bacteriol, 1978. **134**(3): p. 1141-56.
189. Larimer, F.W., et al., *Complete genome sequence of the metabolically versatile photosynthetic bacterium Rhodopseudomonas palustris.* Nat Biotechnol, 2004. **22**(1): p. 55-61.
190. Oda, Y., et al., *Functional genomic analysis of three nitrogenase isozymes in the photosynthetic bacterium Rhodopseudomonas palustris.* J Bacteriol, 2005. **187**(22): p. 7784-94.
191. Boel, G., et al., *Transcription regulators potentially controlled by HPr kinase/phosphorylase in Gram-negative bacteria.* J Mol Microbiol Biotechnol, 2003. **5**(4): p. 206-15.
192. Maurer, T., et al., *High-resolution structure of the histidine-containing phosphocarrier protein (HPr) from Staphylococcus aureus and characterization of its interaction with the bifunctional HPr kinase/phosphorylase.* J Bacteriol, 2004. **186**(17): p. 5906-18.
193. Omoya, K., et al., *Systematic optimization of active protein expression using GFP as a folding reporter.* Protein Expr Purif, 2004. **36**(2): p. 327-32.
194. Yang, M., Z. Wu, and S. Fields, *Protein-peptide interactions analyzed with the yeast two-hybrid system.* Nucleic Acids Res, 1995. **23**(7): p. 1152-6.
195. Keefe, A.D., et al., *One-step purification of recombinant proteins using a nanomolar-affinity streptavidin-binding peptide, the SBP-Tag.* Protein Expr Purif, 2001. **23**(3): p. 440-6.

196. Sundararaj, S., et al., *The CyberCell Database (CCDB): a comprehensive, self-updating, relational database to coordinate and facilitate in silico modeling of Escherichia coli.* Nucleic Acids Res, 2004. **32**(Database issue): p. D293-5.
197. Hazelbauer, G.L., J.J. Falke, and J.S. Parkinson, *Bacterial chemoreceptors: high-performance signaling in networked arrays.* Trends Biochem Sci, 2008. **33**(1): p. 9-19.
198. Parkinson, J.S., P. Ames, and C.A. Studdert, *Collaborative signaling by bacterial chemoreceptors.* Curr Opin Microbiol, 2005. **8**(2): p. 116-21.
199. Sourjik, V., *Receptor clustering and signal processing in E. coli chemotaxis.* Trends Microbiol, 2004. **12**(12): p. 569-76.
200. Wadhams, G.H. and J.P. Armitage, *Making sense of it all: bacterial chemotaxis.* Nat Rev Mol Cell Biol, 2004. **5**(12): p. 1024-37.
201. Hickman, J.W., D.F. Tifrea, and C.S. Harwood, *A chemosensory system that regulates biofilm formation through modulation of cyclic diguanylate levels.* Proc Natl Acad Sci U S A, 2005. **102**(40): p. 14422-7.
202. Black WP, Y.Z., *Myxoccus xanthus Chemotaxis Homologs DifD and DifG Negatively Regulate Fibril Polysaccharide Production.* J Bacteriol, 2003. **186**(4): p. 1001-1008.
203. Caiazza, N.C., et al., *Inverse regulation of biofilm formation and swarming motility by Pseudomonas aeruginosa PA14.* Journal of Bacteriology, 2007. **189**(9): p. 3603-3612.
204. Yang, Z.M. and Z. Li, *Demonstration of interactions among Myxococcus xanthus Dif chemotaxis-like proteins by the yeast two-hybrid system.* Archives of Microbiology, 2005. **183**(4): p. 243-252.
205. Bible, A.N., et al., *Function of a chemotaxis-like signal transduction pathway in modulating motility, cell clumping, and cell length in the alphaproteobacterium Azospirillum brasilense.* J Bacteriol, 2008. **190**(19): p. 6365-75.
206. Dufrene, Y.F., *Recent progress in the application of atomic force microscopy imaging and force spectroscopy to microbiology.* Curr Opin Microbiol, 2003. **6**(3): p. 317-23.
207. Dufrene, Y.F., *Atomic force microscopy, a powerful tool in microbiology.* J Bacteriol, 2002. **184**(19): p. 5205-13.
208. Stephens, B.B., S.N. Loar, and G. Alexandre, *Role of CheB and CheR in the complex chemotactic and aerotactic pathway of Azospirillum brasilense.* J Bacteriol, 2006. **188**(13): p. 4759-68.
209. Hauwaerts, D., et al., *A major chemotaxis gene cluster in Azospirillum brasilense and relationships between chemotaxis operons in alpha-proteobacteria.* FEMS Microbiol Lett, 2002. **208**(1): p. 61-7.
210. Madi, L. and Y. Henis, *Aggregation in Azospirillum-Brasilense Cd - Conditions and Factors Involved in Cell-to-Cell Adhesion.* Plant and Soil, 1989. **115**(1): p. 89-98.
211. Doktycz, M.J., et al., *AFM imaging of bacteria in liquid media immobilized on gelatin coated mica surfaces.* Ultramicroscopy, 2003. **97**(1-4): p. 209-16.
212. Burdman, S., et al., *Involvement of outer-membrane proteins in the aggregation of Azospirillum brasilense.* Microbiology, 1999. **145 (Pt 5)**: p. 1145-52.
213. Burdman, S., et al., *Extracellular polysaccharide composition of Azospirillum brasilense and its relation with cell aggregation.* FEMS Microbiol Lett, 2000. **189**(2): p. 259-64.
214. De Hoff, P.L., L.M. Brill, and A.M. Hirsch, *Plant lectins: the ties that bind in root symbiosis and plant defense.* Molecular Genetics and Genomics, 2009. **282**(1): p. 1-15.

215. Delgallo, M., M. Negi, and C.A. Neyra, *Calcofluor-Binding and Lectin-Binding Exocellular Polysaccharides Ofazospirillum-Brasilense and Azospirillum-Lipoferum.* Journal of Bacteriology, 1989. **171**(6): p. 3504-3510.
216. Karpati, E., et al., *Interaction of Azospirillum lipoferum with wheat germ agglutinin stimulates nitrogen fixation.* Journal of Bacteriology, 1999. **181**(13): p. 3949-3955.
217. Mulyukin, A.L., et al., *Diverse morphological types of dormant cells and conditions for their formation in Azospirillum brasilense.* Microbiology, 2009. **78**(1): p. 33-41.
218. Pereg-Gerk, L., et al., *A transcriptional regulator of the LuxR-UhpA family, FlcA, controls flocculation and wheat root surface colonization by Azospirillum brasilense Sp7.* Molecular Plant-Microbe Interactions, 1998. **11**(3): p. 177-187.
219. Pereg Gerk, L., K. Gilchrist, and I.R. Kennedy, *Mutants with enhanced nitrogenase activity in hydroponic Azospirillum brasilense-wheat associations.* Appl Environ Microbiol, 2000. **66**(5): p. 2175-84.
220. Stahlberg, H., et al., *Oligomeric structure of the Bacillus subtilis cell division protein DivIVA determined by transmission electron microscopy.* Mol Microbiol, 2004. **52**(5): p. 1281-90.
221. Ramamurthi, K.S. and R. Losick, *Negative membrane curvature as a cue for subcellular localization of a bacterial protein.* Proc Natl Acad Sci U S A, 2009. **106**(32): p. 13541-5.

VITA

Amanda Nicole Billings Edwards was born Athens, Tennessee in 1982. From an early age, her parents encouraged creativity and curiosity in the natural world. She attended public schools where both of her parents were teachers. She graduated from McMinn County High School in 2000. That fall she began her undergraduate education at Cleveland State Community College and then transferred to the small Liberal Arts school, Tennessee Wesleyan College, to complete her degree in Biology in 2004. It was at TWC that she started to develop a greater appreciation for molecular and microbiology research. Following graduation, she worked for a brief period of time at Schering-Plough Pharmaceuticals, until she accepted an internship position at Oak Ridge National Laboratory. It was during this time that she applied to graduate school. In February of 2005, she was accepted in the Genome Science and Technology program at the University of Tennessee-Knoxville. She completed her PhD degree in the Spring of 2011.